UNIVERSITÀ DEGLI STUDI DI PADOVA
Dipartimento di Ingegneria Elettrica

Scuola di Dottorato di Ricerca in Ingegneria Industriale
Indirizzo di Ingegneria Elettrotecnica

Ciclo XX

Aspects of Electromagnetic Modelling for Multiple-Input-Multiple-Output Control of MHD Modes in RFX-mod

Direttore della Scuola: Prof. Paolo F. Bariani
Supervisore: Prof. Francesco Gnesotto

Dottorando: Ing. Anton Soppelsa

31 Gennaio 2008

To my Mother,
tireless worker able to teach
the meaning of honesty and humility

Sommario

L'attivita di ricerca oggetto della presente discussione, è stata condotta nell'ambito della Scuola di Dottorato in Ingegneria Industriale, indirizzo Ingegneria Elettrica dell'Università degli Studi di Padova. Oggetto primario dello studio, svoltosi nel settore della modellistica dei sistemi elettromagnetici, è l'analisi del sistema di controllo attivo per la stabilizzazione dei modi MHD del plasma nell'esperimento RFX-mod. Tre i risultati principali dell'attività di ricerca: il primo è l'inquadramento dello specifico problema di controllo nell'ambito della teoria unificata dei segnali, aspetto significativo al fine di fornire un solido impianto teorico dal quale procedere per sviluppare nuovi modelli e tecniche di controllo; il secondo è la realizzazione di un modello matematico dell'impianto basato interamente su misure sperimentali che permette l'analisi della struttura del sistema, la simulazione del suo comportamento dinamico e lo sviluppo di schemi di controllo innovativi; il terzo infine è l'effettiva realizzazione di un nuovo algoritmo di controllo basato sul modello ricavato.

Il sistema preso in considerazione nel presente studio è composto da 192 unità, ognuna delle quali comprende una bobina attiva, il suo alimentatore, tre sensori di campo radiale, rispettivamente toroidale e poloidale. Le bobine attive ed i sensori di campo radiale sono disposti ordinatamente in modo da ricoprire due superfici toroidali e sono organizzati in 48 array poloidali di 4 elementi ciascuno. Tra le bobine attive e i sensori di campo magnetico sono presenti strutture metalliche di diverso spessore che sono sede di fenomeni dissipativi dovuti alle correnti indotte dal sistema di controllo attivo e dal plasma stesso.

Durante la prima fase della ricerca si sono effettuate campagne sperimentali per misurare il mutuo effetto delle correnti nelle bobine attive e l'effetto sul flusso magnetico misurato dai sensori radiali. I dati provenienti dalle campagne hanno permesso di risalire alla forma matematica della matrice delle mutue induttanze delle bobine attive e di quella delle mutue induttanze tra bobine attive e sensori radiali. A causa della presenza delle strutture passive le matrici non sono costanti, ma variano al variare della frequenza. Per questo motivo le campagne sperimentali sono state condotte studiando il comportamento

degli accoppiamenti in esame a diverse frequenze. Un modello del sistema di controllo dei modi MHD del plasma è stato costruito sulla base di queste due matrici di trasferimento ed è stato completato con l'aggiunta del modello degli alimentatori delle bobine attive. Ciò è stato completato con la scrittura di opportune procedure Matlab® che hanno permesso di automatizzare il processo di calcolo a partire dall'acquisizione dei dati sperimentali e da alcune ipotesi riguardanti il numero di accoppiamenti significativi.

Successivamente il modello è stato sottoposto ad un'intesa attività di validazione, comprendente verifiche del funzionamento in catena aperta, sia a tensione impressa sia a corrente impressa, ed in catena chiusa. Si è constatato che il modello riproduce con un'accuratezza del 5% i segnali sperimentali, che è sufficientement fedele da riprodurre correttamente l'intervallo di stabilità del sistema retroazionato e può quindi venire usato con successo come strumento d'indagine di fenomeni marginalmente stabili.

L'analisi del modello ha evidenziato due importanti fenomeni. In primo luogo l'accoppiamento tra bobine attive e sensori radiali non è così localizzato come postulato a priori e ciò ha comportato il calcolo di un maggior numero di accoppiamenti. In secondo luogo l'uniformità degli accoppiamenti risulta inferiore alle aspettative, evidenziando che la presenza di disuniformità importanti delle strutture passive costituisce un limite alle massime prestazioni dinamiche del sistema nella configurazione attuale.

Nell'arco dell'ultimo anno di ricerca è stato realizzato un nuovo algoritmo di controllo basato sulla decomposizione a valori singolari del modello ricavato negli anni precedenti. Risultati di simulazioni confermano che questo algoritmo di controllo è in grado di compensare le principali disomogeneità delle strutture passive almeno fino a una frequenza limite, oltre la quale la potenza erogata dagli alimentatori non è più sufficiente a contrastare gli effetti delle correnti indotte.

Parte dell'attività di ricerca è stata svolta nell'ambito di una collaborazione tra il Consorzio RFX ed il laboratorio JET di Culham (UK) riguardante il potenziamento dell'amplificatore per il controllo dell'instabilità verticale di plasma. In tale ambito la presente attività di ricerca hacontribuito alla realizzazione della parte software del sistema di controllo del nuovo amplificatore risonante.

Summary

The research activity object of the present dissertation has been carried out at the Industrial Engeneering Doctoral School (Course of Electric Engeneering) of the University of Padova. The study concerned the electromagnetic systems modelling with regard on active control system analysis for the stabilization of plasma MHD modes in the RFX-mod experiment. Three are the main results of the research activity. The first one is the inclusion of the specific problem in the frame of the Unified Signal Theory, important in order to build a solid theoretical background from which starting developing new control models and techniques. The second one is the production of a mathematical model of the plant based exclusively on experimental measures. This allow the system's structure analysis, the simulation of its dynamic behaviour and the development of innovative control schemes. The third one is the actual production of a new algorithm based on the developed model.

The system cosidered in the present study is made up by 192 units, each one including an active coil, its power amplifier, three field sensors (respectively radial, toroidal and poloidal). The active coils and the radial sensors are laid down in a regular manner and in this way they cover exactly the toroidal surfaces they intersects. Both of them form a grid made of 48 poloidal arrays, each one consisting of 4 elements. Metallic structures of different thickness are present in between the active coils and the magnetic field sensors, which are interested by dissipative effects due to the induced currents by the active control system and by the plasma.

During a first phase of the research, experimental campaigns have been made in order to measure quantitatively the mutual couplings between saddle coils and the effect of their currents on the magnetic field measured by the radial sensors. Data collected during these campaigns allowed for the mathematical form of the active coils inductance matrix and the mutual inductance between active coils and sensors to be discovered. Due to the presence of the passive structures these matrices are not constant, but variable in the frequency domain. For this reason the campaigns have been carried out studying the behaviour of the couplings at different frequencies. A model of the cou-

plings has then been derived and used in the construction of a bigger model comprehensive of the active coils and power amplifier dynamics. The task has been completed by writing convenient procedures in the Matlab® language, which allowed for an automated processing of the experimental data under some simplifying hypothesis about the number of significative couplings.

Later the model has been intensively validated. Tests have been carried out both in open loop and closed loop. The open loop tests have been made by comparing the real and simulated outputs corresponding to the applied voltages and currents. The model was able to reproduce the output quantities with a 5% accuracy, to mimic the real closed loop stability range and has been used with success as a tool to gain insight into marginally stable phenomena.

The model analysis evidenced a couple of important facts. The first is that the coupling between active coil and sensor is not so local as expected; this required a great number of couplings to be considered. The second is that the uniformity of the couplings is less than expected. The presence of features, like the inner equatorial gap, ruining the uniformity of the passive structures acts as a limit of the obtainable performance in the present configuration.

On the basis of the model a new control algorithm has been designed using the singular value decomposition. Simulation results confirm that this control algorithm is able to compensate the effects of the local features of the passive structures till a limit frequency. Above that frequency the power required for the compensation would exceed the capacity of the amplifiers.

Part of the research activity has been carried out in the frame of a collaboration between the Consorzio RFX and the EFDA-JET laboratory of Culham (UK) about the upgrade of the power amplifier of the plasma vertical instability. Here the research has focused on the realisation of part of the software control system of the new resonant amplifier.

Contents

Acknowledgments

This Doctoral dissertation could not have been written without the aid of many colleagues and friends who constantly helped me in the research activity. I sincerely would like to thank them all and I regret not being able to mention everyone with the due precision. I am particularly grateful to Giuseppe Marchiori, with whom I share the authorship of many of the presented results, to Mario Cavinato, Gabriele Manduchi, Cesare Taliercio, Lionello Marrelli, Paolo Zanca for their precious suggestions, to my Advisor Prof. Francesco Gnesotto and my Tutor Adriano Luchetta for their useful guide, to Prof. James R. Drake of the Royal Institute of Technology and to Prof. Bernardo Brotas de Carvalho of the Instituto Superior Técnico for their willingness to comment this dissertation, to Filippo Sartori, Fabio Piccolo, Luca Zabeo for their support while I was at the JET Laboratory, to the other PhD students Cristiano Taccon, Fulvio Auriemma, Matteo Agostini, Federica Bonobo, Marco Gobbin for their help in printing the dissertation copies and in submitting it to the University office. Thanks to Prof. Giuseppe Chitarin for having provided the values of the mutual couplings between active coils and sensors at frequency zero and to Ing. Antonio Masiello for having provided the analogous values for the active coils couplings.

Most of all, I would like to thank my precious Marcella "Alpine Awareness" Morandini, her parents and all my Family, for the constant support they have provided and the patience they have showed, especially in the final steps of the writing.

Chapter 1

Introduction

1.1 Structure of the Document

The present document is the summary of the research carried out from January 2005 to December 2007 at the Padova University Electrical Engineering Doctorate School. The first chapter presents background material. After a short introduction to the research in the field of nuclear fusion, the description of the toroidal coordinate system provides the pretext to introduce the terminology used in the following sections. The Doctoral activity and the place where it has been carried out are then presented. In the following chapters 2, 3, 4 results of the research are shown and discussed. These chapters cover different aspects of the research. In chapter 2 theoretical backgrounds are given. In chapter 3 the core result of the research is described. Chapter 4 deals with the implementation of a software device that theoretically allows for an improvement of performance. Finally, chapter 5 is reserved for concluding remarks.

1.2 Background

The following subsection aims at providing some background information about the nuclear fusion and the research in this field without any claim of completeness. The intention is to give the minimum information required for a better understanding of the rest of the document. Publications covering the topics of this chapter at an introductory level are: [1] for a good review of the modern physics of the magnetically confined plasmas, [2] for a description of the RFX machine structure, [3] for a description of the RFX-mod peculiarities, [4] for a paper on the aspects of the RFX-mod MHD control system design, and [5] for a book covering the history of the magnetically confined fusion research.

1.2.1 Nuclear fusion

Nuclear fusion is the process by which a couple of atomic nuclei join together to form a heavier one. When nuclei of light elements undergo a fusion reaction, some mass is lost in the process and energy is liberated according to the Einstein's equation $E = mc^2$.

Such nuclear reactions happen naturally in the stars, where high temperature and pressure allow hydrogen nuclei to get close enough for the strong force to bind them together. In this case the gravitational force is responsible of creating the conditions in which the fusion can occur; so the fusion reactions happening in the stars are said to be *gravitationally* confined. The adjective *thermonuclear* specifies that the electrical repulsion of nuclei carrying charge of the same sign is won by means of their thermal energy. It is usually specified in contrast with the so called *cold* fusion, where the problem of winning the Coulomb Barrier is faced by means of other effects.

Among all the possible nuclear fusion reactions, the one that happens in the most favourable conditions is the fusion between deuterium ${}^{2}_{1}\mathrm{H}^{+}$ and tritium ${}^{3}_{1}\mathrm{H}^{+}$ nuclei. This because the cross section for the reaction tritium-deuterium is so that it can balance the radiative losses of a confined plasma with the given density at the lowest possible temperature.

Apart from the gravitational confinement, there are other two methods to achieve the conditions of temperature and pressure which allow for the thermonuclear fusion reactions to happen. One is based on the momentum conservation and it is called *inertial* confinement, the other is based on the Lorentz force and therefore it is called *magnetic* confinement.

The magnetically confined thermonuclear fusion relies on the fact that at the working conditions the reactants are fully ionised. That is the gas of the reacting species is made entirely of electrons and positive ions freely moving in the space. Charged particles interact with the magnetic field through the Lorentz's force and for this reason they can actually be confined by a properly shaped magnetic field. Macroscopically, a ionised gas at high temperature is a good conductor which can be interested by a flow of electric current. The interaction between this current and the surrounding magnetic field, giving rise to the confining force. A ionised gas macroscopically neutral is called *plasma*.

Research into the field of plasma physics began in the 1950s, with the purpose of developing a new commercially viable energy source and still continues to this day. Since its beginning, the research activity in the field of magnetically confined thermonuclear fusion has been carried out with the aid of electromechanical devices, able to confine plasma inside their vacuum chamber. The development of the plasma research in the field has been tightly linked with the development of the machines used for the experiments. In the

following years several machines, corresponding to several different magnetic configurations, have been realised. The most successful of them were based on a *toroidal* geometry. The size and complexity of such devices has grown gradually from the initial major radius of about half a meter to the several meters of the current biggest devices.

The toroidal magnetic configurations presently used in the fusion research are the *Tokamak*, the *Stellarator* and the *Reversed Field Pinch* (RFP). All of them share the toroidal concept for their construction but the magnetic configuration is rather different. In Tokamaks and Reversed Field Pinches a toroidal current is induced in the plasma with a central solenoid and a toroidal field is applied with convenient *toroidal field* coils. The shape of the magnetic field is controlled to a higher degree with additional *poloidal field* windings. However the two configurations differ because in Tokamas the toroidal component of the magnetic field is much stronger than the poloidal component, whereas in the Reversed Field Pinches they are of comparable size. Moreover the toroidal field change sign at a point between the plasma centre and the plasma edge. Stellarators are different because they do not require an induced toroidal current in order to confine the plasma. This naturally allows for operations in steady state, but this configuration requires the design and realisation of coils with complex, non-planar shapes.

Today the research in the field of magnetically confined thermonuclear fusion is carried out at Universities, Laboratories and Research Centres around the world. The operating machines where it is possible to perform experimental exploitation of magnetically confined plasmas are now a few tens and other machines are currently being build. The research reported in this document has been carried out in two of these laboratories, namely the Reversed-Field eXperiment (RFX), run by the Consorzio RFX in Padova, Italy and the Joint European Torus (JET), a project run in the framework of the European Fusion Development Agreement (EFDA) by the United Kingdom Atomic Energy Agency (UKAEA) at Culham, in the United Kingdom. Presently, RFX and JET are the world biggest operating Reversed Field Pinch and Tokamak respectively.

1.2.2 MHD theory and plasma instabilities

The most simple physical model of the plasma behaviour is described by the *magnetohydrodynamic* (MHD) theory. This academic discipline studies the behaviour of the electrically conducting fluids from a macroscopic point of view. The starting point of the theory is a set of equations comprehensive of the Navier-Stokes equations of fluid dynamics, the Maxwell's equations of electromagnetism and a plasma state equation involving the thermodynamical

quantities. Depending on the applications, this set of equations can be already too much to explain the fundamentals of the plasma dynamic in a magnetic field. In this case simplifying assumptions are made and special theories are derived. One of the most important simplifications is to consider the plasma resistivity equal to zero. In this case the plasma becomes a perfect conductor able to freeze the magnetic field lines in their original configuration. In this case the name of the theory becomes *ideal* MHD. Depending on the working hypothesis, other names are commonly in use. For example *resistive* MHD, where the plasma resistivity is considered, and *two-fluid* MHD, where the ions and electrons are treated as different fluids.

However, even the most general MHD theory has limits. To be applicable this model requires the distribution of the particles forming the fluid to be close to Maxwellian. Even if the rate of Coulombian collisions in the plasma multiplied by the time constant of the MHD phenomena is high, this hypothesis is not automatically verified. This happens because in fusion plasmas the mean free path of the particles can be as big as tens of thousands of times the size of the machine itself. This should shed some light about the fact that there do exist macroscopical phenomena which cannot be explained by a fluid theory and therefore that there is the need of developing a kinetic theory able to take into account, for example, the effects of a non Maxwellian distribution of the plasma particles. The ideal MHD is almost invariably the first model considered by experimental physicists and engineers because of its ideal simplicity, its ability of capturing many of the important properties of plasma dynamics and being often also qualitatively accurate.

Ideal MHD theory is particularly useful, because in many cases it can be applied to analyse the plasma behaviour in the neighbourhood of a given equilibrium state. The plasma is said to be in a *equilibrium state* if there are not net forces accelerating macroscopically any part of the plasma itself. If the equilibrium is stable a small perturbation in the plasma configuration will be damped out, if not it will grow, eventually causing the collapse of the magnetic configuration, the lost of the confinement and the premature end of the discharge. The understanding of the plasma instabilities is therefore of primary interests for the realisation of stable devices to be used in the magnetically confined fusion research. The plasma instabilities which can be predicted by and analysed with the help of the MHD theory are called *MHD instabilities*. Examples of these instabilities, are the *resistive wall mode* (RWM) instability and the *neoclassical tearing mode* instability. The former is the instability arising in presence of a wall with finite conductivity while the plasma would have been MHD stable in front of a perfectly conducting one, the latter is due to the non-zero resistivity of the plasma. Examples of more trivially ex-

plainable instabilities are the vertical instability that affects Tokamaks with elongated, non-circular plasma profiles, or the horizontal instability due to the inhomogeneity of the pressure at the surface.

1.2.3 Toroidal coordinate system

Toroidal surfaces are central to the theory of plasma confinement. Axial symmetry is a feature pursued by engineers in system design as it allows for simplified modelling, implementation, testing and commissioning. For these reasons, when possible, the structural components of the machines used in the field of the magnetically confined fusion are designed exploiting axial-symmetry. Cylindrical set of coordinates are therefore very common in the field of the magnetically confined fusion.

As the electrical machines used in this field of the plasma science are toroidal in nature, beside the cylindrical coordinates a *toroidal* frame of reference is also commonly used. In these coordinates a point

$$\boldsymbol{p} = x\hat{\boldsymbol{i}} + y\hat{\boldsymbol{j}} + z\hat{\boldsymbol{k}} \tag{1.1}$$

in the three-dimensional Cartesian space V is labelled by the triplet (r, ϑ, φ) using the change of variables $\boldsymbol{g} : \mathbb{R}^3 \to \mathbb{R}^3$ defined by the equations

$$\begin{aligned} x(r, \vartheta, \varphi) &= (R_0 + r\cos\vartheta)\cos\varphi \\ y(r, \vartheta, \varphi) &= (R_0 + r\cos\vartheta)\sin\varphi \\ z(r, \vartheta, \varphi) &= r\sin\vartheta. \end{aligned} \tag{1.2}$$

and considering the mapping $\boldsymbol{x} = \boldsymbol{p} \circ \boldsymbol{g}$ from $\mathbb{R}^3$ onto V.

The variables r, ϑ, φ are called *toroidal* coordinates[1], and ϑ and φ are respectively the *poloidal* and the *toroidal* angles, while r is the *radial* coordinate or *radius*. The positive number R_0 is one of the most fundamental machine parameters: the nominal *major radius*. The coordinate surfaces of this mapping are toroidal, conical and planar corresponding respectively to constant r, ϑ and φ. The planar coordinate surfaces are called *poloidal* planes. A visual description of a toroidal surface is reported in Figure 1.1. The black lines on the surface are the intersections between the toroidal surface and the other coordinate surfaces. The blue and red arrows show respectively the versus of

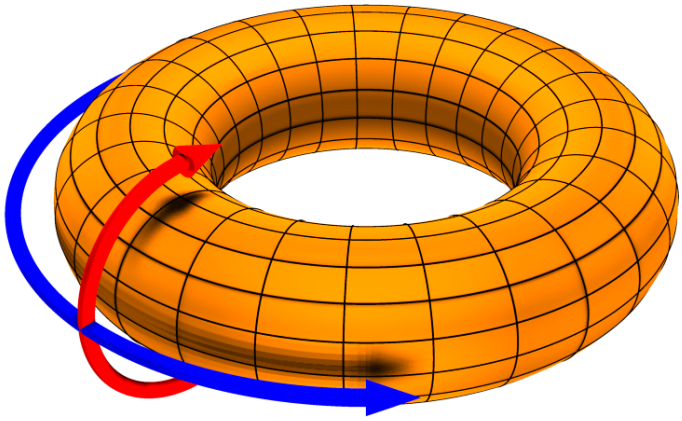

Figure 1.1: Toroidal (blue arrow) and poloidal (red arrow) coordinates on a toroidal surface. Picture licensed under Creative Commons Attribution 2.5 License, Made in POV-Ray by Dave Burke 2006

toroidal and poloidal coordinate.

The same terminology is used to refer to components of the machine which exhibit analogous structure. For example axialsymmetric coils are called also *toroidal* coils, the coils producing the toroidal magnetic field are called also *poloidal* coils, the vacuum vessel where the plasma is created is sometime also called toroidal chamber; moreover in case of probes placed on the vacuum vessel is handy labelling them with toroidal and poloidal indices. Additionally

[1]The toroidal coordinates so defined do not have the property of being separable. Separable toroidal coordinates for the Laplace equations do exist, for example

$$x(\tau,\sigma,\varphi) = a\ \frac{\sinh\tau}{\cosh\tau-\cos\sigma}\cos\varphi$$

$$y(\tau,\sigma,\varphi) = a\ \frac{\sinh\tau}{\cosh\tau-\cos\sigma}\sin\varphi$$

$$z(\tau,\sigma,\varphi) = a\ \frac{\sin\sigma}{\cosh\tau-\cos\sigma}$$

the z axis, the xy plane and the circle $r = 0$ to be called, respectively, *principal axis*, *equatorial plane* and *secondary axis*.

Some attention has to be made in the definition of the domain of the coordinates change in order to attain its bijectivity. As a matter of fact, the injectivity of such a mapping is guaranteed only if its domain is reduced to the region U of the points (r, ϑ, φ) satisfying

$$\begin{gathered} -\pi < \vartheta \leq \pi \\ -\pi < \varphi \leq \pi \\ r > 0 \\ -r\cos\vartheta < R_0 \end{gathered} \tag{1.3}$$

In this case, the function $\boldsymbol{g}$ is not surjective any more as the the principal and secondary axes are not reached by the constrained coordinates. On these regions, however, the Jacobian matrix of $\boldsymbol{g}$ would be singular and the corresponding mapping $\boldsymbol{x} : U \subset \mathbb{R}^3 \to V$ not regular. Instead, in the region of V obtained removing the principal and secondary axes, the above toroidal coordinates are orthogonal, defining an orthonormal basis as follows

$$\begin{aligned} \hat{\boldsymbol{u}}_r(r, \vartheta, \varphi) &= -\frac{d\boldsymbol{x}}{dr}(r, \vartheta, \varphi) \\ \hat{\boldsymbol{u}}_\vartheta(r, \vartheta, \varphi) &= \frac{1}{r}\frac{d\boldsymbol{x}}{d\vartheta}(r, \vartheta, \varphi) \\ \hat{\boldsymbol{u}}_\varphi(r, \vartheta, \varphi) &= \frac{1}{R_0 + r\cos\vartheta}\frac{d\boldsymbol{x}}{d\varphi}(r, \vartheta, \varphi) \end{aligned} \tag{1.4}$$

This basis is commonly used to represent vectorial quantities such as the total magnetic field produced by the set of active coils in the following form

$$\boldsymbol{b}(r, \vartheta, \varphi) = b_r(r, \vartheta, \varphi)\hat{\boldsymbol{u}}_r + b_\vartheta(r, \vartheta, \varphi)\hat{\boldsymbol{u}}_\vartheta + b_\varphi(r, \vartheta, \varphi)\hat{\boldsymbol{u}}_\varphi. \tag{1.5}$$

1.2.4 Devices for the magnetically confined fusion

The devices used today by experimentalists of the magnetically confined fusion science are large electrical machines, integrated with a number of auxiliary systems. In the context of the magnetically confined fusion research all the devices share a common conceptual design. The main components of these machines are: the vessel, the magnetic system, the heating and current drive systems, the diagnostics and the control system.

The vessel

The region where the plasma is created is bounded by a ring shaped structure which constitutes the *vacuum vessel*. The internal wall of the vessel is

protected, totally or partially, by a cover of tiles called *first wall*. It is generally constructed with elements or materials made up of atoms with a low atomic number that are able to resist to a high thermal load like, for example, graphite, carbon fibre composites (CFC), or beryllium. The vacuum vessel is so called because inside the plasma an ultra-high vacuum is obtained before starting the operations in order to reduce the impurity density.

The magnetic system

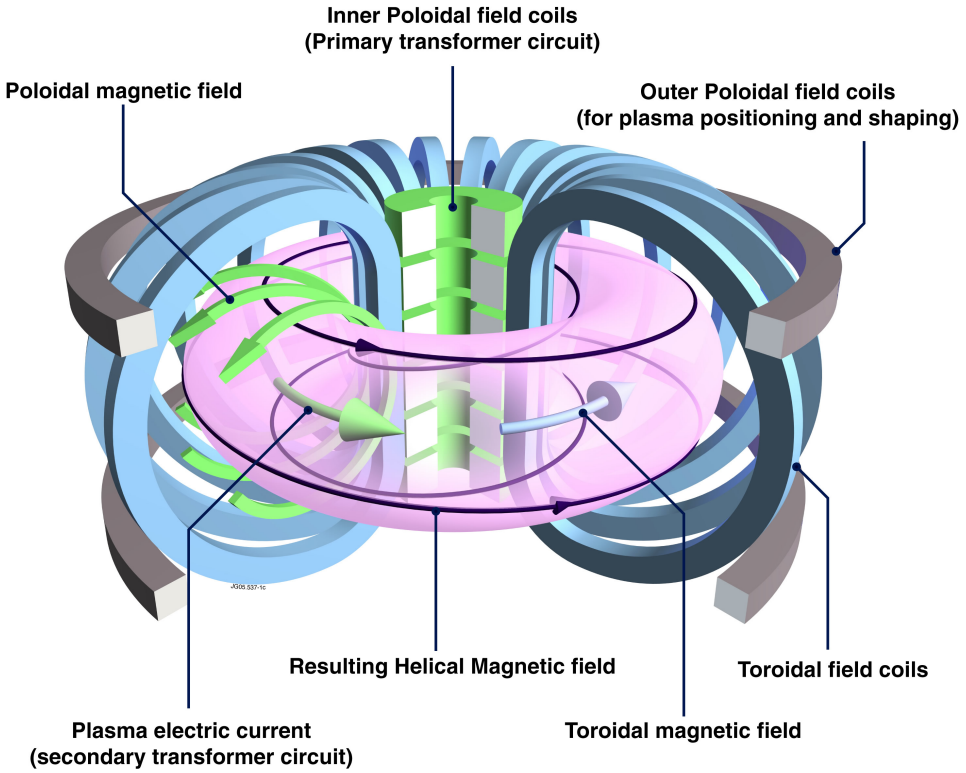

Figure 1.2: Conceptual structure of a Tokamak magnetic subsystem. Graphics: EFDA-JET

In the case of Tokamaks and Reversed Field Pinches, a number of *poloidal coils* are placed around the support structure eventually wrapping the vacuum vessel to create a toroidal magnetic field. These coils act as a sparse toroidal solenoid. In the centre of the torus, along its primary axis, a rectilinear solenoid is placed. This set of coils is usually referred to as *central solenoid*, however *inner poloidal field* coils and *magnetising circuit* are sometime used as synonyms. The main role of the central solenoid is to induce a toroidal

electrical field in the plasma. The consequent loop voltage drives a toroidal current in the plasma, which is called *plasma current* and which is another fundamental parameter of this kind of machines. The plasma current can be sustained as long as the magnetising circuit is able to vary monotonically its current. Toroidal coils are also placed conveniently outside the vacuum vessel, usually in the outer region. They are used for two tasks: to control the plasma position and to shape the plasma boundary. These toroidal coils are also called *field shaping* coils. A picture of the gross magnetic configuration in the case of a Tokamak machine is presented in Figure 1.2.

Things are slightly different for Stellarators. In this case the central solenoid is not strictly required and the two toroidal and poloidal sets of coils are merged in one single set of non planar coils. These kind of winding can be elicoidal-like or even more complex. Other coils, local in nature, are the *error field* coils used for the correction of the field errors in the neighbouring of non-axialsymmetric features of the machine or for a finer control of the plasma boundary.

The main material used in the construction of the machines magnetic system was, in the past, copper. Nowadays, in order to be able to control the plasma for a longer time, the coils of the magnetic system are usually made of superconducting materials. This choice is essentially imposed by the fact that it is extremely difficult to design copper coils able to sustain the ohmic thermal load of the nominal current densities for the requested period of time.

Each one of these coils system is usually fed by a corresponding independent power supply group. The characteristic of the power supplies vary depending on the size of the machine and the length of the plasma discharge. Usually, in small and medium sized machines, the energy required for the operations is stored in mechanical, magnetic and electric accumulators which take it from the national power grid. The nominal power of the converters used to perform this task can be a fraction of the actual maximum power required by the machine operations. This approach needs a careful design of the energy storage systems and of the converters. However, the most challenging power supplies are those of big seized machines which operate with long discharge or in steady state. These kind of power supplies require a careful engineering activity and non-standard designs, as the mean power requested by these machines can be of the order of 500 MegaWatt.

Auxiliary heating and current drive systems

The most simple mechanism rising the plasma temperature is given by the Ohm's effect. The current induced in the plasma by the central solenoid flux swing is also responsible for its temperature rise. However, as the plasma resistance decrease with the plasma temperature, this mechanism is not sufficient

to reach the target temperature. For this reason other heating mechanism are required. These plasma auxiliary heating systems are based on the coupling of electromagnetic waves with the plasma at the ion, electron or hybrid cyclotron frequency and on the injection into the plasma of a "current" of neutral particles, usually hydrogen or deuterium atoms. The injection of neutral particles requires a device called *neutral beam injector* which is itself a system of the same order of complexity than the machine. In machines like Tokamaks and RFP, which usually operates in a pulsed regimes, this system can also be used as non inductive *current drive* system. By using these devices it is possible to increase the length of the pulse beyond the limits imposed by the maximum amount of magnetic energy that can be stored in the central solenoid, possibly reaching the steady state operational regime. Such heating system becomes the primary heating facilities in machines without a central solenoid, as could be in Stellarators.

Diagnostics

Being experimental machines these kind of devices are usually filled up with diagnostic equipment of several kind. The most commonly used are: magnetic probes (such as field probes and Rogowsky coils), temperature and pressure sensors, optic sensors, like infra red cameras, Thompson scattering, interferometers and neutrons detectors.

The control system

All the machine subsystem can also be seen as information users. Many of them, like the diagnostic systems, are data producers, others, such as the power amplifiers controlling the current in the coils, are data consumer and several are both of them at the same time, for example all the controllers which process input data producing output data. In this vision the devices of the subsystems of the machine are components of a network where information flows from one node to another. This flow needs to be controlled carefully. Data processing quality, that is the reliability and capability of the information processing, is of critical importance for the machine operations. Some of them are indeed subject to strict, real-time, timing requirements.

Other systems

Apart from the subsystems described above there is a great number of other components, sometimes called auxiliary system, which are essential for the machine operations. For example: the coils cooling system, the cryogenic

system, the gas pumping and the vacuum system, eventually the cooling system for the conversion of the nuclear reactions energy.

In the past the coil cooling system has been implemented with standard technology, but the use of superconducting coils requires the set up of a cryogenic system working at a temperature of about 4 Kelvin. The cryogenic system can also be used to implement the last component in the vacuum pumping chain. Indeed this system can be implemented with lines made of a cryopump, a turbomolecular and a rotative pump connected in series. If the number of fusion reactions become significant (as it should be in the case of the next generation machines) the implementation of a system which takes care of the the heat generated by the neutrons produced by the fusion reactions is also required.

Despite its length, this list of subsystems is not exhaustive of all the components important for the realisation of a device for the study of the magnetically confined nuclear fusion. The present section aims at giving the idea of the complexity of such devices.

1.2.5 RFX-mod

Most of the doctoral research activity has been carried out at the RFX-mod site, in Padova, Italy. RFX-mod is currently the biggest RFP in the world and it is run by the "Consorzio RFX", an EURATOM-ENEA association. The machine, known in the past with the name "Reversed Field eXperiment" (RFX), started the operations in the 2004 after an upgrade triggered by a fire that in the 1999 destroyed part of its power supplies. Modifications applied to the machine components have been thought to be important enough to be mentioned in its name, so it has been changed to *RFX-mod*.

The structure of RFX-mod is essentially the one described in the previous subsection. A slightly more descriptive illustration of the components of interest for the doctoral dissertation is given in the following one. The details of the major modifications of RFX-mod have been reported in the papers [3].

The main parameters of the RFX machine are listed in Table 1.1. The vacuum vessel is a toroidal rigid structure made of INCONEL 625, composed of 72 elements welded together. Its inner surface is fully covered by graphite tiles, and be baked at temperatures between 350-400 °C. The vessel major radius is 2 m while its minor radius is 0.5 m. The vacuum vessel is also an interface between the plasma and the outside. It is therefore equipped with 96 ports for gas immission, vacuum pumping and diagnostic systems.

In RFX-mod the vacuum vessel is surrounded by a 3 mm thick copper shell. The purpose of this structure is to provide a *passive stabilisation* of the fast magnetohydrodynamical instabilities. This component, common in RFP

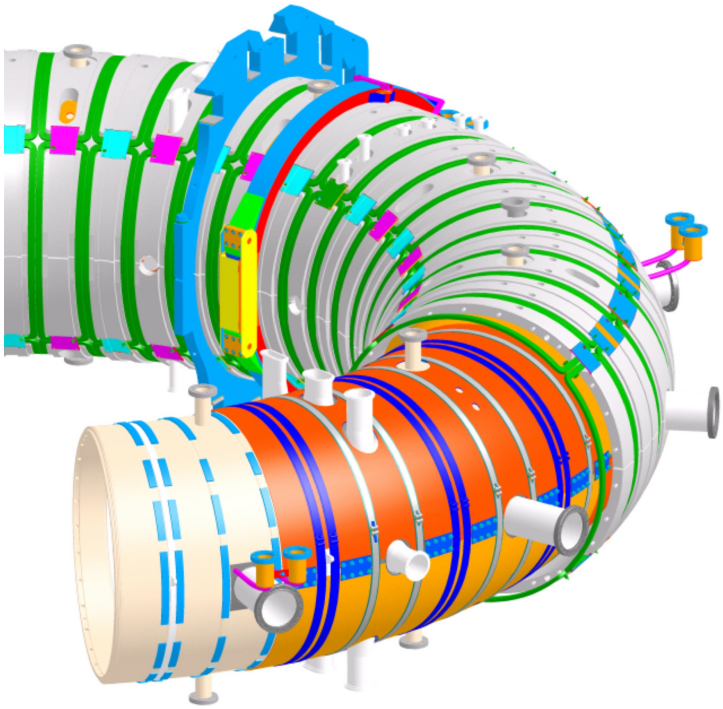

Figure 1.3: RFX-mod assembly.

machines, was not described in the general section, but, together with the *active control* system of the MHD instabilities, it is one of the fundamental components for the present document. The shell is not uniform neither in the poloidal direction, as an inner equatorial cut is present, nor in the toroidal direction, as a poloidal gap and a region where the two edge of the shell toroidally overlap are also present. The two gaps in the shell allow for the penetration of the axialsymmetric toroidal field b_φ and the axialsymmetric toroidal electric field.

Outside the stabilising shell, a toroidal structure provides the necessary mechanical support to the machine assembly, including 48 toroidal field coils, 8+8 field shaping coils and 192 local coils called *saddle coils*. In Figure 1.3 the picture of the vacuum vessel, shell and support structure assembly is presented. The saddle coils windings can be seen as the fourth element of the machine magnetic subsystem, the magnetising circuit, the toroidal coils and the field shaping coils being the first three. Overall, the maximum peak power of an RFX-mod pulse requires 200 MVA to be taken from the 400 kV 50 Hz Italian

Parameter	Value	Unit
Major Radius, R_0	2.0	m
Minor Radius, a	0.5	m
Maximum plasma current, I_p	2.0	MA
Maximum applied toroidal field, $b_{\varphi,0}$	0.7	T
Current rise time	$15 - 50$	ms
Flat top time	250	ms
Core flux swing	15	Vs
Inductive storage	72.5	MJ
Vacuum Vessel Toroidal resistance	1.1	mΩ

Table 1.1: RFX main parameters

grid.

These magnetic windings operate as described in the previous section. The magnetising winding is capable of applying an unipolar flux swing of 15 Wb, starting with an initial current load of about 10 MAturns (corresponding to a field of 4.5 T in the central bore) and producing a peak loop voltage of 700 V in some tens of milliseconds. This is required in the first phase of the plasma discharge, called *plasma ramp-up*, when the plasma has also to be heated by the ohmic effect. In RFX-mod the magnetising circuit is not a perfect rectilinear solenoid, because the position of its coils has been optimized in order to limit the stray field in the plasma region. The toroidal coils produce, during normal operations, a maximum toroidal bias field $b_{\varphi,0} = 0.7$ T at the beginning of the discharge and a reversed field at the wall $b_{\varphi,w} = 0.44$ T during the plasma current flat-top. The field shaping windings provides an accurately shaped vertical equilibrium field in order to obtain a precise control of the plasma position. This circuit presents a magnetomotive force equal to the plasma current (up to 2 MAturns) to reduce the flux swing requirements.

The saddle coils circuit falls into the category of the error field correction coils. Despite it has not been designed to provide such a functionality, it shares with those systems the most important geometrical characteristic of an error field windings, that is being local. This component of the RFX-mod magnetic system has been realised in order to implement an active control of the MHD instabilities. In particular for the control of the so called *resistive wall modes* (RWM). To accomplish its task, 192 independently fed coils have been installed in the machine. They are hosted by grooves conveniently cut on the outer surface of the toroidal support structure at $r = r_c = 0.582$ m and have been arranged as a bi-dimensional Cartesian grid of adjacent coils, as shown in Figure 1.4. Each coil is made of a copper thread wound up 60 times and has

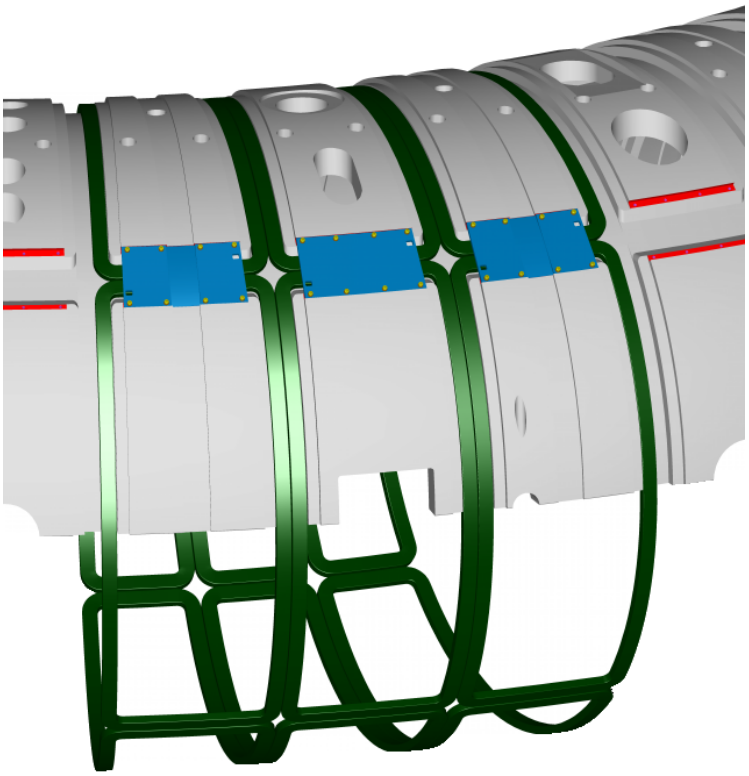

Figure 1.4: RFX-mod support structure and active coils.

four legs, two of them laying on a toroidal surface in the poloidal direction, the other two in the toroidal direction. The coils are placed tightly close together, so that a single groove hosts the legs of two poloidally or toroidally adjacent coils. Neglecting the size of their section, the interior surface of these coils is an exact covering of the toroidal surface they lay on. The grid can be subdivided into 48 poloidal arrays of 4 coils each or into 4 toroidal arrays each of 48 elements. Each coil spans a poloidal angle of 90 degrees and a toroidal angle of 7.5 degree. They are arranged so that the centre of mass of the first coil is placed exactly in the origin of the ϑ, φ coordinates. For this reason the four toroidal arrays, and the corresponding four coils in a poloidal array are referred to with the adjectives *outer*, *upper*, *inner* and *lower* when necessary.

For their shape and position, the saddle coils can produce a relatively strong local magnetic field with a substantially radial component in its neighbourhood. The coils are designed to carry a maximum current of 400 A for 300 ms producing a maximum local radial field b_r of about 50 mT. In the following

sections these coils will also be called *active* coils and *radial field* coils. This can not lead to confusion because the study of this magnetic system is the primary subject of the doctoral dissertation.

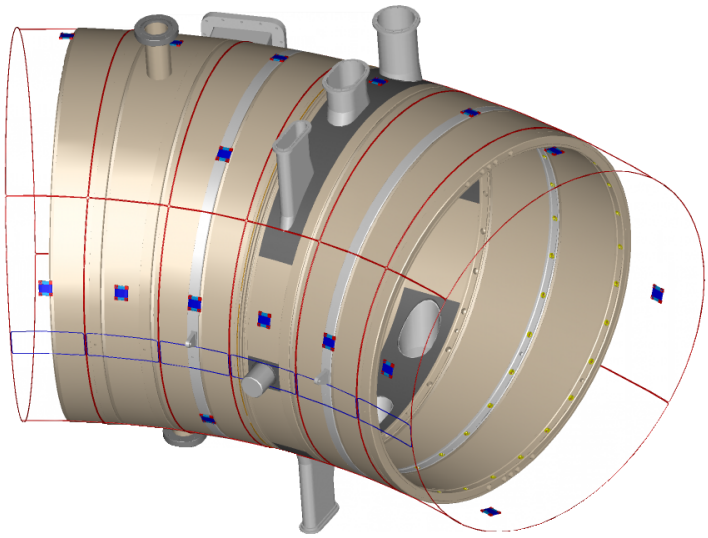

Figure 1.5: RFX-mod vessel and relative position of the radial sensors.

The RFX-mod magnetic field sensors are also of primary interest for the dissertation, in particular the integral radial field sensors laid down on the outer surface of the vacuum vessel at $r = 0.507$ m. These sensors are one-turn coils with a geometry analogous to the one of the active coils. They are placed, however, on a toroidal surface with an inferior radius. In Figure 1.5 the radial field sensors position together with the other poloidal and toroidal field pick-up coils on the vacuum chamber is shown.

The collection of a saddle coil, the sensor lying below it and eventually the power amplifier which feed it is called *MHD unit*.

1.3 The active system for the control of MHD instabilities

The collection of the RFX-mod machine assembly, with the saddle coils, their amplifiers, the radial field sensors and the electronic equipment represents the hardware of the RFX-mod *active system for the control of the MHD instabilities*. The system is of course also made of the electronic equipment needed

for the acquisition and processing of the relevant control variables. From a systemic point of view three components can be identified:

1. The power amplifiers feeding the saddle coils

2. The electromagnetic system made of the active coils, the radial sensors and the passive structures of the machine assembly

3. The control systems

These components are generally connected in a loop configuration: the voltages at the ends of the power amplifiers are the inputs of the radial magnetic system whose outputs are the fluxes measured by the sensors. The flux values are processed by control algorithms and resulting quantities are sent back to the power amplifiers as references or set points.

The details of the model of the amplifiers are not the subject of this dissertation, and only the essential information will be given. The power amplifiers themselves can be seen as a controlled dynamic system. They can operate in three different modalities, depending on their parameter configuration. They can be *voltage controlled*, *current controlled* or *flux controlled*. In the first case the power amplifiers control electronic interprets its input signals as a scaled voltage reference and the electronic gates of the power supply unit are controlled so as to present the associated output voltage. In the second case, the input signal is interpreted as a scaled current reference and the feedback controller implemented in the power amplifiers tries to drive a current following the reference. In the third case the, the input signal is interpreted as a flux reference. The controlled error signal is the difference between the reference and the flux measured by the underlying sensor.

The electromagnetic system is substantially inductive. It is made by 192 coils which can be interested by a current flow (the active coils), and 192 coils which are used as sensors (the radial field sensors). This set of 384 coils can be modelled as an ideal inductive 384-pole. That is the currents satisfy the relation

$$\begin{bmatrix} \boldsymbol{v}_1(t) \\ \boldsymbol{v}_2(t) \end{bmatrix} = \begin{bmatrix} \mathbf{M}_{11} & \mathbf{M}_{12} \\ \mathbf{M}_{21} & \mathbf{M}_{22} \end{bmatrix} \frac{d}{dt} \begin{bmatrix} \boldsymbol{i}_1(t) \\ \boldsymbol{i}_2(t) \end{bmatrix} + \begin{bmatrix} \mathbf{R}_{11} & \mathbf{0} \\ \mathbf{0} & \mathbf{R}_{22} \end{bmatrix} \begin{bmatrix} \boldsymbol{i}_1(t) \\ \boldsymbol{i}_2(t) \end{bmatrix} \tag{1.6}$$

where $\boldsymbol{v}$ and $\boldsymbol{i}$ denotes respectively voltage and current vector. The index 1 refers to the active coils, index 2 to the sensors. $\mathbf{M}_{ij}$ are partitions of a global inductance matrix, while $\mathbf{R}_{ii}$ are diagonal resistance matrices.

The voltage at the ends of the sensor coils is integrated to produce the flux measure. The integrating electronic is assumed to have a very small effect

on the measured system so that the relation $\boldsymbol{i}_2(t) = \mathbf{0}$ is reasonable. This consideration lead to the equations

$$\begin{array}{rcl} \boldsymbol{v}_1(t) & = & \mathbf{M}_{11}\frac{d}{dt}\boldsymbol{i}_1(t) + \mathbf{R}_{11}\boldsymbol{i}_1(t) \\ \boldsymbol{\psi}_2(t) & = & \mathbf{M}_{21}\boldsymbol{i}_1(t) \end{array} \tag{1.7}$$

where $\psi(t)$ is the flux vector measured by the radial field sensors.

These equations, however, are correct only in a space free of passive structures. In their presence a linear multiple-input-multiple-output model of the relation between the input voltages and the output fluxes can still be derived, but require more effort in the modelling, and the resulting transfer matrices result to be frequency dependent. This holds true even for the transfer function matrix linking the input coil currents to the output flux vectors, which would be constant in the absence of passive structures.

The components $\mathbf{M}_{11}$ and $\mathbf{M}_{21}$ of the global inductance matrix have been central to this doctoral dissertation. A state space model of the transfer function matrix $\mathbf{M}_{21}(j\omega)$, called also $\mathbf{M}(j\omega)$ in the following, and a model of the transfer function relating the saddle coils input voltages to the currents flowing in them has been derived. $\mathbf{M}_{11}$ plays a role in the latter derivation.

1.3.1 Nomenclature

A common naming convention has to be adopted for the clear identification of each entity in the set of the active coils and radial field sensors. In the case of this system, however, more than one naming convention emerged, used on the base of their convenience. At first sight labelling each coil naturally with a number from 1 to 192 following a particular geometrical order seems to be the most clear solution. This also makes sense from the point of view of the implementer of the control system, for whom each entity measure is a component of a vector stored somewhere in the controller memory. From other points of view, however, other naming conventions seems to be more adequate. For example when performing the spatial spectral analysis of a quantity measured by the system[2] the quantity itself is intrinsically bi-dimensional. In this case labelling with pairs in the set $\{1, 2, \ldots, 48\} \times \{1, 2, 3, 4\}$ provides more insight of how things work. Other naming conventions are in use at the RFX site in particular for the coils power amplifiers. These are in use because are the most obvious from the point of view of the power supply expert. The naming conventions more suitable for the present document are described below.

In the *bi-dimensional* nomenclature, to each sensor, active coil and relative amplifier is assigned a pair of numbers from the set $\{1, 2, \ldots, 48\} \times \{1, 2, 3, 4\}$.

[2]This kind of analysis will be described in the following chapter

The first number in the pair is called *toroidal index*, the second *poloidal index*. The pair (1,1) is assigned to the sensor and active coil surrounding the half line $\vartheta = 0$, $\varphi = 0$. The pair (1,2) is assigned to the sensor and active coil surrounding the half line described by $\vartheta = \frac{1}{2}\pi$, $\varphi = 0$ and so on. The pair (2,2) is assigned to the coil and sensor linked to the $\vartheta = \frac{1}{2}\pi$, $\varphi = \frac{1}{24}\pi$ half line and so on. In other words each coil is identified by two indices: the first one is the index of a poloidal array whereas the second one is the index of a toroidal array. The toroidal and poloidal indices are discrete coordinates corresponding to the continuous coordinates. The position of the "centre" of the (i, j) coil is $\vartheta = (j-1)\frac{\pi}{2}$, $\varphi = (i-1)\frac{\pi}{24}$. The nomenclature is extended also to the relative coil power amplifier.

In the *progressive* nomenclature to each sensor, active coil, and corresponding amplifier is assigned a single number, called *progressive index*, varying from 1 to 192. Mathematically the progressive index p can be calculated from the toroidal index i and poloidal index j using the formula

$$p = 4(i-1) + j. \tag{1.8}$$

In other words the progressive nomenclature labels the sensors, coils and relative amplifiers by counting them in poloidal major order. The toroidal and poloidal indices can be calculated from the progressive index using the relations

$$\begin{aligned} i &= \text{floor } (p-1)/4 + 1 \\ j &= \text{mod } (p-1, 4) + 1. \end{aligned} \tag{1.9}$$

Chapter 2

Analysis of the RFX-mod MHD system

2.1 Introduction

This chapter concerns the formal description of the RFX-mod active system for the control of the MHD instabilities and its analysis, from the point of view of the System and Signal Theory. Particular attention has been paid to the description of its intrinsic sampling mechanisms and in relation with the toroidal geometry.

In the following section are introduced the mathematical language and the tools needed to describe the active system from a systemic point of view, relaying on standard concepts of the System and Signal Theory. In particular the language of the Unified Signal Theory developed by Professor Gianfranco Cariolaro of the Padova University is used. After the most important concepts of this theory have been recalled, the analysis of the sampling components of the system is presented. The analysis shows how the spatial harmonic content of physical quantities such as the poloidal sheet current density $\boldsymbol{J}_p$ and the radial magnetic field b_r are affected by the sampling performed by the sensors. An integral parameter Λ, summarising the importance of the toroidal effect, is proposed.

2.2 Summary of the Unified Signal Theory

The Unified Signal Theory is an abstract formulation of signals and systems. It has been developed starting from few basic concepts, and it then results to be a general theory applicable to a wide class of signals and systems. As the reference textbook for the Unified Signal Theory is, at the moment, only

published in Italian language, in order to provide the reader with a general understanding of the theory, a summary of it is presented in this section. The reader should keep in mind, however, that the purpose of this summary is to provide the information required to understand the specific analysis carried out in the rest of this dissertation, not to provide a complete survey of the Unified Theory. Further details of the theory, results and examples which are useful for its understanding, can be found in [6], which is the reference textbook of the Unified Signal Theory.

2.2.1 Regular groups

The key of the unification is the formal definition of signal, which is based on algebraic structures called *locally compact Abelian groups*. The elements of this class are those mathematical objects which are, at the same time, both a locally compact topological space and an Abelian group with continuous group operation with respect of the topology [7]. Locally compact Abelian groups are referred to, in the following, as *regular groups* for brevity[1]. In other words the regular groups are the Abelian groups which, at the same time, are also locally compact *topological spaces*. The concept of regular group is logically at the very bottom of the Unified Signal Theory and the study of the structures of these groups is central to its development.

Elementary regular groups are $\mathbb{R}$, $\mathbb{Z}$ and $\mathbb{O}$. The latter is the trivial group containing only the neutral element. $\mathbb{Z}(T)$, the set $\{nT : n \in \mathbb{Z}\}$, $T \in (0, \infty)$ is also a fundamental regular group. Other groups, denoted by U/S, are those obtained as quotients of a regular group U and one of its regular subgroups $S \subset U$. A result of the topological group theory assures that the quotient group formed in that way is always a regular group. Every group U can always be represented as a quotient group by means of the trivial group, which is always contained in every regular group. For example R can be expressed as $\mathbb{R}/\mathbb{O}$ and the trivial group as U/U for every group U. This means that the category of the quotient groups contains the one of the non-quotient groups. In the following the word group is used to refer to the class of the quotient groups. Regular groups can also be constructed by taking the Cartesian product of two regular groups. This fact has been used extensively in this chapter. Finally regular groups can be constructed using *isomorphisms* between regular groups.

It is a fundamental result of Topology that

Theorem 2.2.1. *Every regular group G is isomorphic to a group of $\mathbb{R}^m$ in the*

[1] In should be stressed that in this context "regular" is merely a placeholder for the locution "locally compact Abelian" and nothing else.

form

$$G \sim \mathbb{R}^p \times (\mathbb{R}/\mathbb{Z})^q \times \mathbb{Z}^r \times \mathbb{Z}/\mathbb{Z}(N_1) \times \cdots \times \mathbb{Z}/\mathbb{Z}(N_s) \tag{2.1}$$

for convenient p,q,r,s and $N_1, \ldots, N_s \in \mathbb{N}$.

This theorem states that the structure of every possible regular group is completely known and having reference to the structure of simpler, elementary groups. This theorem is used in the theory to develop the concepts of *base*, *signature* and *representation* of a regular group. These concepts are important for the development of the theory and in the characterisation of the regular subgoups of $\mathbb{R}^n$. However, for the purpose of this dissertation, their definition can be omitted.

2.2.2 Definition of signal

Equally important to the Unified Theory is the formal definition of signal, which, as has been mentioned before, relies on the concept of regular group.

Definition A signal is a function from a regular group U into the set of the complex numbers.

$$s : U \to \mathbb{C} \tag{2.2}$$

Regular groups are important for the Unified Theory because they allow the definition of a non-trivial *operator* acting on signals which is linear and invariant to translations.

2.2.3 Periodicity and cells

Regular groups are also used in the Unified Theory to express the concept of periodicity. Formally, every regular sub-group P of a regular group U selected for this purpose is called *periodicity* of the group U. In general, signals with periodicity P have the property that the signal value at u is the same of the signal value at $u + p$, for all the $p \in P$. That is,

$$s(u) = s(u + p)\ \forall u \in U,\ \forall p \in P. \tag{2.3}$$

The concept of periodicity is linked to the idea of *cell*, the generalisation of the period.

Definition A cell of the group U modulo P is a subset C of U so that

$$C + P = U \tag{2.4}$$

and, for every $p_1, p_2 \in P$, the relation

$$(C + p_1) \cap (C + p_2) = \varnothing \Leftrightarrow p_1 \neq p_2 \tag{2.5}$$

holds. A cell of U modulo P is denoted with the symbol $[U/P)$.

In other words, the subsets family generated by shifting a cell $[U/P)$ of elements in P a *partition* of U.

In the Unified Theory quotient groups are often interpreted as the couple group/modulo, instead of normal groups. This is possible because signals defined on U with periodicity P are always in a one to one correspondence with the signals defined over the quotient group U/P. This correspondence can easily be established making use of the following proposition, which is proved in the appendix.

Proposition 2.1. *For every cell $C = [U/P)$ there exist a one to one mapping $\mu : C \to U/P$ from C to the quotient group U/P.*

2.2.4 The Haar integral

On every regular group U it is possible to define a measure, the Haar measure, from which an integral operator can be constructed. This operator is called *Haar integral* and it is denoted, in this dissertation, by the usual integral symbol, as shown in the equation below.

$$\int_U s(t)dt \tag{2.6}$$

The Haar integral has the properties of being not identically zero for all signals, linear and invariant to a shift of the signal, that is obeying to the equation

$$\int_U s(t)dt = \int_U s(t-u)dt, \quad \forall u \in U. \tag{2.7}$$

A fundamental result of the theory of locally compact groups is the proof of the existence and uniqueness of this integral.

Theorem 2.2.2. *On every regular group it is possible to define a non-trivial integral operator invariant to signal translations. This integral is unique up to a multiplicative constant.*

By using this theorem an integral operator can quickly be checked to be a correct Haar integral. Generally the Haar integral of a regular group is found by checking if a given operator satisfies the above properties. For example the

Lebesgue integral on $\mathbb{R}$ is also an Haar integral. The expressions of the Haar integral for the most common regular groups are shown in table 2.1.

On the regular groups a special "function", called *delta* or *impulse* and denoted by $\delta_U(\boldsymbol{u})$ in the case of the group U, can be defined. This fundamental "signal" is characterised by the following property

$$\int_U \delta_U(\boldsymbol{t}-\boldsymbol{u})s(\boldsymbol{u})d\boldsymbol{u} = s(\boldsymbol{t}). \tag{2.8}$$

In the case of regular groups isomorphic to $\mathbb{R}$ or $\mathbb{R}/\mathbb{Z}$, $\delta_U(\boldsymbol{u})$ is the Dirac Delta (which is a distribution and not a function), whereas in the case of groups isomorphic to $\mathbb{Z}$ or $\mathbb{Z}/\mathbb{Z}(N)$ it is a function which is zero everywhere in U $\mathbf{0}$.

	Haar integral	Expression
1)	$\int_{\mathbb{R}} s(t)dt$	$\int_{-\infty}^{+\infty} s(t)dt$
2)	$\int_{\mathbb{Z}(T)} s(t)dt$	$T\sum_{n=-\infty}^{\infty} s(nT)$
3)	$\int_{\mathbb{R}/\mathbb{Z}(T)} s(t)dt$	$\int_0^T s(t)dt$
4)	$\int_{\mathbb{Z}(T)/\mathbb{Z}(NT)} s(t)dt$	$T\sum_{n=0}^{N-1} s(nT)$

Table 2.1: Expressions of the Haar integral corresponding to common regular groups.

2.2.5 Linear systems and convolution

The Haar integral is used in the Unified Theory to define in a general way the concept of *linear transformation*. A couple of multidimensional signals $\boldsymbol{u}(\boldsymbol{t}_1)$ with $\boldsymbol{t}_1$ taking values in U and $\boldsymbol{y}(\boldsymbol{t}_2)$ with $\boldsymbol{t}_2$ taking values in V, tied by the following equation

$$\boldsymbol{y}(\boldsymbol{t}_2) = \int_U \mathbf{H}(\boldsymbol{t}_2,\boldsymbol{t}_1)\boldsymbol{u}(\boldsymbol{t}_1)d\boldsymbol{t}_1, \tag{2.9}$$

are said to be, respectively, the input and the output of a linear transformation or *system*. The function matrix $\mathbf{H}(\boldsymbol{t}_2, \boldsymbol{t}_1)$ is defined over the Cartesian product $U \times V$ and it is called the *kernel* of the transformation.

The presented definition is the most general definition of linear system as it applies to variant, non-causal and multiple-input-multiple-output systems. The details of the use and meaning of such an operator depending on the relationship between the input domain U and the output domain V have been developed in the framework of the Unified Theory and can be found in the book [6].

In case the signals are not multidimensional the signals and the kernel of the above equation are written using normal letters instead of the bold ones, as below.

$$y(\boldsymbol{t}_2) = \int_U h(\boldsymbol{t}_2, \boldsymbol{t}_1) u(\boldsymbol{t}_1) d\boldsymbol{t}_1 \tag{2.10}$$

If the transformation kernel satisfies the following property

$$h(\boldsymbol{t}_2 + \Delta\boldsymbol{t}, \boldsymbol{t}_1 + \Delta\boldsymbol{t}) = h(\boldsymbol{t}_2, \boldsymbol{t}_1) \tag{2.11}$$

for every $\Delta\boldsymbol{t} \in U$, which requires the domains U and V to share a common group operation, the system is called *quasi invariant*. If U and V are the same group it is *strictly invariant*. The invariance of a transformation is an important property which determines simplifications in the analysis of systems. Invariant counterparts of variant systems, for example, requires to define their kernel in a group with half of the dimensions. Also the Fourier analysis of the signals is simplified for invariant systems. Most of the results of the System and Signal Theory used in the engineering applications regards the class of the invariant transformations. By letting $\Delta\boldsymbol{t} = -\boldsymbol{t}_1$ in the above equation, the kernel of an invariant transformation can always be written in the form[2]

$$h(\boldsymbol{t}_2 - \boldsymbol{t}_1) = h(\boldsymbol{t}_2 - \boldsymbol{t}_1, \mathbf{0}). \tag{2.12}$$

Despite the relevance of the invariant or quasi invariant transformations, for the present dissertation some results regarding the variant transformation are required. They are recalled in the next section and proved in the appendix.

2.2.6 Dual domains

The definition of *dual* of a regular group U is used in the development of a general Fourier analysis based on the topological group theory. Dual groups,

[2]When different functions are used for semantically equivalent purposes, if they can be discriminated by the number or type of their arguments, they are denoted with the same symbol.

	Group	Dual
1)	U	$\hat{U}$
2)	$U_1 \times U_2$	$\hat{U}_1 \times \hat{U}_2$
3)	$\mathbb{R}$	$\mathbb{R}$
4)	$\dfrac{\mathbb{R}}{\mathbb{Z}(T)}$	$\mathbb{Z}(1/T)$
5)	$\mathbb{Z}(T)$	$\dfrac{\mathbb{R}}{\mathbb{Z}(1/T)}$
6)	$\dfrac{\mathbb{Z}(T)}{\mathbb{Z}(NT)}$	$\dfrac{\mathbb{Z}(1/NT)}{\mathbb{Z}(1/T)}$
7)	$\dfrac{\mathbb{R}}{\mathbb{Z}(2\pi)} \times \dfrac{\mathbb{R}}{\mathbb{Z}(2\pi)}$	$\mathbb{Z}(1/2\pi) \times \mathbb{Z}(1/2\pi)$
8)	$\dfrac{\mathbb{Z}(2\pi/N_1)}{\mathbb{Z}(2\pi)} \times \dfrac{\mathbb{Z}(2\pi/N_1)}{\mathbb{Z}(2\pi)}$	$\dfrac{\mathbb{Z}(1/2\pi)}{\mathbb{Z}(N_1/2\pi)} \times \dfrac{\mathbb{Z}(1/2\pi)}{\mathbb{Z}(N_2/2\pi)}$

Table 2.2: Common regular groups and their duals. Parameter $T \in \mathbb{R} \setminus \{0\}$, $N \in \mathbb{Z} \setminus \{0\}$.

denoted with a hat on the group symbol as in $\hat{U}$, are important because they are the natural domain of the Fourier transform of signals. The logical derivation of the concept of dual starts from the definition of *character* of a regular group. The set of all the possible characters of a group turns out to be itself a regular group. In this case the standard function multiplication is selected as the group operation. The existence of the inverse for each character, the existence of the neutral element and the closure of the set under the group operation are easily established directly from the above definition. For example the neutral element is the constant function 1. This multiplicative regular group is topologically isomorphic to an additive regular group which is, by definition, the dual of the original group. The construction of dual groups through the notion of characters is, however, used only in the development of the mathematical theory. From the practical points of view, the identification of the dual of a regular group is made by applying convenient results of the Unified Theory. This method is based on the concept of *reciprocal* group. The interesting identities involving the concept of dual group for the present dissertation are reported in Table 2.2.

	Signal	Fourier transform
1)	$s(\boldsymbol{t})$	$S(\boldsymbol{f})$
2)	$s\left(\frac{\boldsymbol{t}-\boldsymbol{t}_0}{T}\right)$	$Te^{-j2\pi\boldsymbol{f}\cdot\boldsymbol{t}_0}S(T\boldsymbol{f})$
3)	$s_1(\boldsymbol{t})s_2(\boldsymbol{t})$	$\int_{\hat{U}} S_1(\boldsymbol{f}-\boldsymbol{\nu})S_2(\boldsymbol{\nu})d\boldsymbol{\nu}$
4)	$\delta_U(\boldsymbol{t})$	1
5)	1	$\delta_{\hat{U}}(\boldsymbol{f})$

Table 2.3: Properties of the generalised Fourier transform.

2.2.7 Fourier transform

The generalised Fourier transform of a signal s over the domain U is defined as the following Haar integral

$$S(\boldsymbol{f}) = \mathcal{F}[s(\boldsymbol{t})](\boldsymbol{f}) = \int_U s(\boldsymbol{t})e^{-2\pi\boldsymbol{f}\cdot\boldsymbol{t}}d\boldsymbol{t}, \tag{2.13}$$

where the variable $\boldsymbol{f}$ belongs to $\hat{U}$, the dual of U.

In the Table 2.3 are presented some relationship between signal and Fourier transform used in the rest of the document. The signals in the left column of the table are defined on the regular group U, therefore the Fourier transforms on the right are defined on $\hat{U}$. Signals are denoted with lowercase letters whereas their Fourier transforms are denoted with the corresponding uppercase letters. In the third and fourth rows of the table are recalled the formulas for the Fourier transform of the shifted and stretched version of a signal and for the product of two signals. The last two rules are important relationship linking identity and Delta function on group and its dual.

Another important couple signal-transform used in the the following analysis is

$$\mathcal{F}[\mathrm{rect}(t)](f) = \mathrm{sinc}\, f, \tag{2.14}$$

which relates the signals rect(t) and sinc(f) defined below.

$$\text{rect}(t) = \begin{cases} 1 & \text{if } |t| < \frac{1}{2} \\ \frac{1}{2} & \text{if } |t| = \frac{1}{2} \\ 0 & \text{if } |t| > \frac{1}{2} \end{cases} \quad t \in \mathbb{R}, \tag{2.15}$$

$$\text{sinc}(f) = \frac{\sin(\pi f)}{\pi f} \; f \in \mathbb{R}. \tag{2.16}$$

2.3 Time variant filtering

Some standard results of the Signal Theory about the invariant filtering have to be extended to the non-invariant (or *variant*) case in order to be used in the following calculations. A first proposition shows the mathematical relation between the Fourier transforms of signals which are connected by a variant filter.

Proposition 2.2. *Given a time variant system $g(\boldsymbol{t}_1, \boldsymbol{t}_2)$ transforming the input signal $u(\boldsymbol{t}_1)$ defined over the domain U into the corresponding output signal $v(\boldsymbol{t}_2)$ defined over the same domain by the law*

$$v(\boldsymbol{t}_2) = \int_U g(\boldsymbol{t}_1, \boldsymbol{t}_2) u(\boldsymbol{t}_1) d\boldsymbol{t}_1 \tag{2.17}$$

the Fourier transform of $u(\boldsymbol{t}_1)$, $v(\boldsymbol{t}_2)$ and $g(\boldsymbol{t}_1, \boldsymbol{t}_2)$, respectively $U(\boldsymbol{f}_1)$, $V(\boldsymbol{f}_2)$ and $G(\boldsymbol{f}_1, \boldsymbol{f}_2)$, are related by the equation

$$V(\boldsymbol{f}_2) = \int_{\hat{U}} G(-\boldsymbol{f}_1, \boldsymbol{f}_2) U(\boldsymbol{f}_1) d\boldsymbol{f}_1 \tag{2.18}$$

The importance of this result lays in the fact that the studied system is actually variant with respect of several aspects. The Fourier transform of the output signal is therefore obtained by the convolution of the Fourier transform of the input signal and the Fourier transform of the filter. This means that the harmonic content of the input signal is not only *distorted* by the variant filter, but also new harmonic content can be introduced by the filter.

A second result shows the mathematical expression of the dual shape of an invariant filter when it is treated with the variant theory. It is interesting because it is used in the definition of the parameter Λ given in the following section.

Proposition 2.3. *Given a function g of two vectorial variables $\boldsymbol{t}_1, \boldsymbol{t}_2 \in U$ such that for every $\boldsymbol{d} \in U$ $g(\boldsymbol{t}_1 + \boldsymbol{d}, \boldsymbol{t}_2 + \boldsymbol{d}) = g(\boldsymbol{t}_1, \boldsymbol{t}_2)$, its Fourier transform is*

$$G(\boldsymbol{f}_1, \boldsymbol{f}_2) = \delta_{\hat{U}}(\boldsymbol{f}_1 + \boldsymbol{f}_2) G_r(\boldsymbol{f}_2) = \delta_{\hat{I}}(\boldsymbol{f}_1 + \boldsymbol{f}_2) G_r(-\boldsymbol{f}_1) \tag{2.19}$$

where

$$G_r(\boldsymbol{f}_2) = \int_U g(\boldsymbol{0}, \boldsymbol{\tau}) e^{j2\pi \boldsymbol{f}_2 \boldsymbol{\tau}} d\boldsymbol{\tau} \tag{2.20}$$

The proofs of these propositions can be found in the appendix.

2.4 MHD system analysis

In this analysis the RFX-mod active system for the control of the MHD instabilities, also referred to as the *MHD system* hereafter, has been considered. It is assumed to consist only of the 192 saddle coils, the machine passive structures and the 192 radial field sensors. The intensities of the currents in the saddle coils are supposed to be independent variables. This is reasonable, because they are independently fed by 192 power amplifiers.

The MHD system is seen as a particular magnetic field source with 192 degree of freedom. Moreover, the resulting magnetic field is assumed to depend linearly on the source currents. Such a device can be conveniently modelled as a dynamic system in the frame of the System Theory. However, instead of describing the system from that point of view, in the following it is analysed using the results of the Unified Signal Theory recalled in the previous section.

In the field of System Theory the MHD system would be classified as a multi-input-multi-output (MIMO) dynamic system. The 192 current intensities would be the *inputs* of the system, whereas the 192 flux measures would be its *outputs*. The values of these measures would be arranged in row vectors, respectively $\boldsymbol{i}(t)$ and $\boldsymbol{\psi}(t)$, and the linear dynamic relationship between them represented with the following integral transformation.

$$\boldsymbol{\psi}(t) = \int_{\mathbb{R}} \mathbf{M}(u - t) \boldsymbol{i}(u) dt \tag{2.21}$$

The elements of the 192×192 matrix $\mathbf{M}(\tau)$ would be real functions defined on $\mathbb{R}$ having the property of being causal impulse responses. The System Theory focuses on the structure of the mathematical representation of the dynamic system, that is on the shape of the function $\mathbf{M}(\tau)$. The use of such a representation is common, useful and it is at the base of the work described in chapters 3 and 4. In spite of that, however, the approach described by the

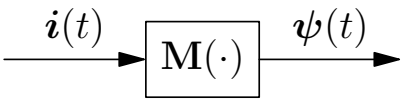

Figure 2.1: Block diagram representing the MHD system as a single MIMO transformation.

Unified Signal Theory has been found fruitful for the purpose of analysing the MHD system. In this view, the focus is on the structure of the domains used in he definition of the interacting signals.

The subject of this dissertation, the MHD system, is a nice example of how the System Theory can miss to capture relevant information about the nature of a dynamic system. Traditionally, the System Theory developed two branches where the continuous and discrete systems has been considered separately. Inside these two branches the domain structure of the signal has not received particular attention, essentially because there was no need. The domain of the signal was an invariant: $\mathbb{R}$ for the continuous and $\mathbb{Z}(T)$ for the discrete systems. In this study, instead, signal domains play a central role. The exigence of performing spatial harmonic analysis, sampling and interpolation of bi-dimensional quantities, made the choice of adopting the approach suggested by the Unified Signal Theory almost natural.

2.4.1 Block diagrams

According to equation (2.21), the MHD system can be represented mathematically by a single MIMO dynamic system. This situation is illustrated in figure 2.1. The symbol $\cdot$ is used in this context to denote the presence of a variable without specifying it with a symbol. This allows to save symbols while retaining the information on the structure of the transformation and the logical rigor of the notation. Despite black box models can reproduce with accuracy the relations between input and output ports of dynamic systems, such a feature is not sufficient, in this case, for developing a clear understanding of its *spatial harmonic* properties. To obtain this knowledge, a more convenient representation of the system has to be adopted, consisting of 2 blocks connected in series. The operation of splitting the MHD system model into two smaller components requires the introduction of a reference surface on which the value of the magnetic field is considered. For this purpose the toroidal surface corresponding to the position of the radial field sensors has been chosen. This surface is labelled T_s and is described by the equation $r = r_s = 0.507$ m. The resulting model consists of the block $\mathbf{h}(\cdot)$, describing how the current intensi-

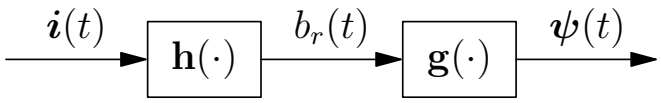

Figure 2.2: Block diagram of the MHD system showing 2 of its components: the interpolation $\mathbf{h}(\cdot)$ and the sampling $\mathbf{g}(\cdot)$.

ties generate the magnetic field, and $\mathbf{g}(\cdot)$, describing how the magnetic field distribution is transformed into the flux measurements. Figure 2.2 shows the resulting block diagram. From the point of view of the Unified Signal Theory, they are respectively *interpolating* and *sampling* filters. This decomposition is important because it makes clear the relationship between the produced magnetic field and the *measured* current intensities and field fluxes. The magnetic field is a fundamental quantity either for plasma physicists and for control engineers because it can directly affect the plasma evolution. For its continuous nature, its shape on the selected surface can be integrally known only in particular circumstances, when it can be reconstructed from the available set of measurements.

2.4.2 Domains definition

Following the approach of the Unified Theory, all the quantities appearing in Figure 2.2 are considered to be signals. As recalled in the previous section this means that they are considered to be complex functions defined over regular groups. In this section the structure of the groups used for the analysis is commented. As described in Chapter 1, the MHD system consists of a number of MHD units, assembled on the machine as a bi-dimensional grid with $N_1 = 4$ toroidal arrays and $N_2 = 48$ poloidal arrays. Conceptually the quantities $\boldsymbol{i}(t)$, $b_r(t)$ and $\boldsymbol{\psi}(t)$ are not signals because the functions $\boldsymbol{i}(t)$ and $\boldsymbol{\psi}(t)$ are n-utple[3] and $b_r(t)$, denoting the radial field distribution on T_s, is a function, that is they are not single complex numbers as required by the definition of signal.

Indeed, these quantities have in common the fact of depending, apart on the time, also on other variables which have not yet been made explicit and that can be used to cast them into signals. This is made introducing the Cartesian groups

$$U = \frac{\mathbb{Z}(2\pi/N_1)}{\mathbb{Z}(2\pi)} \times \frac{\mathbb{Z}(2\pi/N_2)}{\mathbb{Z}(2\pi)} \times \mathbb{R} \tag{2.22}$$

[3]The Unified Theory would define them *multidimensional* signals. Looking at them as a mere collection of signals prevents performing the spatial biharmonic analysis.

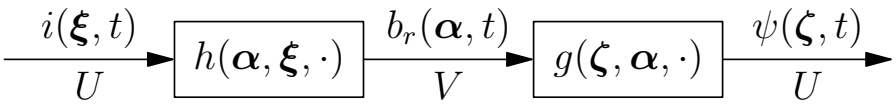

Figure 2.3: Interpolating and sampling filters. Domain of the signals shown explicitly.

and

$$V = \frac{\mathbb{R}}{\mathbb{Z}(2\pi)} \times \frac{\mathbb{R}}{\mathbb{Z}(2\pi)} \times \mathbb{R} \tag{2.23}$$

as domains for the above quantities. In both of them the first two factors are used to represent spatial coordinates while the last one is used to represent the time coordinate t. As this analysis is not focused on the behaviour of the MHD system with respect of the time, in the time dependence is sometimes dropped. This is acceptable because system is assumed to be time-invariant and it is meaningful, for the scope of the analysis, working at fixed time. When this simplification is made the above domains become

$$U_L = \frac{\mathbb{Z}(2\pi/N_1)}{\mathbb{Z}(2\pi)} \times \frac{\mathbb{Z}(2\pi/N_2)}{\mathbb{Z}(2\pi)} \tag{2.24}$$

and

$$V_L = \frac{\mathbb{R}}{\mathbb{Z}(2\pi)} \times \frac{\mathbb{R}}{\mathbb{Z}(2\pi)}. \tag{2.25}$$

The structure of U_L, which is a finite group, is a consequence of the fact that the number of variables to be represented is limited. Its specific shape, in particular the choice of the basis $(2\pi/N_1, 0)$, $(0, 2\pi/N_2)$, is dictated by the need of assuring the rational comparability of the two groups and the convenience of adopting the periodicity $\mathbb{Z}(2\pi) \times \mathbb{Z}(2\pi)$ for V_L which is natural in the toroidal coordinates. The scheme of the system with the notation of the unified approach is presented in Figure 2.3. Boldface letter such as $\boldsymbol{\xi}$, $\boldsymbol{\alpha}$ and $\boldsymbol{\zeta}$ are used to denote the vectorial quantities (ξ_1, ξ_2), (α_1, α_2) and (ζ_1, ζ_2) respectively. α_1 is the poloidal coordinate (ϑ), α_2 is the toroidal coordinate (φ). The components of $\boldsymbol{\xi}$ and $\boldsymbol{\zeta}$ represents lattice counterparts of the continuous variables.

2.4.3 Current distribution

The multidimensional signals such as the vector of the current intensities of the MHD system do have, in general, a degree of freedom in the choice of their domain, which turns out to be not fixed a priori. For example, the above currents can be considered as a collection of 192 signals on $\mathbb{R}$, a signal on $\mathbb{Z}/\mathbb{Z}(192) \times \mathbb{R}$

or a signal on U. The choice of the domain structure has to be made considering other available information on the system such as the constraints on the type of harmonic analysis, if any, that has to be performed on the signal. So, considering the examples just mentioned, in the first case no spatial harmonic analysis is possible, because the domain is spatially unstructured[4], in the second case a mono-dimensional spatial harmonic analysis is possible whereas in the third a bi-dimensional spatial harmonic analysis become feasible.

The vector of the current intensities of the MHD system can be interpreted as a discrete bi-dimensional distribution in the sense that it is possible to devise a sampling scheme of a continuous bi-dimensional quantity where the currents turns out to be samples. This can be seen considering a continuous laminar current density, $\boldsymbol{J}_p(\boldsymbol{\alpha}, t)$, on the toroidal surface T_c corresponding to the saddle coils radius $r_c = 0.582$ m. The harmonic content of this bi-dimensional signal can be defined without ambiguities because the poloidal and toroidal components are not independent assuming the current solenoidality[5]. Somehow arbitrarily, the harmonic content of $\boldsymbol{J}_p(\boldsymbol{\alpha}, t)$ is then defined to be the one of its poloidal component. The current density is then sampled with a $N_1 \times N_2$ grid of sensors. Without entering the details, one way of implementing this sampling system is considering a small arc, $L(\boldsymbol{\gamma})$, as a reference boundary for the current measurement. This arc is placed on the toroidal surface T_c along the toroidal direction. Its length, $l(\boldsymbol{\gamma})$, is an approximation of the toroidal width of the saddle coil section. A discrete variable $\boldsymbol{\xi}$ belonging to the group set U_L is used for the definition of the discrete signal and corresponds to the continuous variable $\boldsymbol{\gamma}$ taking values in V_L. The probes are placed poloidally at angles $\gamma_1 = \xi_1$ and centered toroidally at angles $\gamma_2 = \xi_2 - \pi/N_2$.

In toroidal coordinates the measure of the current flowing through the arc is expressed by the following integral

$$i(\boldsymbol{\xi}, t) = \int_{L(\boldsymbol{\xi})} \boldsymbol{J}_p(\boldsymbol{\alpha}, t)\hat{\boldsymbol{n}} dl. \tag{2.26}$$

defining the function $f(\boldsymbol{\gamma}, \boldsymbol{\alpha})$ as

$$f(\boldsymbol{\gamma}, \boldsymbol{\alpha}) = \frac{R_0}{\Delta\alpha_2}(1 + a_c \cos(\alpha_1))\delta(\alpha_1 - \gamma_1)\,\mathrm{rect}\left(\frac{\alpha_2 - \gamma_2 + \pi/N_2}{\Delta\alpha_2}\right) \tag{2.27}$$

the currents can be expressed as a linear transformation which is a sampling

[4]From the harmonic analysis, in this case, is not possible to obtain more than a collection of time frequency responses.

[5]This would not be the case if the current density had been tri-dimensional.

from V_L to U_L

$$i(\boldsymbol{\xi}) = \iint_{V_L} f(\boldsymbol{\xi}, \boldsymbol{\alpha}) J_\vartheta(\boldsymbol{\alpha}) d\boldsymbol{\alpha}. \tag{2.28}$$

In case the output quantity had been the mean current density $< \boldsymbol{J}_p(\boldsymbol{\xi}) >$ the filter would have been

$$\hat{f}(\boldsymbol{\xi}, \boldsymbol{\alpha}) = \frac{1}{\Delta\alpha_2} \frac{1 + a_c \cos(\alpha_1)}{1 + a_c \cos(\xi_1)} \delta(\alpha_1 - \xi_1) \operatorname{rect}\left(\frac{\alpha_2 - \xi_2 - \pi/N_2}{\Delta\alpha_2}\right) \tag{2.29}$$

and the linear transformation

$$< J_\vartheta > (\boldsymbol{\xi}) = \iint_{V_L} \hat{f}(\boldsymbol{\xi}, \boldsymbol{\alpha}) J_\vartheta(\boldsymbol{\alpha}) d\boldsymbol{\alpha}. \tag{2.30}$$

2.4.4 Field interpolation

It is natural now modelling the relation between the discrete current distribution $i(\boldsymbol{\xi}, t)$ and the flux distribution $b_r(\boldsymbol{\alpha}, u)$ using the integral linear transformation of the Unified Theory

$$b_r(\boldsymbol{\alpha}, u) = \int_U h(\boldsymbol{\alpha}, u, \boldsymbol{\xi}, t) i(\boldsymbol{\xi}, t) d\boldsymbol{\xi}, \tag{2.31}$$

with $h(\boldsymbol{\alpha}, u, \boldsymbol{\xi}, t)$ the kernel of the transformation. Assuming the *time* invariance of the system a slight simplification to the kernel can be made. It should be pointed out however than assumption on the space invariance can not be made. On a toroidal surface a field can not be invariant because, for example, it is possible to track changes in the position from the local surface curvature. In other words the coils or the sensors on the inner part of the toroidal surface are intrinsically different from the one on the outer surface. But apart of this effect, which could be advocated to be somewhat small for large aspect ratios, there still is the fact that the passive structures are not uniform. They present clear dishomogeneities both in the poloidal direction, such as the shell inner equatorial gap, and in the toroidal direction, such as the shell overlapping region, not to mention the load assembly diagnostic ports. This is a real source of invariance of the space coordinates.

The time invariance allows to reduce the dimension of the kernel domain so that it becomes $h(\boldsymbol{\alpha}, \boldsymbol{\xi}, \tau)$[6]. Making use of the bold notation for n-tuples, the linear transformation becomes

$$b_r(\boldsymbol{\alpha}, u) = \int_U h(\boldsymbol{\alpha}, \boldsymbol{\xi}, u - t) i(\boldsymbol{\xi}, t) d\boldsymbol{\xi} dt. \tag{2.32}$$

Another form of this equation can be obtained by writing explicitly the Haar integrals on the domains. The resulting form is basically the one that could be obtained considering the system, instead of a single linear transformation between multidimensional domains, as a a number of linear transformations from $\mathbb{R}$ to V. Considering that two of the three components of the domain U are lattices, that is $U = U_L \times \mathbb{R}$ with $U_L = \frac{\mathbb{Z}(2\pi/N_1)}{\mathbb{Z}(2\pi)} \times \frac{\mathbb{Z}(2\pi/N_2)}{\mathbb{Z}(2\pi)}$, the linear transformation can be written explicitly as

$$b_r(\boldsymbol{\alpha}, u) = \frac{4\pi^2}{N_1 N_2} \sum_{\boldsymbol{\xi} \in U_L} \int_{\mathbb{R}} h(\boldsymbol{\alpha}, \boldsymbol{\xi}, u - t) i(\boldsymbol{\xi}, t) dt. \tag{2.33}$$

The factor $\frac{4\pi^2}{N_1 N_2}$ can be absorbed in the kernel obtaining the representation

$$b_r(\boldsymbol{\alpha}, u) = \sum_{\boldsymbol{\xi} \in U_L} \int_{\mathbb{R}} \hat{h}_{\boldsymbol{\xi}}(\boldsymbol{\alpha}, u - t) i_{\boldsymbol{\xi}}(t) dt, \tag{2.34}$$

which is perhaps more common and generally accepted. The couple $\boldsymbol{\xi}$ can be seen as a "label" or an index for the elements which it applies to. The leading factor which appears in the above equation depends on the definition of the Haar integral on a lattices as the summation of the signal values times the lattice determinant.

A good estimate of the functions $\hat{h}_{\boldsymbol{\xi}}(\boldsymbol{\alpha}, \tau)$ can be calculated numerically using a time-harmonic solver of eddy currents problems. From the knowledge of the frequency response of these distributions it is possible, in principle, to construct a state space model of harmonics produced by the active coils currents outside the sampling cell. That is of the saddle coils sidebands.

2.4.5 Field sampling

The measure of the radial magnetic field is performed by a set of $N_1 \times N_2$ sensors laid down on a toroidal surface denoted with T_s. The sensors are wide coils, in the sense that their size is not negligible compared to the dimension of the machine itself. The inner radius of T_s is $r_s = 0.507$ m. The number

$$a_s = \frac{r_s}{R_0} \tag{2.35}$$

is a characteristic parameter of the sampling filter and is the inverse of the aspect radius of the toroidal surface T_s.

[6] Actually the new form of the kernel function is denoted with the same symbol of the old form. The compact representation $\hat{h}$ is defined as $\hat{h}(\boldsymbol{\alpha}, \boldsymbol{\xi}, t) = h(\boldsymbol{\alpha}, t, \boldsymbol{\xi}, 0)$. The functions are of course structurally different, but as they are different representations of the same transformation and there is no risk of confusion, the same symbol has been used.

As in the case of the current distribution, the radial magnetic field b_r is represented as a signal on the regular group V. Again, the poloidal and toroidal coordinates which are usually denoted with the letters ϑ and φ, are respectively referred to, in this context, with α_1 and α_2.

The shape of the radial field b_r is influenced by currents in the active coils, Eddy currents in the passive structures and by the dynamics of the plasma. For this reason the radial field distribution is measured in real-time. This measure is carried out by the set of sensor described before. Despite the apparently high number of sensors which can be installed in the machine in order to take this measure, it must be noted that performing the Fourier analysis on the sampled signal is not the same as performing it on the original signal. It has also to be noted that, in fact, the original signal is almost never accessible and all the Fourier analysis has to rely on the sampled signal.

Being the radial field measured by wide sensors, the type of sampling they perform is peculiar and can be formalised with a sampling filter. The radial flux linked to a region of the toroidal surface T_s divided by the value of the region area, gives the mean value of the radial field on that region and using the toroidal coordinates it can be expressed as

$$< b_r > (\boldsymbol{\gamma}) = \frac{1}{A(\boldsymbol{\gamma})} \iint\limits_{C(\boldsymbol{\gamma})} b_r(\boldsymbol{\alpha}) r_s R_0 (1 + a_s \cos(\alpha_1)) d\boldsymbol{\alpha}. \tag{2.36}$$

The region $C(\boldsymbol{\gamma})$ is a rectangle with size $2\pi/N_1 \times 2\pi/N_2$ and center at $\boldsymbol{\gamma}$ in the toroidal coordinate space. This region is mapped into the part of T_s associated with the measure of the flux. Interestingly, this area is almost a cell of $\mathbb{R}^2$ modulo $\mathbb{Z}(2\pi/N_1 \times 2\pi/N_2$. Its area, $A(\boldsymbol{\gamma})$, can be analytically calculated and turns out to be

$$A(\boldsymbol{\gamma}) = \frac{4\pi^2}{N_1 N_2} r_s R_0 \left(1 + b \cos(\gamma_1)\right). \tag{2.37}$$

The parameter b is

$$b = a_s \operatorname{sinc}(1/N_1). \tag{2.38}$$

Introducing the functions

$$\Delta(\boldsymbol{\gamma}, \boldsymbol{\alpha}) = \operatorname{rect}\left(\frac{\alpha_1 - \gamma_1}{2\pi/N_1}\right) \operatorname{rect}\left(\frac{\alpha_2 - \gamma_2}{2\pi/N_2}\right) \tag{2.39}$$

and

$$e(\gamma_1, \alpha_1) = \frac{1 + a_s \cos(\alpha_1)}{1 + b \cos(\gamma_1)} \tag{2.40}$$

the integral (2.36) can be written as a convolution with the following transformation kernel.

$$g(\boldsymbol{\gamma}, \boldsymbol{\alpha}) = \frac{N_1 N_2}{4\pi^2} e(\gamma_1, \alpha_1) \Delta(\boldsymbol{\gamma}, \boldsymbol{\alpha}). \tag{2.41}$$

The purpose of the function $\Delta(\boldsymbol{\gamma}, \boldsymbol{\alpha})$ is to extend the integration to the whole domain V_L without changing the integral. This function is the characteristic function of the region $C(\boldsymbol{\gamma})$. The function $e(\gamma_1, \alpha_1)$ takes into account the value of the infinitesimal area element in the change of coordinates and the value of the area of the sensor. Then the expression for the mean magnetic field at the point $\boldsymbol{\gamma}$ becomes

$$< b_r > (\boldsymbol{\gamma}) = \iint_{V_L} g(\boldsymbol{\gamma}, \boldsymbol{\alpha}) b_r(\boldsymbol{\alpha}) d\boldsymbol{\alpha}. \tag{2.42}$$

The sampling component of this filter ca be established by allowing the evaluation of its output only for variables belonging to the regular group U_L. This is straightforward because $U_L \subset V_L$, and the overall sampling filter turns out to be a sampled version of continuous filter. Considering the variable $\boldsymbol{\zeta} \in U_L$ the sampling filter is

$$< b_r > (\boldsymbol{\zeta}) = \iint_{V_L} g(\boldsymbol{\zeta}, \boldsymbol{\alpha}) b_r(\boldsymbol{\alpha}) d\boldsymbol{\alpha}. \tag{2.43}$$

The filter in the space domain

The filter (2.42) has some peculiarities worth an explanation. The most important is that the filter is not invariant. This is essentially due to the factor $e(\gamma_1, \alpha_1)$ which is expression of the fact that the system is toroidal. In the space domain, an invariant filter would be constant on the affine spaces $\gamma_1 - \alpha_1 = \tau$. Figure 2.4, showing the function $e(\gamma_1, \alpha_1)$ on $[0, 2\pi)^2$, clearly demonstrates that this is not the case. The output value of the filter can also be interpreted as the integral of the radial field on the sensor region weighted by the $e(\gamma_1, \alpha_1)$ and scaled by the factor $\frac{N_1 N_2}{4\pi^2}$. In the case of invariant filters the shape of the weight function would be the same over all the toroidal surface. Instead, Figure 2.5 shows that for different values of the γ_1 variable the shape of the weighting function is different. The source of non-invariance is in the poloidal dimension of the filter. This can be shown using the fact that the filter is separable, and that the factor depending on (γ_2, α_2) is invariant.

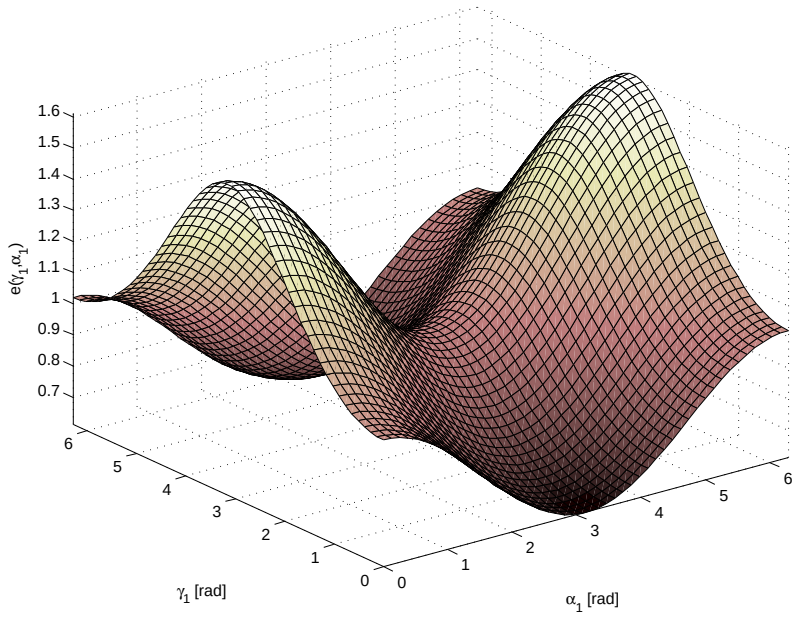

Figure 2.4: Representation of e as function of γ_1 and α_1.

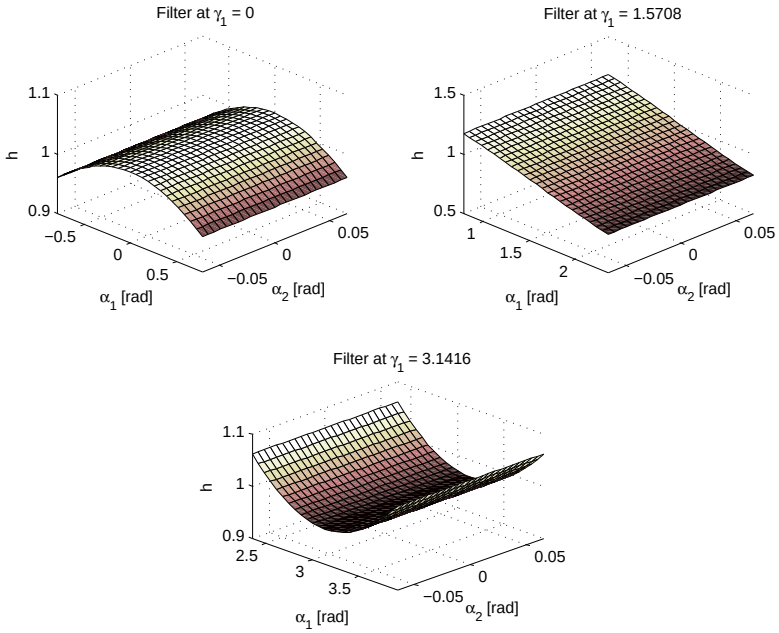

Figure 2.5: Representation of e as function of α_1 and α_2 for $\gamma_1 = 0$, $\gamma_1 = \pi/2$, and $\gamma_1 = \pi$.

The filter in the dual domain

Its Fourier transform is defined over the fourth-dimensional space $\hat{I}^2$

$$G(\boldsymbol{f},\boldsymbol{\nu}) = \iint\limits_{I^2\times I^2} g(\boldsymbol{\gamma},\boldsymbol{\alpha}) e^{-j2\pi(\boldsymbol{f}\cdot\boldsymbol{\gamma}+\boldsymbol{\nu}\cdot\boldsymbol{\alpha})} d\boldsymbol{\gamma} d\boldsymbol{\alpha} \tag{2.44}$$

in general form, but this expression can be simplified considering that the function Δ depends only on the quantity $\boldsymbol{\tau} = \boldsymbol{\alpha} - \boldsymbol{\gamma}$ that is

$$\Delta(\boldsymbol{\gamma},\boldsymbol{\alpha}) = \text{rect}\left(\frac{\alpha_1-\gamma_1}{2\pi/N_1}\right)\text{rect}\left(\frac{\alpha_2-\gamma_2}{2\pi/N_2}\right) \tag{2.45}$$

$$\tilde{\Delta}(\gamma_1,\alpha_1,\tau_2) = \text{rect}\left(\frac{\alpha_1-\gamma_1}{2\pi/N_1}\right)\text{rect}\left(\frac{\tau_2}{2\pi/N_2}\right) \tag{2.46}$$

and that the function e depends only on γ_1 and α_1 and thus can be written like $e(\boldsymbol{\gamma},\boldsymbol{\alpha}) = \tilde{e}(\gamma_1,\alpha_1)$. Substituting in the above equation $\boldsymbol{\gamma}$ in favour of $\boldsymbol{\tau}$, the integrand can be factored out as a product of 2 functions of different variables.

$$g(\gamma_1,\gamma_2,\alpha_1,\alpha_2) = g_1(\gamma_1,\alpha_1)g_2(\gamma_2,\alpha_2) \tag{2.47}$$

In the above equation, g_1 and g_2 are expressed by the following equations.

$$g_1(\gamma_1,\alpha_1) = \frac{N_1}{2\pi}\tilde{e}(\gamma_1,\alpha_1)\text{rect}\left(\frac{\alpha_1-\gamma_1}{2\pi/N_1}\right) \tag{2.48}$$

$$g_2(\gamma_2,\alpha_2) = \frac{N_2}{2\pi}\text{rect}\left(\frac{\alpha_2-\gamma_2}{2\pi/N_2}\right) \tag{2.49}$$

By means of this factorization the problem of calculating the four dimensional Fourier transform of $g(\gamma_1,\gamma_2,\alpha_1,\alpha_2)$ can be simplified and transformed into the easier job of finding two two-dimensional Fourier transforms. In this case, the four-dimensional Fourier transform $G(\boldsymbol{f},\boldsymbol{\nu})$ turns out to be the product of two two-dimensional Fourier transforms.

$$\begin{aligned}
&\iint\limits_{I^2\times I^2} g(\boldsymbol{\gamma},\boldsymbol{\alpha}) e^{-j2\pi(\boldsymbol{f}\cdot\boldsymbol{\gamma}+\boldsymbol{\nu}\cdot\boldsymbol{\alpha})} d\boldsymbol{\gamma} d\boldsymbol{\alpha} = \\
&\iiiint\limits_{I^4} g_1(\gamma_1,\alpha_1)g_2(\gamma_2,\alpha_2) e^{-j2\pi(f_1\gamma_1+\nu_1\alpha_1)} e^{-j2\pi(f_2\gamma_2+\nu_2\alpha_2)} d\gamma_1 d\gamma_2 d\alpha_1 d\alpha_2 = \\
&\iiiint\limits_{I^4} g_1(\gamma_1,\alpha_1) e^{-j2\pi(f_1\gamma_1+\nu_1\alpha_1)} g_2(\gamma_2,\alpha_2) e^{-j2\pi(f_2\gamma_2+\nu_2\alpha_2)} d\gamma_2 d\alpha_2 d\gamma_1 d\alpha_1 = \\
&\iint\limits_{I^2} g_1(\gamma_1,\alpha_1) e^{-j2\pi(f_1\gamma_1+\nu_1\alpha_1)} d\gamma_1 d\alpha_1 \iint\limits_{I^2} g_2(\gamma_2,\alpha_2) e^{-j2\pi(f_2\gamma_2+\nu_2\alpha_2)} d\gamma_2 d\alpha_2 \\
&\qquad = G_1(f_1,\nu_1)G_2(f_2,\nu_2)
\end{aligned}$$

the integration of g_2 is straightforward making the change of variable $\alpha_2 = \tau_2 + \gamma_2$.

$$\begin{aligned}
G_2(f_2,\nu_2) &= \iint\limits_{I^2} g_2(\gamma_2,\alpha_2)e^{-j2\pi(f_2\gamma_2+\nu_2\alpha_2)}d\gamma_2 d\alpha_2 \\
&= \frac{N_2}{2\pi}\iint\limits_{I^2} \operatorname{rect}\left(\frac{\tau_2}{2\pi/N_2}\right)e^{-j2\pi(f_2\gamma_2+\nu_2\tau_2+\nu_2\gamma_2)}d\gamma_2 d\tau_2 \\
&= \frac{N_2}{2\pi}\iint\limits_{I^2} \operatorname{rect}\left(\frac{\tau_2}{2\pi/N_2}\right)e^{-j2\pi\nu_2\tau_2}e^{-j2\pi(f_2+\nu_2)\gamma_2}d\gamma_2 d\tau_2 \\
&= \frac{N_2}{2\pi}\int\limits_{I} \operatorname{rect}\left(\frac{\tau_2}{2\pi/N_2}\right)e^{-j2\pi\nu_2\tau_2}\int\limits_{I} e^{-j2\pi(f_2+\nu_2)\gamma_2}d\gamma_2 d\tau_2 \\
&= \delta_{\hat{I}}(f_2+\nu_2)\frac{N_2}{2\pi}\int\limits_{I} \operatorname{rect}\left(\frac{\tau_2}{2\pi/N_2}\right)e^{-j2\pi\nu_2\tau_2}d\tau_2 \\
&= \delta_{\hat{I}}(f_2+\nu_2)\operatorname{sinc}\left(\frac{2\pi}{N_2}\nu_2\right)
\end{aligned}$$

The integration of g_1 is a little bit more difficult but fortunately it can also be carried out in two steps,

$$\begin{aligned}
G_1(f_1,\nu_1) &= \iint\limits_{I^2} g_1(\gamma_1,\alpha_1)e^{-j2\pi(f_1\gamma_1+\nu_1\alpha_1)}d\gamma_1 d\alpha_1 \\
&= \frac{N_1}{2\pi}\iint\limits_{I^2} \frac{1+a\cos(\alpha_1)}{1+a\frac{\sin(\pi/N_1)}{\pi/N_1}\cos(\gamma_1)}\cdot \\
&\qquad \cdot \operatorname{rect}\left(\frac{\alpha_1-\gamma_1}{2\pi/N_2}\right)e^{-j2\pi(f_1\gamma_1+\nu_1\alpha_1)}d\gamma_1 d\alpha_1 \\
&= \frac{N_1}{2\pi}\int\limits_{I} \frac{e^{-j2\pi f_1\gamma_1}}{1+a\frac{\sin(\pi/N_1)}{\pi/N_1}\cos(\gamma_1)}\cdot \\
&\qquad \cdot \int\limits_{I} (1+a\cos(\alpha_1))\operatorname{rect}\left(\frac{\alpha_1-\gamma_1}{2\pi/N_2}\right)e^{-j2\pi\nu_1\alpha_1}d\alpha_1 d\gamma_1
\end{aligned}$$

considering that

$$\mathcal{F}[e^{j\alpha t}](f) = \int\limits_{I} e^{j\alpha t}e^{-j2\pi ft}dt = \delta_{\hat{I}}\left(f-\frac{\alpha}{2\pi}\right) \tag{2.50}$$

and that the Fourier transform of the product of two signals is equal to the convolution of the respective Fourier transforms the integral

$$H(\nu_1,\gamma_1)=\int_I [1+a\cos(\alpha_1)]\,\mathrm{rect}\left(\frac{\alpha_1-\gamma_1}{2\pi/N_1}\right)e^{-j2\pi\nu_1\alpha_1}d\alpha_1 \tag{2.51}$$

turns out to be the convolution of the following two signals

$$H_1(\nu_1)=\int_I [1+a\cos(\alpha_1)]\,e^{-j2\pi\nu_1\alpha_1}d\alpha_1 = \\ =\delta_{\hat{I}}(\nu_1)+\frac{a}{2}\delta_{\hat{I}}\left(\nu_1-\tfrac{1}{2\pi}\right)+\frac{a}{2}\delta_{\hat{I}}\left(\nu_1+\tfrac{1}{2\pi}\right) \tag{2.52}$$

$$H_2(\nu_1,\gamma_1)=\int_I \mathrm{rect}\left(\frac{\alpha_1-\gamma_1}{2\pi/N_1}\right)e^{-j2\pi\nu_1\alpha_1}d\alpha_1 = \\ =\frac{2\pi}{N_1}e^{-j2\pi\nu_1\gamma_1}\,\mathrm{sinc}\left(\tfrac{2\pi}{N_1}\nu_1\right) \tag{2.53}$$

that is

$$H(\nu_1,\gamma_1)=\int_{\hat{I}} F_2(\tau,\gamma_1)F_1(\nu_1-\tau)d\tau = \\ =\frac{2\pi}{N_1}e^{-j2\pi\nu_1\gamma_1}\left\{\mathrm{sinc}\left(\tfrac{2\pi}{N_1}\nu_1\right)+\frac{a}{2}e^{j\gamma_1}\,\mathrm{sinc}\left[\tfrac{2\pi}{N_1}\left(\nu_1-\tfrac{1}{2\pi}\right)\right]+ \right. \\ \left. +\frac{a}{2}e^{-j\gamma_1}\,\mathrm{sinc}\left[\tfrac{2\pi}{N_1}\left(\nu_1+\tfrac{1}{2\pi}\right)\right]\right\} \tag{2.54}$$

At this point the function $G_1(f_1,\nu_1)$ has become

$$G_1(f_1,\nu_1)=\frac{N_1}{2\pi}\int_I \frac{e^{-j2\pi f_1\gamma_1}}{1+b\cos(\gamma_1)}H(\nu_1,\gamma_1)d\gamma_1 \tag{2.55}$$

but, despite it is possible, in principle, to solve analytically the integral, the calculations needed in order to get the closed form formula in the parameters b and f_1 (remembering that $2\pi f_1\in\mathbb{Z}$) require an attention which is not worth the effort, especially considering the scope of the work. For this reason it has been chosen to write the filter in terms of the function $P(f_1)$, defined as below and computing numerically the rest of the calculation.

$$\boxed{P(f_1)=\int_I \frac{e^{-j2\pi f_1\gamma_1}}{1+b\cos(\gamma_1)}d\gamma_1} \tag{2.56}$$

With this convention the $G_1(f_1, \nu_1)$ component of the filter becomes

$$\begin{aligned} G_1(f_1,\nu_1) = \operatorname{sinc}\left(\tfrac{2\pi}{N_1}\nu_1\right) P(f_1+\nu_1) + \\ + \frac{a}{2}\operatorname{sinc}\left(\tfrac{2\pi}{N_1}(\nu_1-\tfrac{1}{2\pi})\right) P(f_1+\nu_1-\tfrac{1}{2\pi}) + \\ + \frac{a}{2}\operatorname{sinc}\left(\tfrac{2\pi}{N_1}(\nu_1+\tfrac{1}{2\pi})\right) P(f_1+\nu_1+\tfrac{1}{2\pi}) \end{aligned} \quad (2.57)$$

and the Fourier transform of the filter turns out to be

$$\begin{aligned} G(\boldsymbol{f},\boldsymbol{\nu}) &= G_2(f_2,\nu_2)G_1(f_1,\nu_1) = \\ &= \delta_{\hat{f}}(f_2+\nu_2)\operatorname{sinc}\left(\tfrac{2\pi}{N_2}f_2\right)\Big\{\operatorname{sinc}\left(\tfrac{2\pi}{N_1}\nu_1\right) P(f_1+\nu_1) + \\ &\quad + \frac{a}{2}\operatorname{sinc}\left(\tfrac{2\pi}{N_1}(\nu_1-\tfrac{1}{2\pi})\right) P(f_1+\nu_1-\tfrac{1}{2\pi}) + \\ &\quad + \frac{a}{2}\operatorname{sinc}\left(\tfrac{2\pi}{N_1}(\nu_1+\tfrac{1}{2\pi})\right) P(f_1+\nu_1+\tfrac{1}{2\pi})\Big\} \end{aligned} \quad (2.58)$$

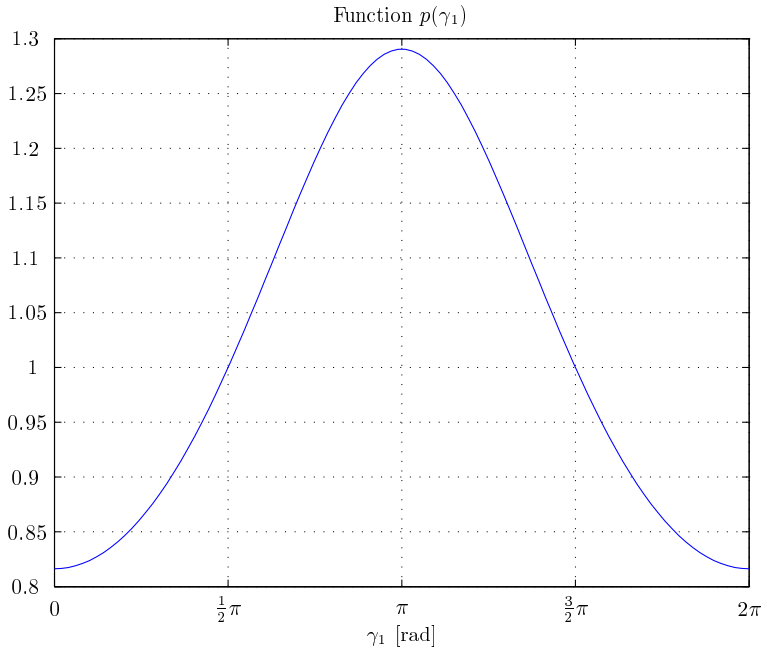

Figure 2.6: The function $p(\gamma_1)$.

$p(\gamma_1)$, the function of which $P(f_1)$ is the Fourier transform, is presented in figure 2.6. By the figure it can be expected that $p(\gamma_1)$ has a mean value

around 1 and the first harmonic about 0.2 times the mean. In fact, the function $P(f_1)$, which has been obtained by numerically evaluating the integral expression (2.56) at a number of chosen values of the f_1 parameter, confirms the expectations.

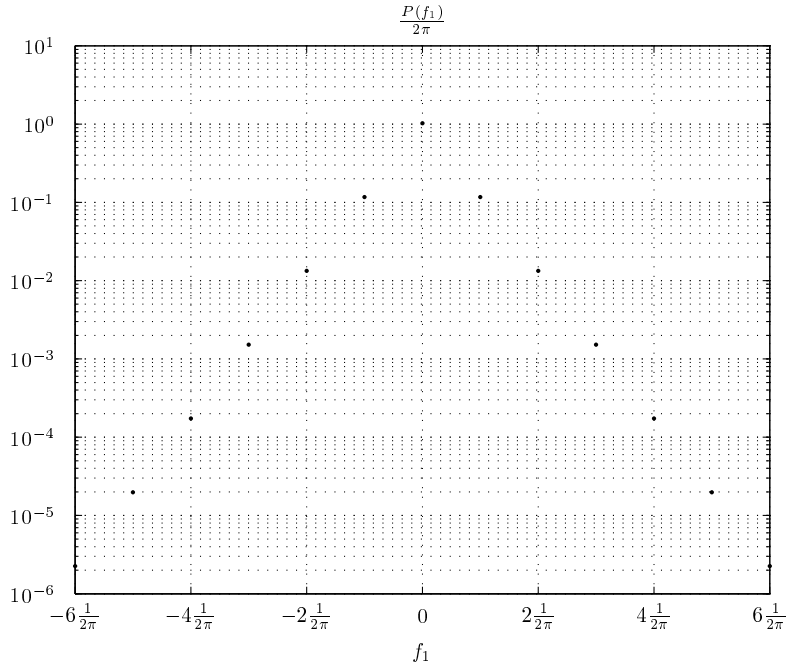

Figure 2.7: Representation of the function $|P(f_1)|$ in logarithmic scale.

In figure 2.7 is presented the absolute value of $P(f_1)$ divided by the factor 2π in logarithmic scale. It is worth noticing that the value of the complex Fourier coefficients is exponentially decaying as in a geometric series with ratio, roughly speaking, 1/10. This means that the space-variance of $G(\boldsymbol{f}, \boldsymbol{\nu})$) can be well approximated considering only the first or the second harmonics in f_1, ν_1.

As R_0 tends toward infinity the parameter a tends to zero. Moreover the function $P(f_1)$ tends to $\delta_{\hat{I}}(f_1)$ which lead to the expected expression for the harmonic content of the filter

$$G(\boldsymbol{f}, \boldsymbol{\nu}) = \delta_{\hat{I}}(f_1 + \nu_1)\delta_{\hat{I}}(f_2 + \nu_2)\,\mathrm{sinc}\left(\frac{2\pi}{N_1} f_1\right)\mathrm{sinc}\left(\frac{2\pi}{N_2} f_2\right) \tag{2.59}$$

Analytical model	Studied model
Is space invariant	Is space variant
Makes a brutal approximation of the kernel (bi-dimensional rect)	Considers the actual flux density
Permits analytical calculations	Requires numerical evaluation of the kernel

Table 2.4: Differences between the analytical model used for the development of the sideband correction algorithm and the features of the system as studied in the framework of the Unified Theory.

The parameter Λ

Considering the result of proposition 2.3 the parameter Λ defined as follows

$$\Lambda = \sqrt{\frac{\int_{\hat{V}_L} \delta_{\hat{V}_L}(\boldsymbol{f}+\boldsymbol{\nu})|G(\boldsymbol{f},\boldsymbol{\nu})|^2 d\boldsymbol{\nu}}{\int_{\hat{V}_L} |G(\boldsymbol{f},\boldsymbol{\nu})|^2 d\boldsymbol{\nu}}}, \tag{2.60}$$

gives a measure of the degree of variance of a filter g on V_L. This parameter is always a number between zero and one on the domain $\hat{V}_L$ because the haar integral is a summation. It is the square root of the ratio between the energy of the filter along the invariant subspace and the total energy of the filter.

2.5 Conclusions

The fact that the sampling performed by the radial field coils is space-variant has some consequences on the signal reconstruction. Indeed the harmonic content of the input signal is distorted not only by a function multiplication, but by an integral linear transformation. This implies that the exponential functions are not filter eigenfunctions as happens in the invariant case. It is worth spending some time comparing the features of this signal based model with those of the common cylindrical model used in the analytical development of the sideband correction algorithm.

This chapter shows that the Unified Signal Theory can be applied to give a detailed description of the behaviour of the MHD system and how to use its results to perform analyses of its components. This chapter shows that the real MHD system presents more than one structural differences from the standard cylindrical model usually used for the derivation of analytical formulas.

However, it does not provide a critique to the development of such a models, which often can be used to implement algorithms allowing an excellent performance of the machine. It provide a method which can be considered when the assumption made by more simple models become unacceptable. The result of this analysis is the detailed explanation, from the point of view of the Unified Signal Theory, of the relation between the physical quantities involved in the analytical models and the actual information that is available for the real-time control. The existence of this step should not be forgotten. The major difference between a uniform cylindrical model and the model proposed in this chapter is the space variance. A weak source of space variance is the toroidal geometry. This has an effect both on the radial field and current sampling. Much stronger source of spatial variance are the shell features such as gaps and ports. The actual harmonic content of the field distribution generated by the saddle coil currents can be estimated with a better accuracy performing numerical calculations using a Finite Element Model of the RFX-mode machine and an electromagnetic solver such as CARIDDI, for example. This result can have an impact on the algorithm which compensates for the aliasing induced by the radial field sampling.

Chapter 3

Model

3.1 Introduction

Summarising what said in the first chapter, the RFX-mod active system for the control of the MHD instabilities consists of 192 active saddle coils, mounted so as to completely cover the outer toroidal surface of the stainless steel supporting structure [4]. The radial component of the magnetic field is measured by an equal number of saddle probes, located on the projection of the active coils on the outer surface of the vessel. The shell is characterised by a poloidal gap and an inner equatorial gap to allow the penetration of the toroidal component of the electric and magnetic field respectively.

A highly flexible real time control system was implemented, capable of performing bi-dimensional spatial Fourier analysis of the field components producing the corresponding harmonics characterized by the poloidal (m) and toroidal (n) mode numbers [8]. Several control strategies were envisaged and have been operating for one year with very good results in terms of quality of the magnetic boundary, bringing about a doubling of energy confinement time in pulses over 300 ms long [9]. The two main strategies are the "virtual shell" and the "mode control". In the basic version of the former, the radial component of the magnetic field measured by each sensor is cancelled, in the latter, selected modes (RWM's or tearing modes) of one field component can be either suppressed or actively stimulated. Up to now simple controllers equal for all the coils have been used; a prospective exploitation of the system flexibility asks for the design of a more sophisticated controller capable of an independent action on either selected modes or different coils taking into account the toroidal geometry, the effect of the passive structures and other local features.

To this purpose a full electromagnetic dynamic model of the active control system has been developed taking advantage of the experience gained on the

other European RFP experiment T2R [10]. The model inputs are the voltages applied to each coil and its outputs the magnetic fluxes measured by the saddle probes. Consistently with previous work in this field, it is also suited to the integration with a dynamic model of the plasma RWM's [11]. The development of such a requires the knowledge of the self and mutual coupling terms between active coils and their resistance. The control scheme which uses the information provided by the radial field sensors requires the knowledge of the mutual couplings between active coils and sensors. The presence of passive conductors such as the vacuum chamber, the shell and the supporting structure, either the coupling and the dissipative factor depend on the frequency.

A preliminary campaign of measures allowed the acquisition of the data for the calculation of the equivalent resistances and of the self and mutual couplings of the active coils [12]. The values obtained have been arranged in two three-dimensional matrices in order to save the information about the frequency response. During the campaign C3, dedicated to the commissioning of the system, a series of vacuum shots has been performed to characterise the open-loop frequency response of the system made up of the power amplifiers the active coils and the sensors. A set of poloidal array has been selected as representative of the different responses of the system due to the local features of the machine. During these experiments coils of different poloidal arrays have been fed at the same time in order to minimise the length of the campaign. The poloidal arrays have been selected trying to minimise cross effects on the sensors measurements, which would have lead to the wrong evaluation of the couplings coefficients. Step and sinusoidal currents at different frequencies have been impressed into the coils acting as inputs of the system. The data have then been collected and analysed automating a procedure already used on T2R data. As previously made for the active coils data, a 3D matrix of complex coefficients has been constructed representing the amplitude and phase of the couplings between active coils and sensors for each test frequency. For their relative position, the couplings between the active coils and the sensors come to depend more on the frequency than those of the active coils. Some validation tests evidenced that while constant matrices allowed to reproduce with sufficient accuracy the current dynamics, that was not possible for the radial fluxes at the sensors. Taking advantage of a MATLAB® identification routine already used in the past with satisfying results [13], a matrix of rational function approximating the dynamic response of the MHD system has been obtained. For computational convenience, the transfer function matrix representation of the system has been changed to an equivalent state space model with constant matrices.

The dynamic system is necessary for the simulation of the overall system

both in open and closed loop operations. It has also been useful in the optimisation of the performance of the regulators present in the various control loops foreseen in RFX-mod, such as the "virtual shell" and mode control.

3.2 Active Circuits Matrices

Since the coupling and dissipative terms depend on the frequency, in principle complex calculation of transfer functions and convolution products would be necessary to obtain the coil current response to whatever voltage input. Alternatively, in order to maintain a state-variable model, particularly suitable to the analysis and design of a control system, the state vector should be extended adding to the coil currents further states to account for the currents circulating in the passive conductors. When the circuit parameter variation is not large, a simplified approach, already adopted in [11], can be tried. It consists in assuming a representation where the states are only the coil currents, the inputs are the corresponding power-supply voltages, and the inductance ($\mathbf{L}$) and resistance ($\mathbf{R}$) matrices are constant element matrices made up of values averaged over the range of measure or taken at a particular frequency. In this case $-\mathbf{L}^{-1}\mathbf{R}$ and $\mathbf{L}^{-1}$ are the state matrix and the "input-state" matrix, respectively. Later on it will be shown that in our case this approach entails an acceptable error in reproducing the current dynamics. In the following the currents are numbered from 1 to 192 using the progressive notation. The inductance and resistance matrix have been built accordingly. In the pictures, however, the bi-dimensional notation has been followed as it seemed more immediate. The experimental data were provided as normalized ratios $\bar{V}_i/\bar{I}_i$ and $\bar{V}_k/\bar{I}_i$. They were obtained by feeding some selected groups of coils with a controlled current at the frequency of 10, 20, 50, 100, 200 Hz. More precisely, the groups were above the shell overlapped gap zone (toroidal index: 13, 14, 15, 16, 17, 18, 19), above a shell "standard" zone (toroidal index 26, 35), on the zone of the support structure second poloidal gap (toroidal index 39, 40, 41). Defining $\dot{Z}_{ii}(\omega)$ as

$$\dot{Z}_{ii}(\omega) = Z_{ii}(\omega)e^{j\varphi_{Z_{ii}}(\omega)} = \bar{V}_i(\omega)/\bar{I}_i(\omega), \tag{3.1}$$

the quantity $\dot{Z}^*_{ii}(\omega) = \dot{Z}_{ii}(\omega)/(\omega N^2)$ (magnitude and phase) was provided, where N is the number of turns of each active coil (N=60). Assuming

$$\dot{Z}_{ii}(\omega) = R_{ii,eq}(\omega) + j\omega L_{ii,eq}(\omega), \tag{3.2}$$

the equivalent resistance $R_{ii,eq}(\omega)$, including the losses in the passive conductors, and self-inductance $L_{ii,eq}(\omega)$ were calculated as a function of frequency

usign the following formulas

$$R_{ii,eq}(\omega) = \omega N^2 Z^*_{ii}(\omega)\cos(\varphi_{Z^*_{ii}}(\omega)) \tag{3.3}$$

$$L_{ii,eq}(\omega) = N^2 Z^*_{ii}(\omega)\sin(\varphi_{Z^*_{ii}}(\omega)). \tag{3.4}$$

In some cases (for instance validation of FE model results) a decomposition which clearly separates pure resistive and inductive terms can be more useful. Such a decomposition can be derived introducing a complex inductance $\dot{L}_{ii}(\omega) = L_{ii}(\omega)e^{j\varphi_{L_{ii}}(\omega)} = \bar{\Psi}_i(\omega)/\bar{I}_i(\omega)$, whose aim is to account for the delay and attenuation of the resulting magnetic flux and the additional losses due to the currents induced in the passive structures. $\dot{L}_{ii}(\omega)$ can be calculated from its defining equation

$$\dot{Z}_{ii}(\omega) = R_{ii}(\omega) + j\omega\dot{L}_{ii}(\omega). \tag{3.5}$$

Here $R_{ii}(\omega)$ is the actual resistance of the i-th coil at the given frequency. If the skin effect in the coil is neglected, the equation

$$\dot{Z}_{ii}(\omega) = R_{ii} + j\omega\dot{L}_{ii}(\omega) \tag{3.6}$$

is assumed, where $R_{ii} = R_{ii}(\omega)|_{\omega=0}$. The amplitude of $\dot{L}_{ii}(\omega)$ can then be expressed as

$$L_{ii}(\omega) = \frac{\sqrt{R^2_{ii}(\omega) + Z^2_{ii}(\omega) - 2R_{ii}(\omega)Z_{ii}(\omega)\cos(\varphi_{Z_{ii}}(\omega))}}{\omega}, \tag{3.7}$$

and its phase $\varphi_{L_{ii}}(\omega)$ as:

$$\varphi_{L_{ii}}(\omega) = \operatorname{atan2}\left(R_{ii}(\omega) - Z_{ii}(\omega)\cos(\varphi_{Z_{ii}}(\omega)), Z_{ii}(\omega)\sin(\varphi_{Z_{ii}}(\omega))\right). \tag{3.8}$$

Now consider the case when the i-th coil is fed and the k-th coil voltage is measured:

$$\dot{Z}_{ki}(\omega) = \bar{V}_k(\omega)/\bar{I}_i(\omega). \tag{3.9}$$

Again, the quantity $\dot{Z}^*_{ki}(\omega) = \dot{Z}_{ki}(\omega)/(\omega N^2)$ being available[1], we calculate:

$$R_{ki,eq}(\omega) = \omega N^2 Z^*_{ki}(\omega)\cos(\varphi_{Z^*_{ki}}(\omega)) \tag{3.10}$$

$$L_{ki,eq}(\omega) = N^2 Z^*_{ki}(\omega)\sin(\varphi_{Z^*_{ki}}(\omega)). \tag{3.11}$$

In this case the trans-impedance $\dot{Z}_{ki}(\omega)$ is directly linked to the complex mutual inductance itself according to the equation $\dot{Z}_{ki}(\omega) = j\omega\dot{L}_{ki}(\omega)$, all the dissipative effects in the passive conductors related to the k-th coil current being taken into account.

[1]The actual available angle was $\alpha_{ki} = \varphi_{Z^*_{ki}}(\omega) + \pi/2$, thus the equations implemented in the code are $R_{ki,eq}(\omega) = \omega N^2 Z^*_{ki}(\omega)\sin(\alpha_{ki}(\omega))$ and $L_{ki,eq}(\omega) = N^2 Z^*_{ki}(\omega)\cos(\alpha_{ki}(\omega))$.

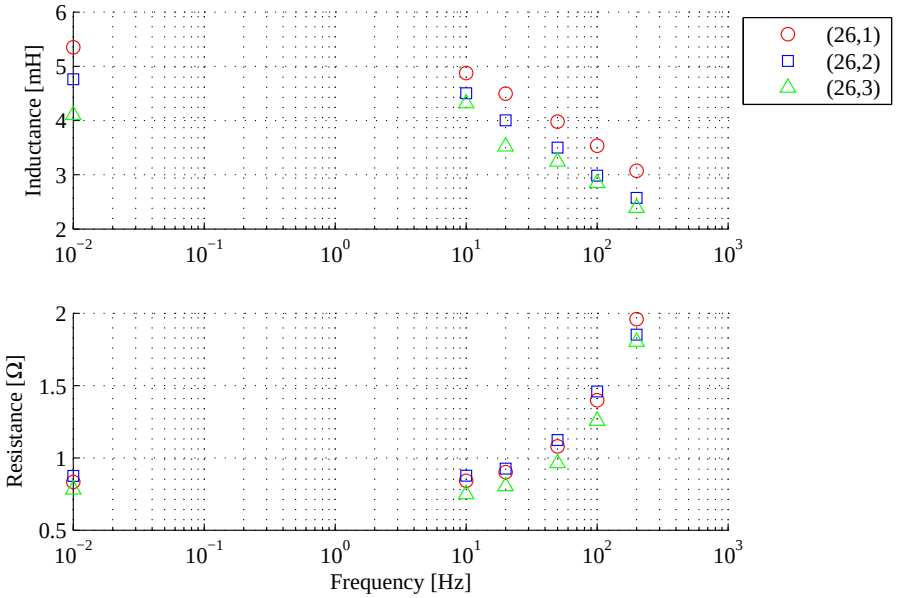

Figure 3.1: Self inductance and resistance of the saddle coils in the legend.

In Figure 3.1 the equivalent self-inductance and resistance are presented as a function of frequency for the three kinds of coil (outer = 1, top and bottom = 2, inner = 3) in a "typical" poloidal section (number 26 at = 187.5°), that is far away from the machine poloidal gaps. The values of self and mutual inductances at 0.01 Hz have been obtained by previous FEM analyses. Circuit resistances as seen from each power supply were derived by taking the averages, at steady state, of the corresponding ratio voltage/current in two vacuum shots where a m=1, n=0 mode was generated with phase=0 (shot 17133) and phase=$\pi/2$ (shot 17718), respectively. Besides the self-inductance reduction due to the increasing shielding effect of the passive structures as long as frequency increases, it is worth while noticing the differences due to the toroidal geometry.

In Figure 3.2, referring again to the array 26, the self inductance of the upper coil and its couplings with the poloidally and toroidally adjacent ones are compared, as a function of frequency. The "off-diagonal" dissipative terms are also presented in the figure. These are associated only to the passive structures, which react to the currents induced in the surrounding active coils, as well. The coupling terms are singled out by a couple of numbers, where the digits 0 e ± 1 mean invariance and increment/decrement along the toroidal (first digit of the couple) and poloidal (second digit of the couple) direction. The relative

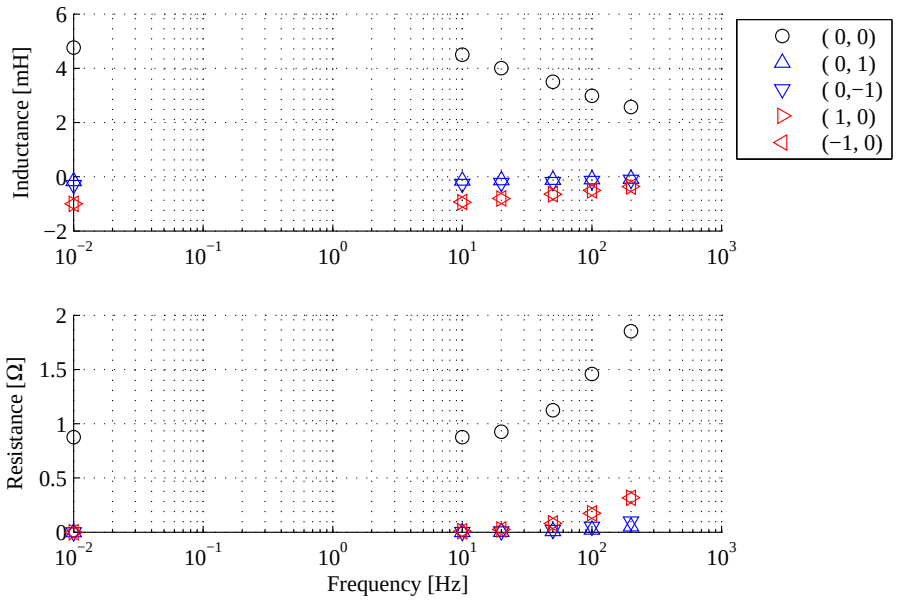

Figure 3.2: Mutual inductance and resistance between coil (26,2) and adjacent coils.

weight of self and mutual inductance is apparent and, in particular, the greater importance of the coupling with the toroidally adjacent coils, consistently with the longer length of the poloidal leg, can be appreciated.

In the considered frequency range the maximum variation of self and mutual inductances with respect to their averages are about 26% and 31%, respectively. Moreover, mutual inductances are less than 18% of the corresponding self inductance. In the next section it will be shown how the simulation results are affected by using average values of the coupling parameters. Eventually, in Figure 3.3, an example of self-inductance variation along the toroidal direction is provided. It was chosen to compare some outer coils, affected by both the poloidal and the equatorial gap, the latter being short-circuited in a nearly uniform way only as far as the copper shell is concerned. The self-inductance value is also influenced by the possible presence of pumping or diagnostics ports. The coils belong to the array 14, 16, 26 and 40, whose positions have been given at the beginning of this section; it should also be remarked that coil (14, 1) encircles a pumping port. An interpretation of the observed result is the prevailing effect of the copper shell, characterized by a higher conductivity, at lower frequencies. In fact the lowest self-inductance values belong to coils whose projection lies onto shell zone where the short-circuit elements

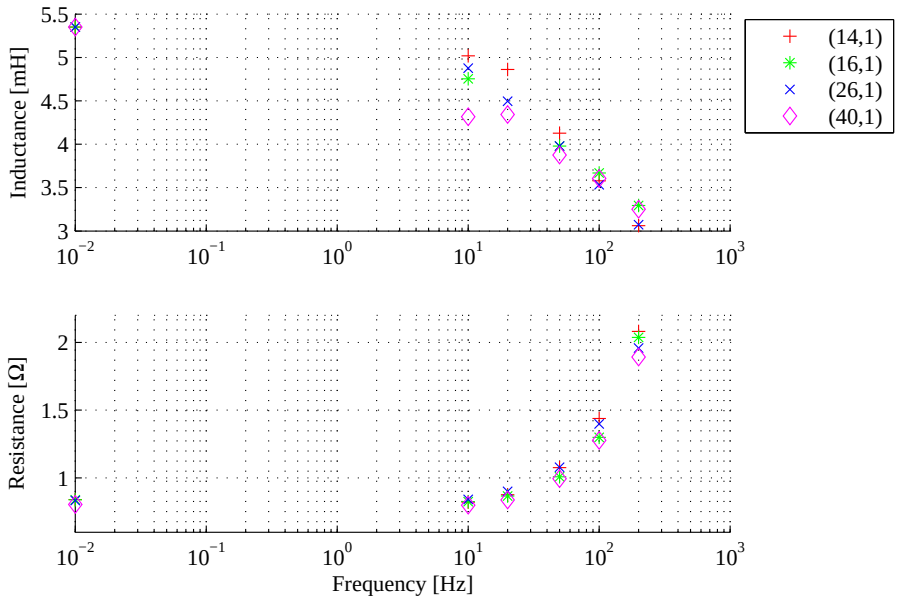

Figure 3.3: Self inductance and resistance of the coils in the external array.

number is higher, even though they span a cut of the supporting structure. Actually, the different toroidal pitch of the saddle coils and the short-circuit system bring about different "overlapping patterns" between coils and short-circuiting elements. Where the number of short-circuiting elements is higher, the better is the shell "equatorial continuity" approximated.

On the contrary, as the frequency increases, the outer conductor, i.e. the supporting structure, becomes also an effective shield, except in the cut stretches, where the maximum values of coil self-inductances can then be found. An example of this behaviour can be seen in the figure, at low frequency, where the coil with maximum inductance is (14,1), which surrounds a pumping port coming before the shell underlying edge without any short-circuiting elements, and the coil with minimum inductance is (40,1), mounted onto the intersection of the structure poloidal and toroidal cuts, but where three shell short-circuiting elements are present. The self-inductance of this latter coil results less attenuated at high frequencies.

3.2.1 Experimental validation

In order to validate the coupling terms and to assess the achievable accuracy in using constant element matrices some tests have been carried out. In Figure

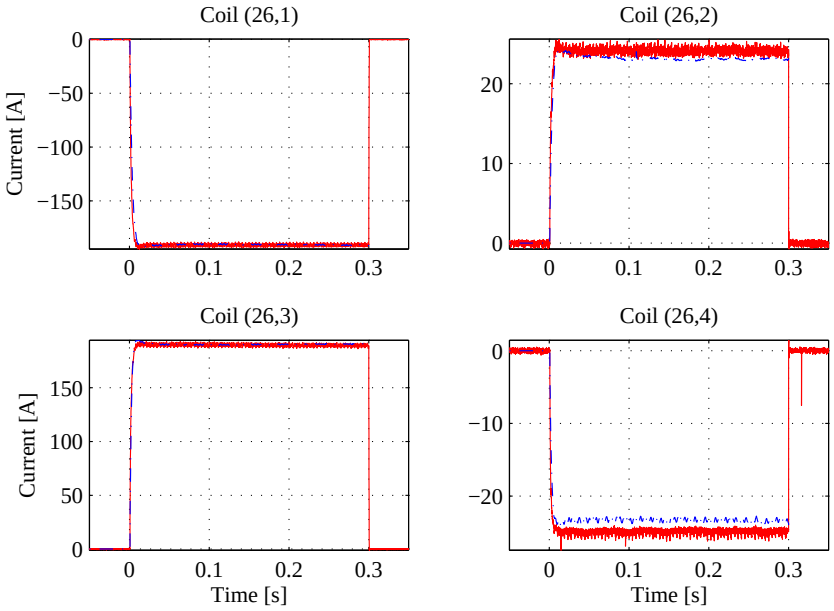

Figure 3.4: Comparison between actual currents (red) and model currents (blue) in shot number 17131.

3.4 and Figure 3.5 experimental and model coil currents are compared. The experimental voltages are applied as model inputs. In the former (shot 17131) a m = 1, n = 1 mode was generated in a vacuum shot; in the latter (shot 17523) a m = 1, n = -7, 10 Hz rotating field was given as a reference in a plasma shot with virtual shell. The 0 Hz and 10 Hz values of inductance and resistance were used to make up the matrices, respectively. The agreement is very satisfactory in both cases even in the transient phase. In particular, the second example also shows that it is an acceptable assumption to neglect the coupling between plasma and active coil currents, the former not appearing to affect the evolution of the latter significantly.

3.3 Matrix of mutual inductances between active coils and sensors

An approach similar to that described in the previous section was followed in the evaluation of the matrix of the mutual inductances between active coils and sensors. The same “typical” parts of the load assembly were considered: “standard” zone, structure and shell poloidal gap with shell overlapped edges, only

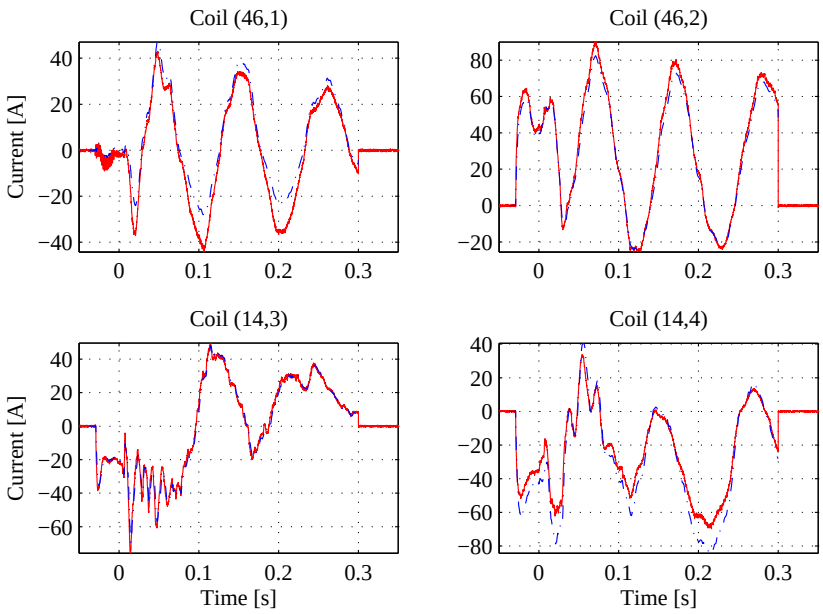

Figure 3.5: Comparison between actual currents (red) and model currents (blue) in shot number 17523.

structure poloidal gap. As a further sample of the first zone, data collected in a section at φ=22.5° have been included. Unlike the experimental data used in the previous section, these were collected during a campaign specifically dedicated to the system commissioning and thus they have been acquired and stored as regular RFX data, which makes them much more conveniently accessible.

3.3.1 Evaluation of the 3D matrix elements

As aforementioned in the introduction, the evaluation was carried out improving and speeding up a procedure already used in processing T2R data, i.e. analysing the signals available at the different frequencies by means of Fourier and Hilbert transforms. The results are substantially coincident except for the highest frequencies, where, possibly due to a lower signal to noise ratio, results provided by DFT seemed to be more reliable, in particular as far as the phase estimate is concerned. For all the four poloidal positions the coupling with 12 sensors has been considered, namely the underlying one and the surrounding eight, the previous one and the following one along the toroidal direction and the opposite, i.e. at 180° along the poloidal direction. This high number was

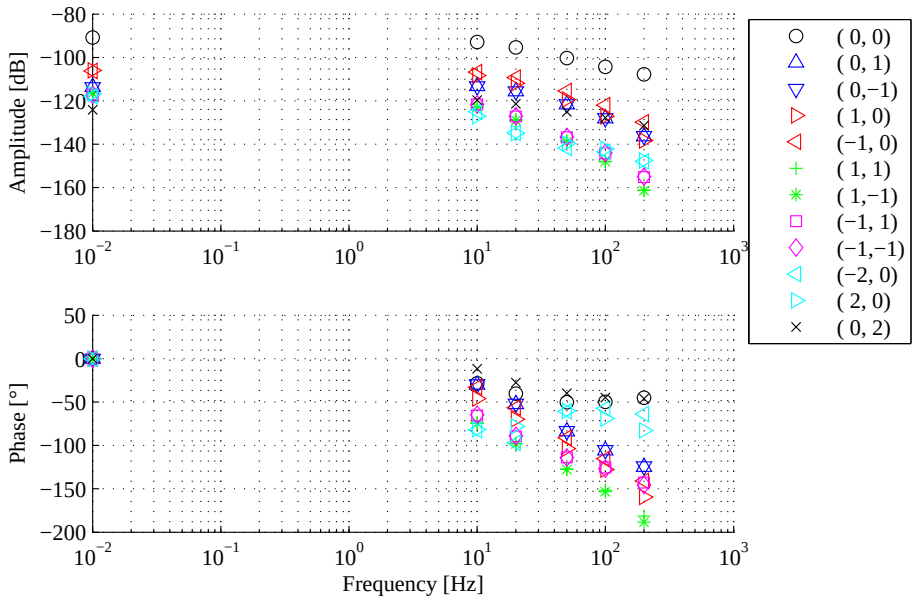

Figure 3.6: Mutual coupling between coil (16,1) and nearby sensors.

reached after some iterations, necessary to achieve a satisfactory agreement between the measured and the calculated radial component of the magnetic field, imposing the measured coil currents as input signals in the model. The matrix was then filled by inserting the averages of the values obtained in the "standard" zone of the load assembly.

In Figure 3.6 amplitudes and phases of the mutual inductances relative to coil (16,1) are shown as a function of frequency. Again here we use the relative numbering to distinguish the different couplings. The values at 0 Hz depend on the geometry and relative position, consistently with the intuition, but it can be noticed that increasing the frequency, the coupling with the opposite (0,2) and the toroidally not adjacent ($\pm$2,0) sensors becomes more important. This can be explained considering the presence of the shell overlapped edges and the inner equatorial gap. Other non symmetric results, such as the differences between the coupling (-2,0) and (2,0), i.e. with sensor underlying coil (14,1) and (18,1), respectively, are also due to the non-axisymmetric local features of the load assembly. On the contrary, in Figure 3.7 a much more symmetric behaviour is exhibited by the couplings relative to a coil (26,1) in a standard section. The mutual inductances between coil and underlying sensor of the same "standard" section are shown in Figure 3.8. It is interesting to notice that at high frequency the presence of the inner equatorial gap compensates

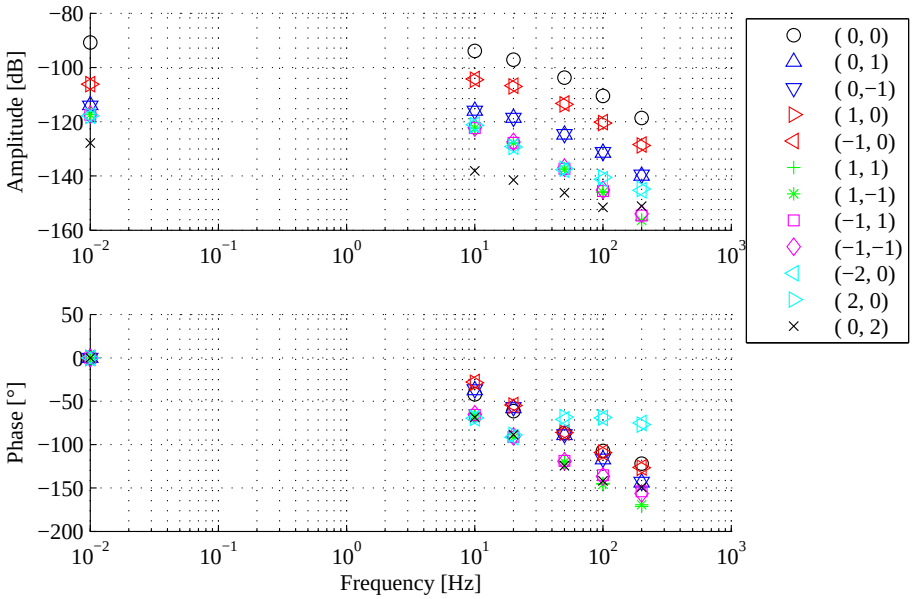

Figure 3.7: Mutual coupling between coil (26,1) and nearby sensors.

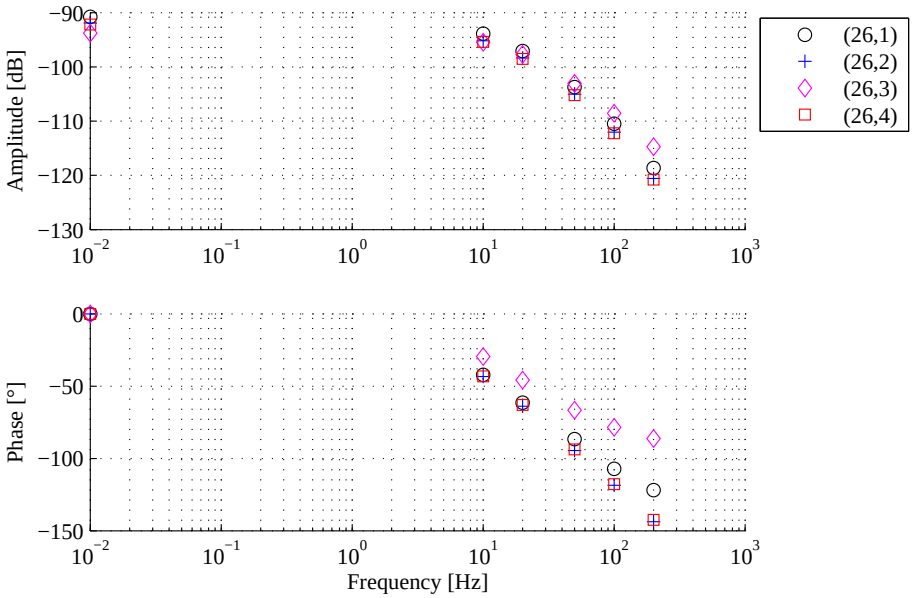

Figure 3.8: Mutual coupling (0,0) of the coils in the poloidal array 26.

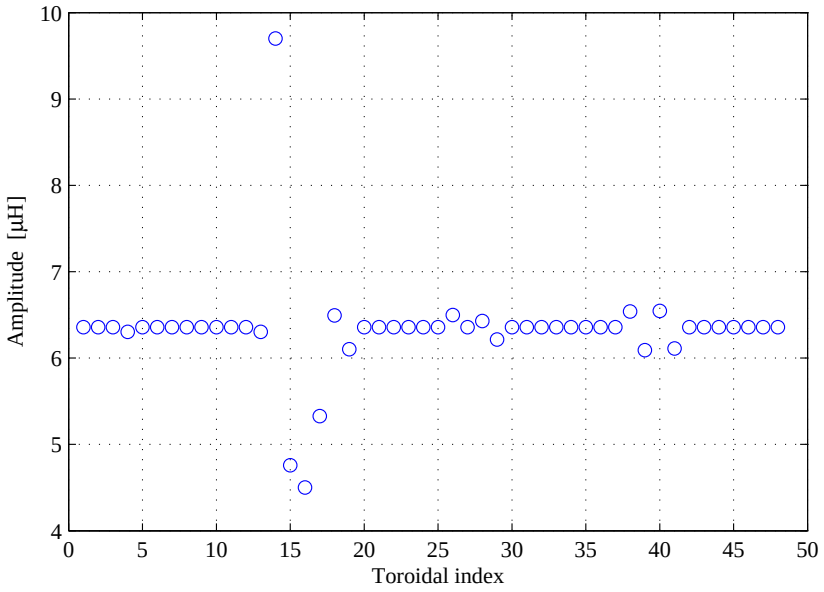

Figure 3.9: Self-inductance of the external coils at 50 [Hz].

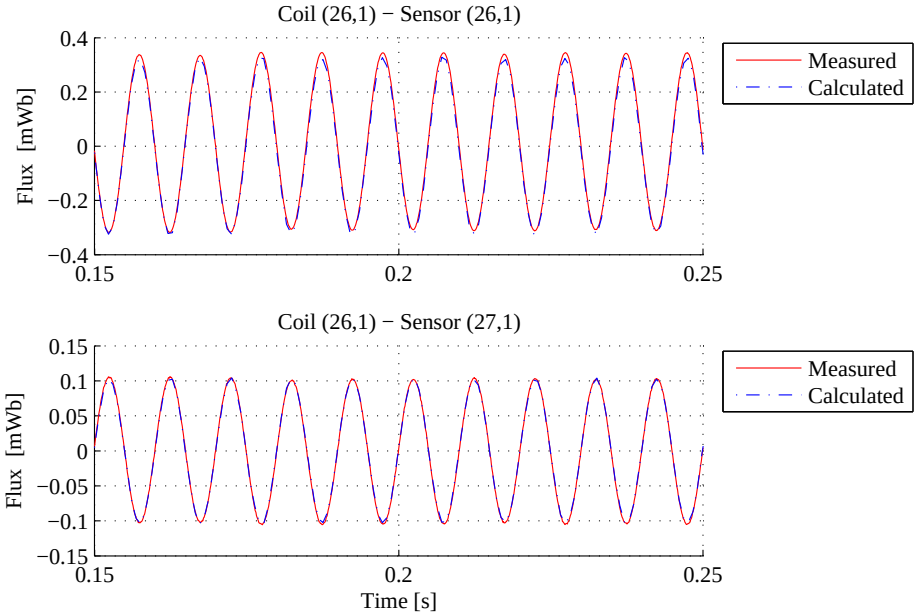

Figure 3.10: Comparison between actual flux and the delayed-scaled source current at 100 [Hz].

for the reduced size of the inner coil-sensor couple, the corresponding mutual inductance resulting larger than the others where the shielding of the passive structures is more effective. A comprehensive view of (0,0)-coupling along the torus at 50 Hz is given in Figure 3.9. Apart from some small numerical variations, the most significant differences are observed nearby the structure and shell poloidal gaps, as expected. In particular, (14,1) is the highest since there is no short-circuit element in the inner shell edge on its right side; on the contrary the following three mutual inductances are the lowest, as the corresponding couples face the shell overlapped edges with the outer one regularly short-circuited. The deviations are lower in the section of the structure second poloidal gap; the largest two terms result (38,1) and (40,1), the former couple encircling a pumping port and the latter spanning the poloidal gap. The average values of the "standard" zone appear at the other positions.

In Figure 3.10, as an example of the accuracy in the mutual inductance evaluation procedure, the measured and reproduced evolution of the magnetic radial component in two positions are presented in a 100 Hz case: a very good agreement can be observed.

3.3.2 Evaluation of the transfer function matrix

In order to build a model suitable to the control system analysis and the regulator design is required a block capable of providing the magnetic field as measured by the sensors in the presence of a general coil current input. Some preliminary tests using different constant term matrices, i.e. the same simplified approach as in the case of the active coil inductance and resistance matrices, clearly demonstrated that this approach was not applicable due to the strong dependence of the coupling terms on the frequency.

Thus a matrix whose elements are transfer functions was necessary. On the other hand, as mentioned in the introduction to section 2, a state variable representation is more convenient and numerically robust. Thus, first a MIMO transfer functions model was built and then a state space realization was worked out. In the past a procedure was developed to obtain the transfer function of the magnetic vertical component produced by the field shaping windings currents inside the old thick conducting shell of RFX. Now it has been upgraded and adapted to the automatic evaluation of the coil-sensor transfer functions. It is based on a MATLAB® toolbox routine providing the numerator and denominator coefficients of the transfer function which best fits in a least square sense an assigned set of experimental frequency response data. By inspection of the first results it was noticed that according to the couple coil-sensor, a different number of zeros and poles of the transfer functions was necessary to achieve the best fitting. Nine mutual inductances were initially

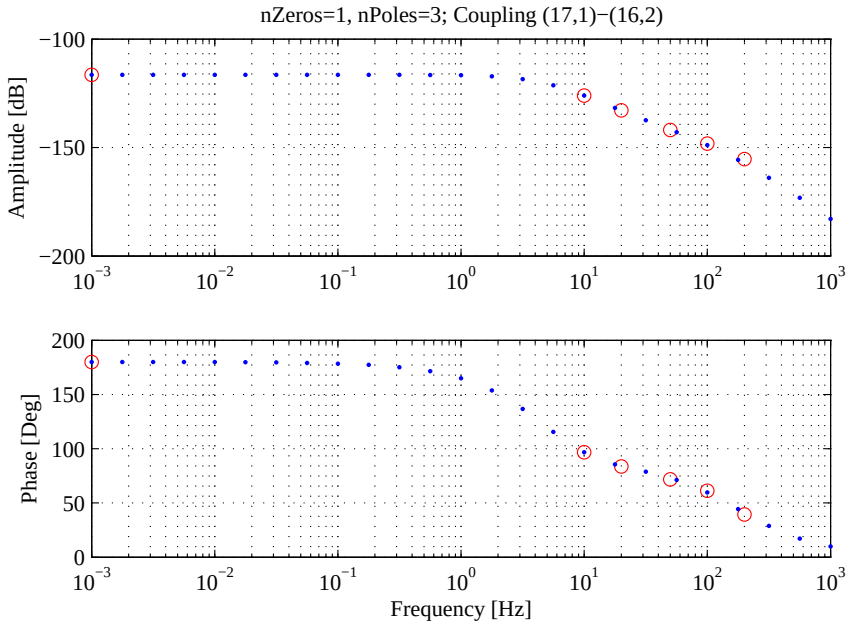

Figure 3.11: Measured (red circles) and estimated (blue dots) frequency response. Cross coupling best case.

considered, that is to say the coupling between each coil, the underlying sensor and the other eight surrounding it. On the basis of the symmetry and the dynamic behaviour they were grouped into 3 classes, each corresponding to a different combination of zeros and poles in the automatic procedure. Instead, it was always imposed on the relative degree, defined as the difference between the degree of the numerator and the denominator polynomials, to be less than zero to obtain a strictly proper system. The output of the numerical routine was then simplified by getting rid of poles and zeros at frequencies larger than 2 KHz, i.e. not significant to fit the data in the experimental range ($\leq$200Hz). This implied to insert a correction factor to maintain the steady-state gain.

A final tuning was also carried out on the relative weights of the fit-errors versus frequency. After the first tests to validate the capability to reproduce the time evolution of the magnetic field it has been necessary to add three further couplings, namely with the two toroidally not adjacent sensors and with the opposite one, but it has been chosen not to modify the tuning again.

In Figure 3.11 and Figure 3.12 the experimental frequency response data are compared with the Bode plots of the calculated transfer functions in the case of the mutual inductance between a coil and an upward right shifted and an underlying sensor, respectively. Both amplitude and phase are correctly

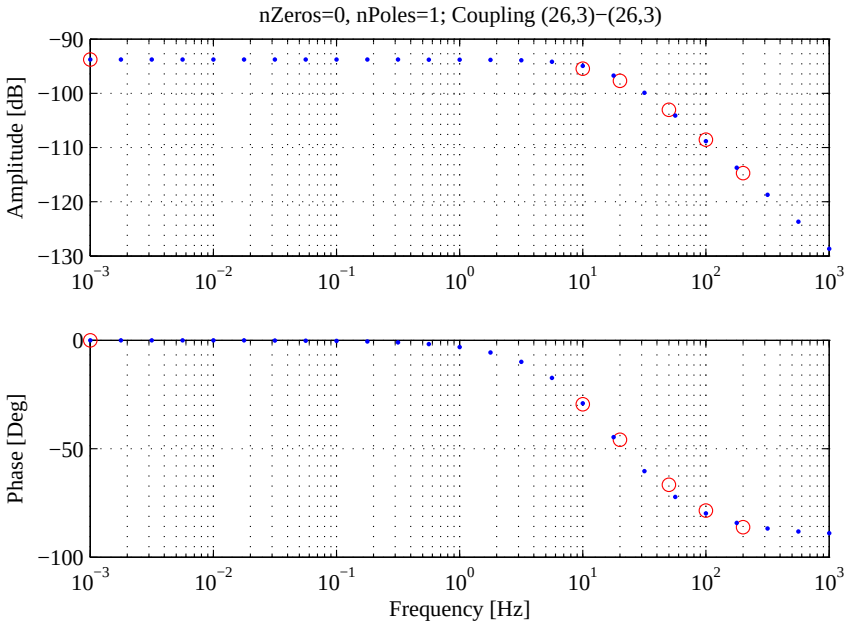

Figure 3.12: Measured (red circles) and estimated (blue dots) frequency response. Coupling with underlying sensor best case.

reproduced. On the whole, a satisfactory agreement was observed, except for few cases, corresponding to particular position along the torus. An example of the worst matching is given in Figure 3.13, where amplitude and phase of the mutual inductance between inner coil and underlying sensor in the region of the shell overlapped edges are shown.

3.3.3 Experimental validation

It was already pointed out the importance of developing a state-space model to perform complex numerical calculation. An automatic procedure which avails of a MATLAB® routine allows to convert the transfer function matrix into a state space model. The high order of the resulting model (5968 states) imposed to provide for a subdivision into a convenient number of subsystems (in this case 6). The validation procedure is similar to that described in section 2.2. Since we were just interested in the mutual inductance block, we applied the measured coil currents as system inputs and derived the radial components of the magnetic field as model outputs. In Figure 3.14 and Figure 3.15 the fluxes measured in shot 17136 by 4 poloidal arrays of saddle probes are compared with the corresponding model outputs. In this shot a m=1, n=2 mode was created

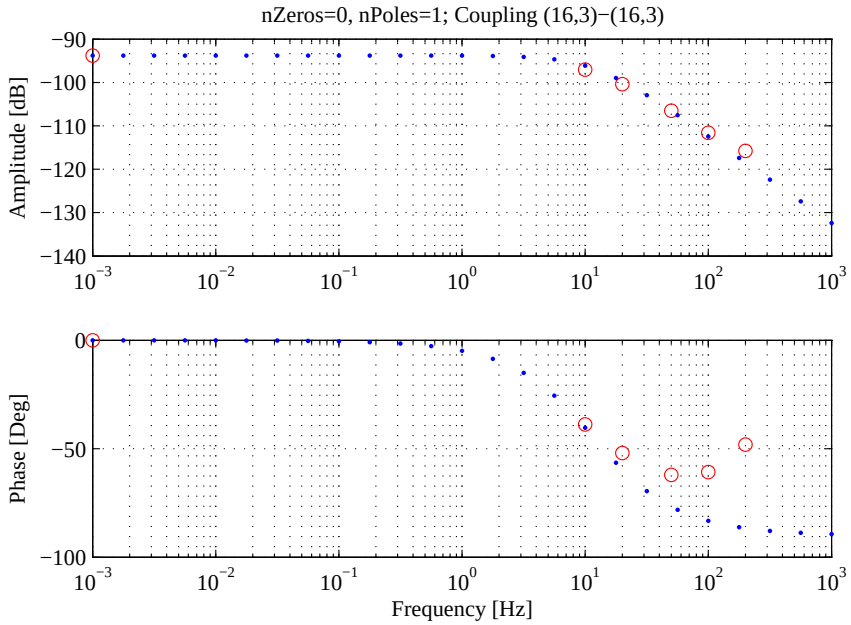

Figure 3.13: Measured (red circles) and estimated (blue dots) frequency response. Worst case.

and the chosen arrays (toroidal number 14, 16, 26 and 40) give a picture of the flux evolution in different sectors of the toroidal load assembly. On the whole a rather satisfactory agreement is achieved; the observed deviations should be attributed to the effect of not included contributions from farther coils.

3.4 Validation of the full open loop model

The further step was to connect the two system V-I and I-F in series obtaining the full open loop model of the system. Data of shot 17131 (generation of a m=1, n=1 mode) have been considered for the same representative set of poloidal arrays. In Figure 3.16 and Figure 3.17 the comparison of experimental and calculated fluxes in the V-F and I-F models is presented. The agreement in the V-F case is still satisfactory, even if some quantities of the full model exhibit a larger deviation from the experimental values. Nonetheless the accuracy was assessed adequate for a sufficiently reliable regulator design and analysis of its performance.

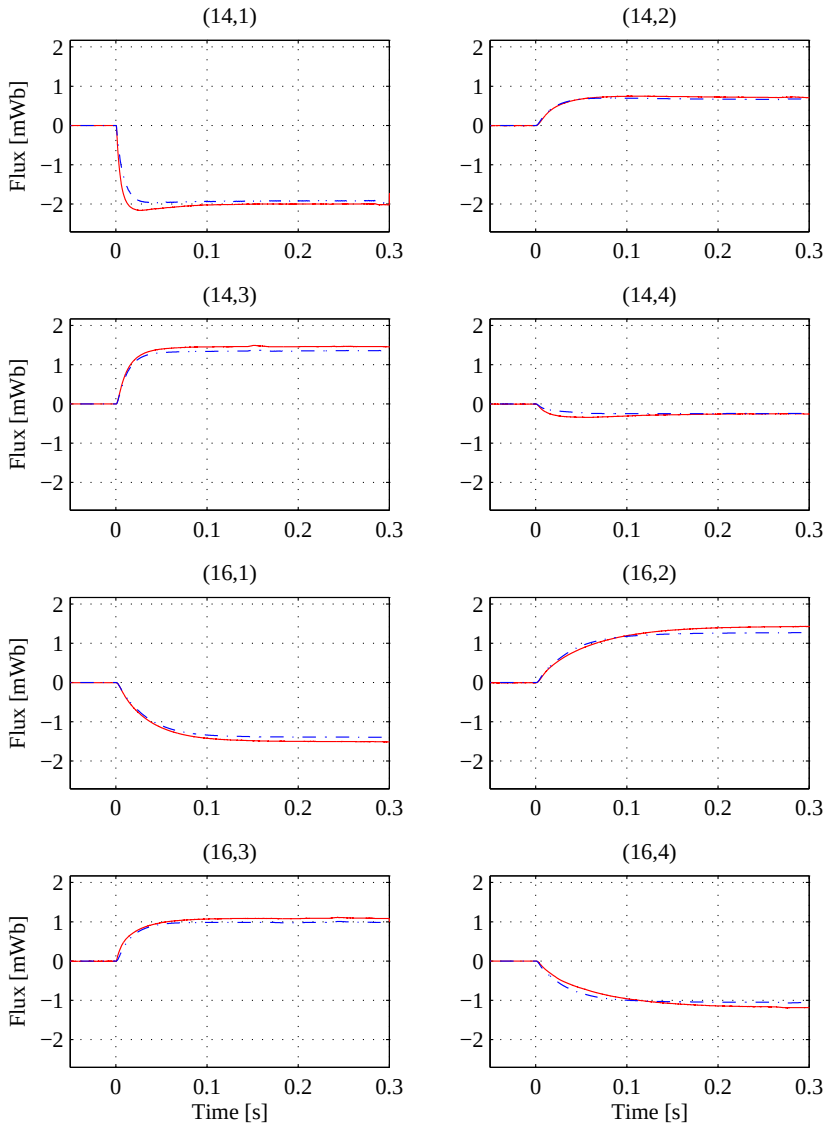

Figure 3.14: Comparison between measured flux (red) and calculated flux (blue) at the specified sensor in shot 17136.

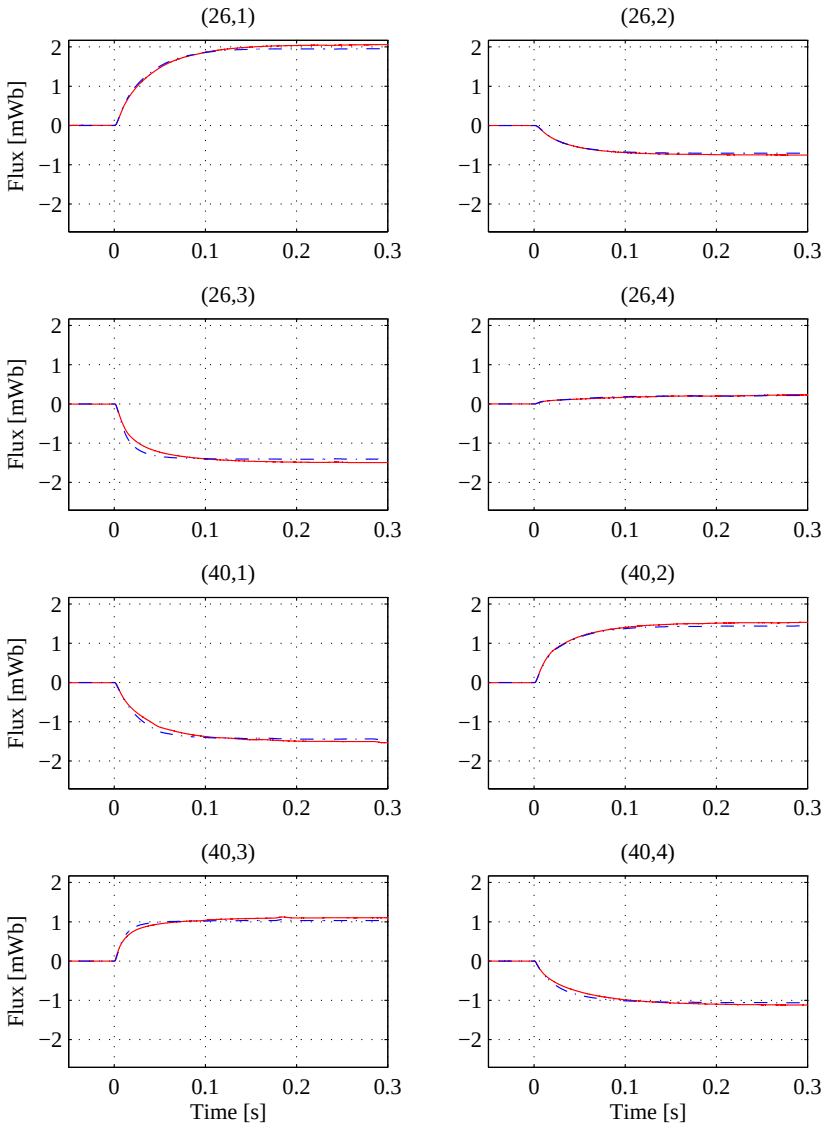

Figure 3.15: Comparison between measured flux (red) and calculated flux (blue) at the specified sensor in shot 17136.

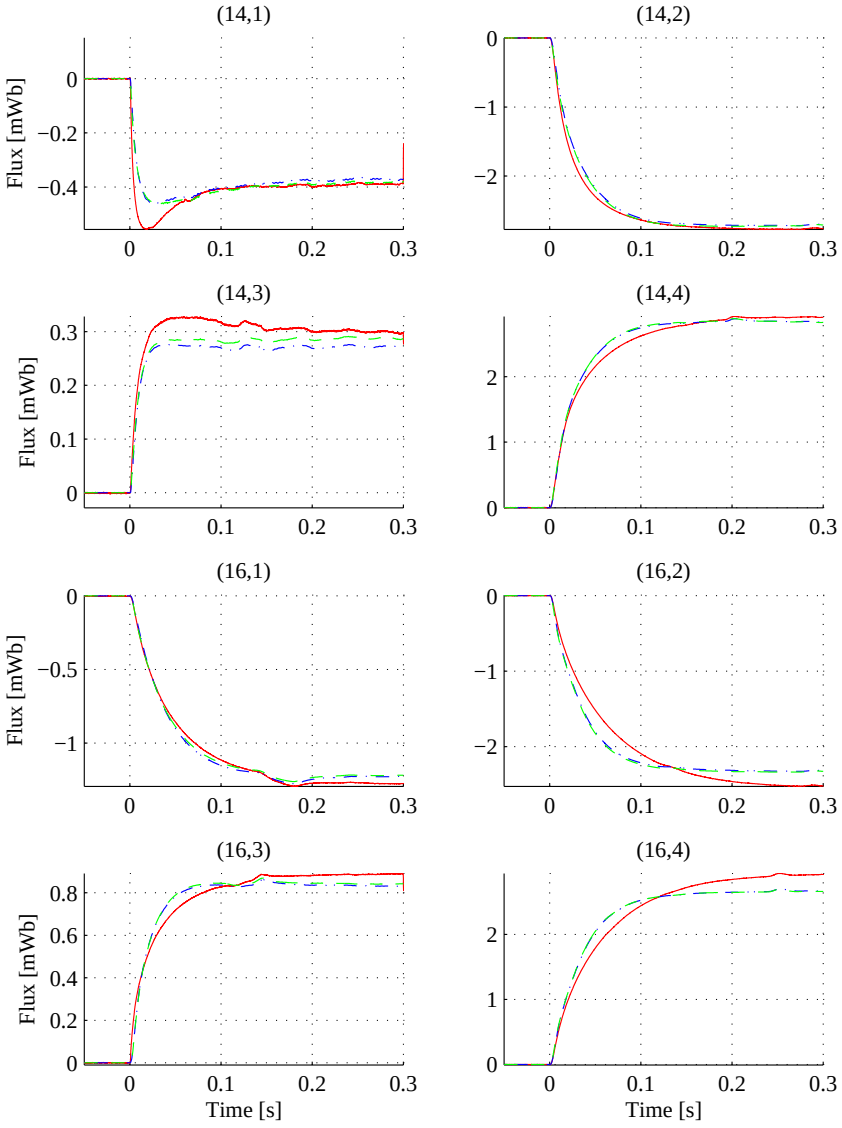

Figure 3.16: Comparison between measured flux (red) and calculated flux using the V-F (blue) and I-F (green) models in shot 17131. Data relative to the poloidal arrays 14 and 16.

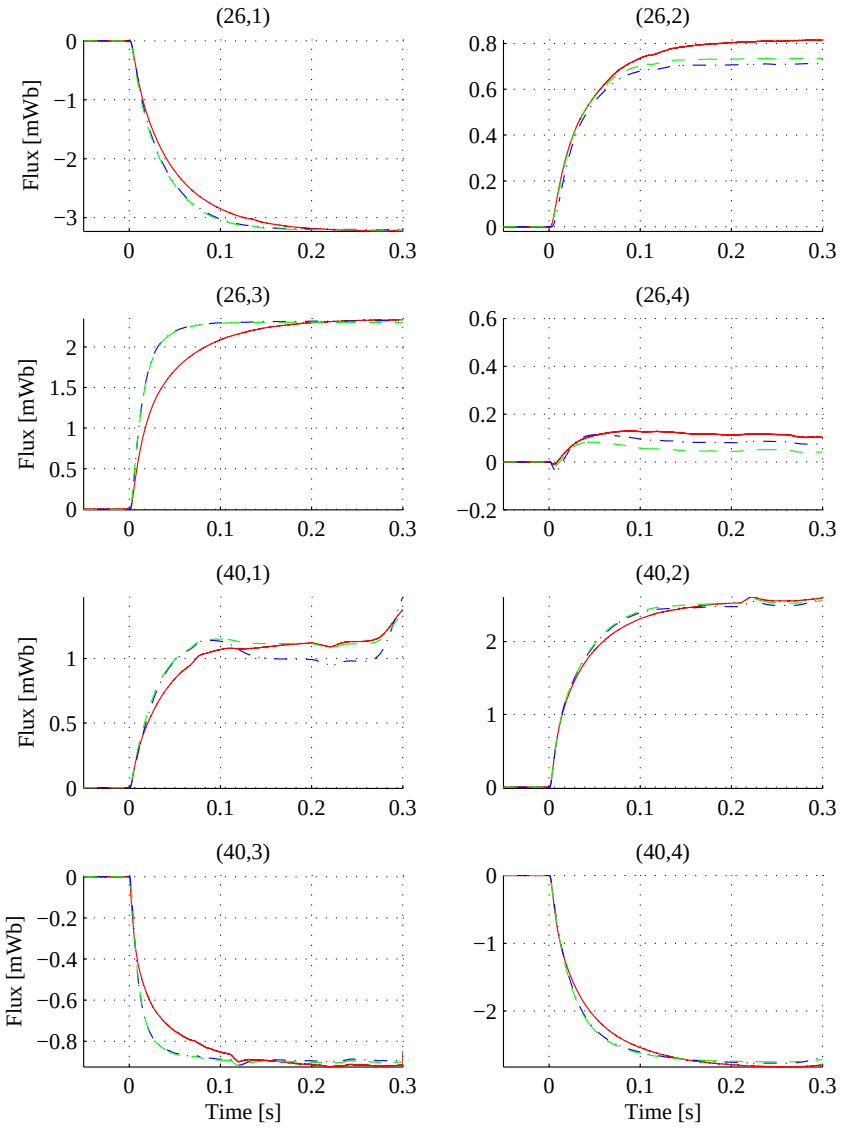

Figure 3.17: Comparison between measured flux (red) and calculated flux using the V-F (blue) and I-F (green) models in shot 17131. Data relative to the poloidal arrays 26 and 40.

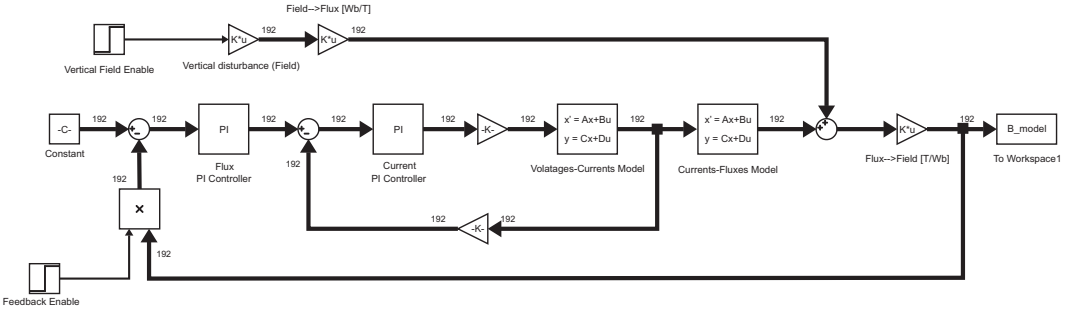

Figure 3.18: Block diagram of the MHD system in closed loop configuration.

3.5 Validation of the closed loop model

The closed loop model is presented in Figure 3.18. The regulator acts on the magnetic field error, so a conversion block from flux to field is included in the loop. The inner current control loop is also represented; the parameters of the PI digital regulator implemented on the power-supply boards have not been changed in the considered experimental sessions and are summarized as follows: sampling time $T_s = 51$ μs, $\hat{k}_P = 1$, $\hat{k}_I = 392$, $\hat{k}_D = 0$. On the contrary, the effect of some variations in the MHD mode controller parameters is presented in the following paragraphs and compared with the model results. As a matter of fact, the real system always performs a space FFT on the 192 magnetic field samples provided by the saddle probes. When the so-called virtual shell operation is chosen, the Fourier components undergo an inverse FFT to obtain again the original signal. Alternatively, in the mode control scheme, selected modes can be ruled out or feedback controlled. Feedforward modal components can also be superimposed. In the presented cases virtual shell operation was chosen and, consequently, it was not considered necessary to include the FFT and FFT^{-1} blocks. Eventually, an enable block was added to take into account the actual insertion instant of the MHD mode control system.

3.5.1 Stability analysis in virtual shell operation

In shots 17166, 17167, 17168 a 2 mT vertical magnetic field was created by the currents of the Field Shaping Winding and three different values of k_I gains were tested to determine the stability margin of the MHD mode control system and to assess its capability to vanish this "disturbance" field. In shot 17166, $k_I = 400 \times 10^3$ was chosen bringing about an unstable response of the system. This same behaviour is correctly reproduced by the model. The integral gain

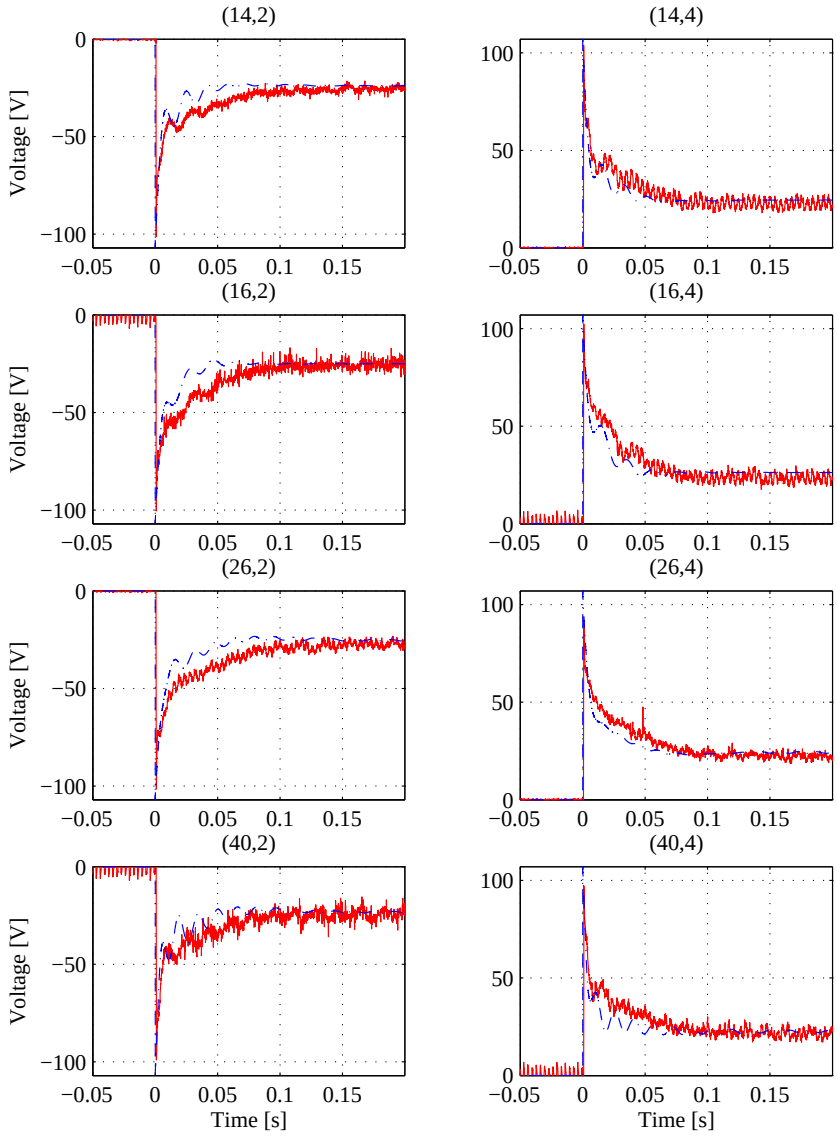

Figure 3.19: Comparison between experimental (red) and simulated voltages (blue) using the closed loop model in shot 17167.

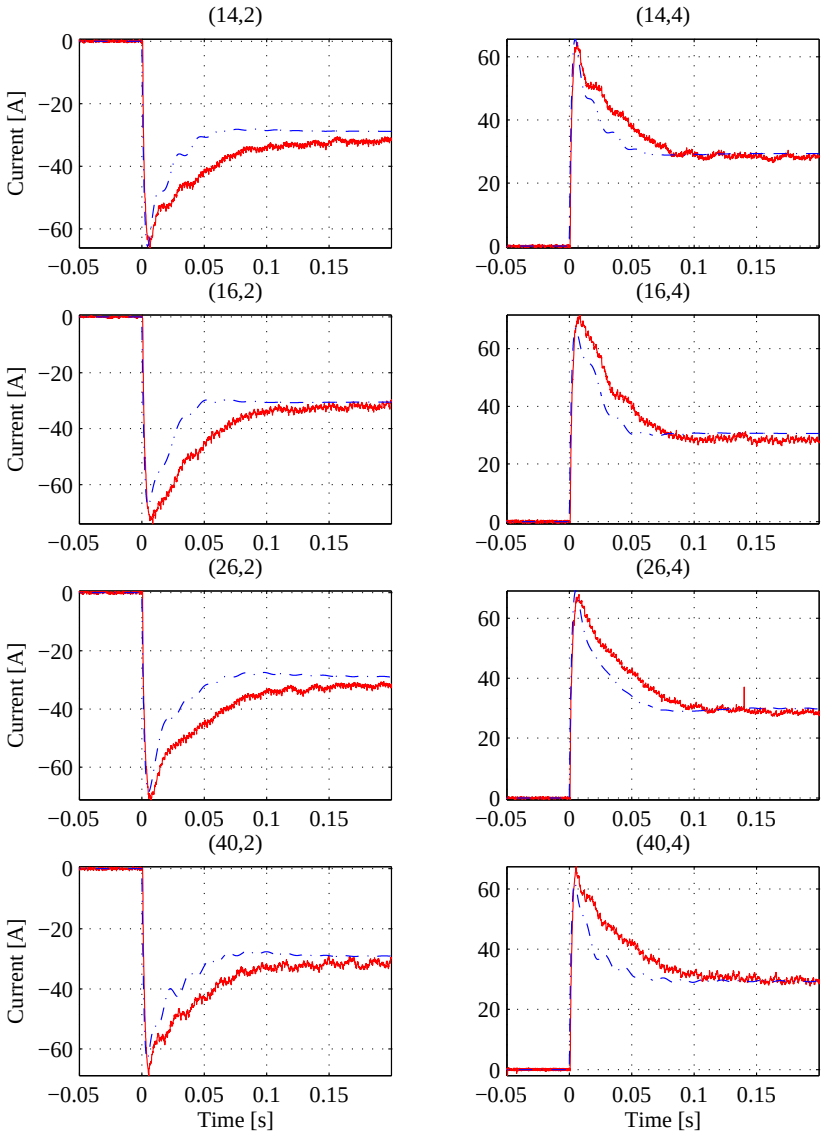

Figure 3.20: Comparison between experimental (red) and simulated currents (blue) using the closed loop model in shot 17167.

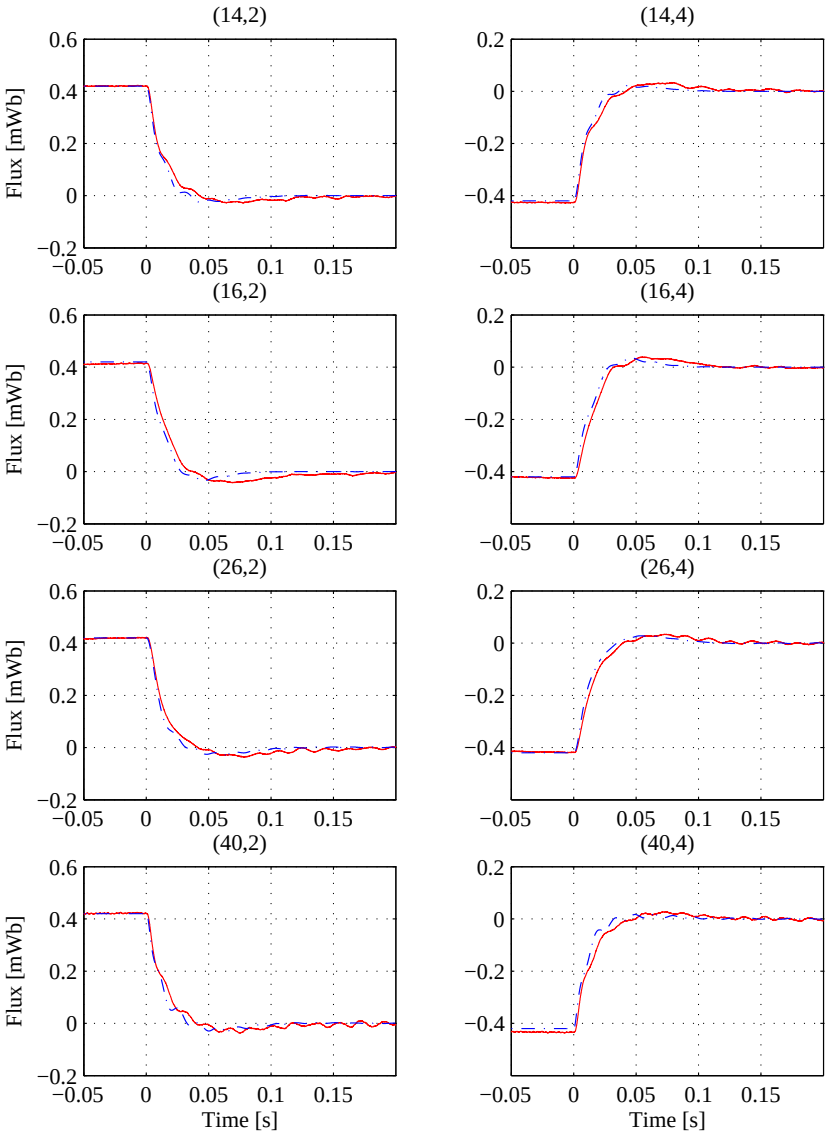

Figure 3.21: Comparison between experimental (red) and simulated radial flux measurements (blue) using the closed loop model in shot 17167.

k_I was reduced to 40×10^3 in the following shot 17167, obtaining a stable, fairly prompt response. Again the model results satisfactorily agree with the experimental ones not only in terms of the feedback controlled quantities but also in terms of saddle coil voltages and currents. In Figure 3.19, 3.20 and 3.21 voltages, currents and radial components of the magnetic fields are presented along with the corresponding experimental quantities.

3.6 Conclusions

A full electromagnetic model of the active control system of plasma MHD modes in RFX-mod has been developed. An extensive series of validation tests proved the model capability to reproduce the system open and closed loop response in terms of evolution of the magnetic fluxes with satisfactory accuracy. Since all the model parameters have been derived from experimental data, the effects of the toroidal geometry, passive structures, and the presence of non axialsymmetric features on the dynamics of the coil currents and the radial field are implicitly taken into account. The model should be a basic tool for the design of more complex controllers to further improve the interaction with the plasma modes by fully exploiting the real-time system flexibility.

Chapter 4

Pseudo-Decoupler

4.1 Introduction

Interest in real time control of the magnetic field perturbations in fusion devices has been growing in the last years because of the demanding stability requirements associated with advanced scenarios. Experiments in the RFP configuration may play an important role in this framework: due to the richer harmonic content of the edge magnetic field perturbations compared to the Tokamak, the RFP is a challenging test-bed for the development of edge magnetic field control scenarios. RFX-mod has been designed with the aim of extensive experimental activity in this field [4], the MHD system described in the previous chapters being the tool for its exploitation.

Different control strategies acting either equally on all the radial magnetic field harmonic components (Virtual Shell) or selectively on subsets of them (Mode Control) have been implemented. Both led to a substantial improvement of the plasma confinement with a three-fold increase of the pulse length and have been routinely used ever since [9].

Various types of PID controllers of either the single sensor signals or the mode components were designed according to Single-Input-Single-Output techniques. Such an approach was successful in controlling resistive wall modes (RWM) and in producing highly monochromatic static spectra. On the other hand, the available PI regulator was less effective in the control of tearing modes, being able to exert a rotating torque only up to 20-30 Hz [14]. This was due to the high coupling of the active system, each coil affecting at least one fourth of the total number of underlying sensors.

Thus a Multi-Input-Multi-Output approach to the control system design was expected to be more adequate to meet the requirements given in terms of spectral dynamic monochromaticity, reference tracking error and disturbance

rejection. The MIMO model of the coils and sensors in the presence of the passive structures, described in chapter 3, has been used in the design of a new control strategy. The high dimensionality of the problem was not a minor issue to cope with and some simplifying assumptions were adopted to carry out the design. Moreover, in the model simulations the plasma is assimilated to an external disturbance and it can be neglected to investigate the maximum achievable performance in terms of stability margins and tracking capability which are limited mainly by the presence of the passive structures.

4.2 Previous design attempts

Up to now, the best achieved performances in RFX-mod have been obtained with a control system made up of 192 PID controllers that shared the value of integral, proportional and derivative gains k_I, k_P and k_D. Despite the use of PID controllers has several well understood advantages, this technique can fail to produce satisfying controllers, for example because the diagonal PID structure does not take into account most of the plant interactions.

Trying to move forward from the diagonal PID design, the use of optimal techniques such as LQG, H_∞ or pole placement have been considered. They all have the major flaw in the need of the plant model, which is the starting point of a long sequence of calculations, not always well conditioned, producing in most cases a dynamic controller of nearly the same size as the model.

However, despite the great number of states, the model has also the peculiar structure of having a block diagonal state matrix with a very small block size of maximum 3 and the other matrices of the state space representation largely sparse. After observing that the general purpose libraries of Matlab® fail in performing the model reduction, specialised routines performing a model reduction based on the truncation of the least Hankel singular values have been written. Using the specialised routines it has been possible to reduce significantly the number of states to about 600. Unfortunately, the truncation did not preserve the stability of the original model making it not directly usable for the controller design.

After finding difficulties in the model reduction, optimal designs have been abandoned in favour of a sub-optimal inverse-based decoupler design [15]. A first insight into the control problem was obtained designing a pre-compensator based on an approximation of the plant inverse calculated by taking into account a small subset of the possible couplings. Unfortunately closed loop stability of the pre-compensated plant was not achievable with a satisfying disturbance rejection using this method. This suggested a different approach as described in the following paragraph.

4.3 Projecting Decoupler

The approximated decoupler described in the above section evidenced some problems when trying to increase the number of neighbours considered. Experience on this point contributed in showing that the condition div $\boldsymbol{B}(t) = 0$ shall not be ignored when designing the compensator. So, a completely new design around the integral form of the above condition has been made.

$$\int_{T_s} \boldsymbol{b}(t) d\boldsymbol{S} = \sum_{i=1}^{192} \int_{T_i} \boldsymbol{b}(t) d\boldsymbol{S} = \sum_{i=1}^{192} \psi_i(t) = 0 \tag{4.1}$$

In the above equations T_s is the whole toroidal surface covered with the 192 measure coils each of area T_i and linked flux $\psi_i(t)$.

4.3.1 Projected model

The above condition can be expressed in matricial form defining the vector $\boldsymbol{q}^H = [1, \ \ldots \ , 1]$, where the superscript H denotes the conjugate transpose of the matrix. If a transfer function matrix $\mathbf{G}(j\omega)$ represents a dynamic system whose outputs are flux measures spanning exactly a closed surface, it satisfies the flux conservation condition if and only if $\boldsymbol{q}^H \mathbf{G}(j\omega) = \mathbf{0}^H$. This equation implies that every transfer function matrix satisfying condition (4.1) can not be full rank, and thus can not be invertible. The available model of the plant, despite its accuracy in reproducing the plant dynamics, actually does contain approximations for which the flux condition is not fulfilled. In particular only a small number of couplings has been considered in the model [16].

A measure of how far is a model from meeting the flux condition can be derived considering the orthogonal projector

$$\mathbf{Q} = \frac{\boldsymbol{q}\boldsymbol{q}^H}{\boldsymbol{q}^H \boldsymbol{q}} \tag{4.2}$$

and its complementar

$$\mathbf{P} = \mathbf{I} - \mathbf{Q}, \tag{4.3}$$

where $\mathbf{I}$ is the identity matrix. Using these two projectors it is possible to decompose the transfer function matrix into the parallel component $\mathbf{G}_{\parallel}(j\omega)$ which satisfy equation (4.1) and the orthogonal $\mathbf{G}_{\perp}(j\omega)$ component which does not. This follows from the fact that $\mathbf{P} + \mathbf{Q} = \mathbf{I}$, considering that $\boldsymbol{q}^H \mathbf{P} = \mathbf{0}^H$ holds.

$$\mathbf{G}(j\omega) = (\mathbf{P} + \mathbf{Q})\mathbf{G}(j\omega) = \mathbf{P}\mathbf{G}(j\omega) + \mathbf{Q}\mathbf{G}(j\omega) = \mathbf{G}_{\parallel}(j\omega) + \mathbf{G}_{\perp}(j\omega) \tag{4.4}$$

It is straightforward to show that if condition (4.1) is satisfied for a transfer function matrix then necessarily it has a null orthogonal component. This means that the maximum singular value of the orthogonal component $\epsilon(\omega) = \|\mathbf{G}_\perp(j\omega)\|_2$ is a measure, at the chosen frequency, of how far is the transfer function matrix from fulfilling the flux condition.

4.3.2 Decoupler synthesis

As the available model of the plant did have a non null orthogonal component, the decoupler synthesis has been made starting from the component resulting from its projection onto the space of models satisfying the flux condition. To attain the simplest possible shapes in the decoupler transfer functions a symmetrisation step has been applied to the model before calculating its projected component. The symmetrisation step results in neglecting the effect of any toroidal feature such as shell overlapping edges or holes under the coils, but still taking into account the effects of its inner equatorial gap. As we shall see in the following paragraphs a simple shape of the transfer functions in the decoupler is a necessary condition for its implementation in a real time control loop. We regard model scaling, symmetrisation and projection as preliminary operations resulting in a conditioned model satisfying the required physical relations and additional control synthesis constraints. In the following we use the symbol $\tilde{\mathbf{G}}(j\omega)$ to refer to the system obtained after the preliminary steps have been applied to the available model.

The projecting decoupler $\mathbf{W}(j\omega)$ has been derived from the plant model using the Singular Value Decomposition (SVD) [17] of $\tilde{\mathbf{G}}(j\omega)$.

$$\tilde{\mathbf{G}}(j\omega) = [\mathbf{U}_1(j\omega)\ \mathbf{U}_2(j\omega)] \begin{bmatrix} \mathbf{\Sigma}_1(j\omega) & \mathbf{0} \\ \mathbf{0} & 0 \end{bmatrix} [\mathbf{V}_1(j\omega)\ \mathbf{V}_2(j\omega)]^H \tag{4.5}$$

The projecting decoupler is then defined to be

$$\mathbf{W}(j\omega) = \mathbf{V}_1(j\omega)\mathbf{\Sigma}_1^{-1}(j\omega)\mathbf{U}_1^H(j\omega) \tag{4.6}$$

The name has been chosen after the property that the transfer function matrix $\mathbf{N}(j\omega) = \tilde{\mathbf{G}}(j\omega)\mathbf{W}(j\omega)$ is itself an orthogonal projector onto the space of the distributions which satisfy the flux conservation condition, the space of the admissible distributions. It is shown in the appendix, with an SVD exercise, that $\mathbf{N}(j\omega) = \mathbf{P}$.

4.3.3 Decoupler implementation

The theoretical results obtained in the previous section have been used to implement a decoupling control scheme. The main issue of the implementing

procedure was the state space realisation of the projecting decoupler. The symmetrised and projected model has been evaluated in the frequency range from 10^{-2} to 10^{3} Hz. The frequency response of the projecting decoupler $\mathbf{W}(j\omega)$ has been derived using equation (4.6) over the same frequency range.

In general, an inverse based approach in the design of the controller is not appealing because for strictly proper plants (the majority of the physical systems) the obtainable compensator is not a proper system. This would indeed be the case. However, a full inversion of the system dynamics was not needed to extend the static decoupling design done in the past to a reasonably wide range of frequencies. By inspection of the elements of $\mathbf{W}(j\omega)$ it has been noticed that each one could have been reasonably approximated in a fairly wide frequency range by a simple transfer function having just two zeros. It turned out that the maximum frequency range I_f for which the approximation could be applicable went from 0 to 200 Hz.

To obtain a reasonably small state space realisation, a couple of stable poles outside the frequency range of interest was added. The location of the zeros have then been found by fitting the frequency response of each transfer function in the projecting decoupler with the following second order model

$$k\frac{(s\theta_1+1)(s\theta_2+1)}{(s\tau_p+1)^2} \tag{4.7}$$

using a least square procedure. In the above model the gain k and the pole $1/\tau_p$ were fixed parameters not affected by the optimisation procedure, whereas θ_1 and θ_2 were the parameters to be identified. The gain of each transfer function has been calculated evaluating the relevant projecting decoupler element at $\omega = 0$, whereas for τ_p has been used a value chosen to lie outside the frequency range of interest. The result of the fitting procedure is an approximation $\tilde{\mathbf{W}}(j\omega)$ of the projecting decoupler such that $\tilde{\mathbf{W}}(j\omega) \approx \mathbf{W}(j\omega)$ over the frequency range I_f.

A state space realisation of the approximating model has been obtained placing the poles in the same position for each transfer function. It resulted to have 192 inputs, 192 outputs, 384 states and to be able to approximate the projecting decoupler over the frequency range I_f. The state matrix $\mathbf{A}$ and the input-state matrix $\mathbf{B}$ turned out to be block diagonal, with block dimensions respectively 2×2 and 2×1. The state-output matrix $\mathbf{C}$ and the input-output matrix $\mathbf{D}$ however, resulted to be full.

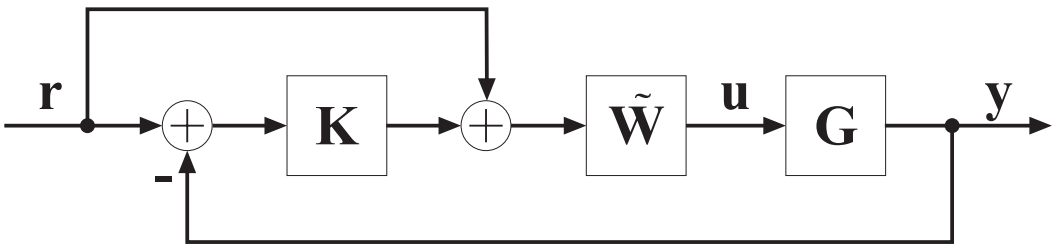

Figure 4.1: Scheme of the control loop

4.4 Controller synthesis

As in the classical decoupling designs, in this pseudo-inverse based procedure, the controller synthesis is made after the pseudo-decoupler is obtained. The compensated plant satisfies

$$\mathbf{G}(j\omega)\tilde{\mathbf{W}}(j\omega) \approx \mathbf{N}(j\omega) = \mathbf{P} \tag{4.8}$$

in the frequency range I_f and so it behaves like a projector. This means that if the reference signals are admissible they are presented at the output ports of the plant unchanged. Thus, in the space of the admissible distributions, the compensated plant is the identity, at least for those distributions with limited band. In these conditions a closed loop control paradigm has been implemented. The control system has been designed with a feedback on the output error to face disturbances and a feedforward action to improve the reference tracking. The block diagram of the implemented control loop is illustrated in Figure 4.1. In the frequency range of interest, for a reference input satisfying the relation $\boldsymbol{r} = \mathbf{P}\boldsymbol{r}$, the transfer function $\mathbf{T}(j\omega)$ from $\boldsymbol{r}$ to the output $\boldsymbol{y}$ can be approximated by

$$\mathbf{T}(j\omega) \approx (\mathbf{P}\mathbf{K}(j\omega) + \mathbf{I})^{-1}\mathbf{P}(\mathbf{K}(j\omega) + \mathbf{I}) \approx \mathbf{I}. \tag{4.9}$$

This can be realised considering that $\mathbf{G}(j\omega)\tilde{\mathbf{W}}(j\omega)$ is approximated by $\mathbf{P}$, and that $\mathbf{P}$ is a projector. The sensitivity function $\mathbf{S}(j\omega)$ is instead

$$\mathbf{S}(j\omega) = (\mathbf{G}(j\omega)\tilde{\mathbf{W}}(j\omega)\mathbf{K}(j\omega) + \mathbf{I})^{-1} \tag{4.10}$$

The structure of the gain $\mathbf{K}(j\omega)$ has been chosen to be diagonal with the same action on each error channel, that is $\mathbf{K}(s) = k(s) * \mathbf{I}$ where $k(s)$ is a single transfer function. To achieve satisfying performance in terms of reference tracking and disturbance rejection a controller with the following shape has been selected.

$$k(s) = k_0 \frac{s\tau_{k_z} + 1}{s(s\tau_{k_p} + 1)} \tag{4.11}$$

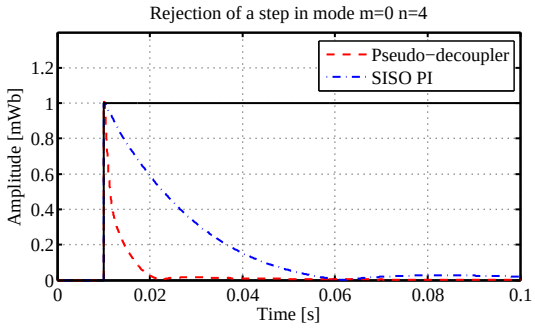

Figure 4.2: Comparison between the new and the SISO PID controller performance in rejecting a m=0 n=4 disturbance step.

4.5 Simulation results

The approximated pseudo-decoupler $\tilde{\mathbf{W}}(j\omega)$ and the feedback gain $\mathbf{K}(j\omega)$ have been implemented as continuous state space models. In order to make a comparison of the performances obtainable with the new controller, a state space form of the actually implemented SISO PI controller has also been realised. The structure of this controller is diagonal with the same proportional and integral action on each error channel. The proportional gain used was $k_P = 800$ whereas the integral gain was set to $k_I = 40 \cdot 10^3$. Simulations with the available model of the dynamics between currents and fluxes have been run with the new and the PI controller. Three kind of experiments are presented in this paper, the rejection of a modal disturbance step, the rejection of a 20 Hz rotating mode and the tracking of a 50 Hz rotating mode. The modes m=1, n=7, and m=0, n=4 were chosen as reference signals. The former corresponds to a typical tearing mode whose control at the plasma edge is of particular interest in RFP discharges; the latter was selected to highlight the effect of interaction between neighbouring coils. The reason behind this choice can be understood considering that the lower are the values m and n, the higher is the number of adjacent coils carrying a current of the same sign. In this condition, the flux generated by the coil directly above a sensor is substantially reduced by the contribute of the other coils.

In Figure 4.2 and 4.3 the rejection of a modal flux disturbance step is presented. Both the controllers are able to zero the output error, but the new one has a faster response and presents a shorter descent time in both cases. More interestingly, the dynamic response of the system under the effect of the pseudo decoupler is the same. This means that the efficiency of the MHD system in generating different modes can be made the same in the frequency

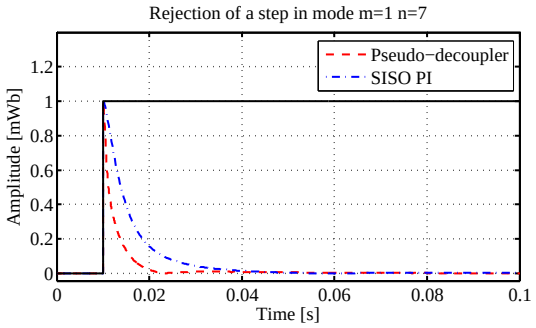

Figure 4.3: Comparison between the new and the SISO PID controller performance in rejecting a m=1 n=7 disturbance step.

range I_f.

In Figure 4.4 and 4.5 are presented the system performances in counteracting the effect of the two rotating modal disturbances (m=0, n=4 and m=1, n=7). We see here that a clear improvement of the performance can be obtained using the pseudo-decoupler, especially in the less efficient m=0, n=4 case, where the PI controller has very little effect. However, although the pseudo-decoupling controller performs better than the SISO PI, a 25% residual disturbance is still present.

The last couple of pictures, Figure 4.6 and 4.7, refers to the tracking performance of the controllers. Again the simulations results show that the pseudo-decoupler performs better in tracking the rotating mode and has a much lower steady state error.

Simulations, however, highlighted a potential problem of the pseudo-decoupler approach. The current driven by the power amplifiers is, in fact, more than the current used by the simple decentralised PI controller. With the pseudo-decoupler tracking a 1 mWb m=1, n=7 mode rotating at 50 Hz, the regime requests are about the maximum allowed by the power amplifiers.

4.6 Conclusions

The major result of this chapter is the constructive demonstration that controllers potentially able to improve the dynamic performance in terms of mode tracking, disturbance rejection and spectrum quality do exist. Indeed, simulations results suggest that the new controller of the MHD system based on the pseudo-decoupler exhibits better performances than the diagonal PI controller. It is still an open question whether an actual improvement in the

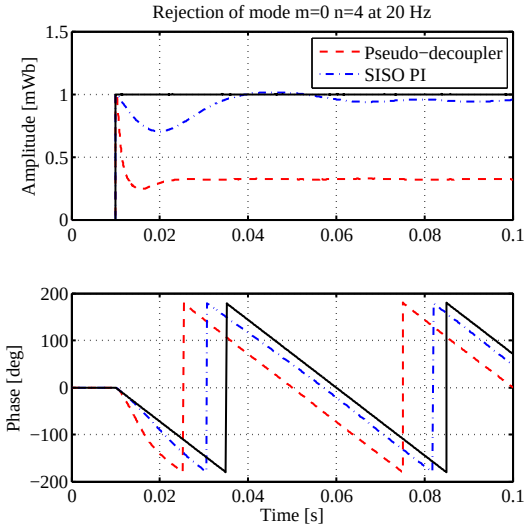

Figure 4.4: Comparison between the new and the SISO PID controller performance in rejecting a m=0 n=4 rotating mode at 20 [Hz].

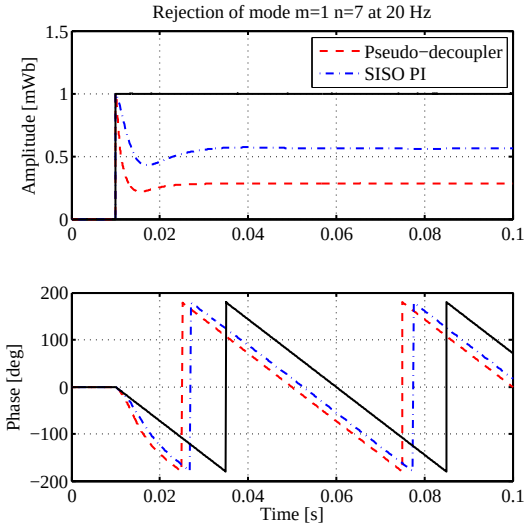

Figure 4.5: Comparison between the new and the SISO PID controller performance in rejecting a m=1 n=7 rotating mode at 20 [Hz].

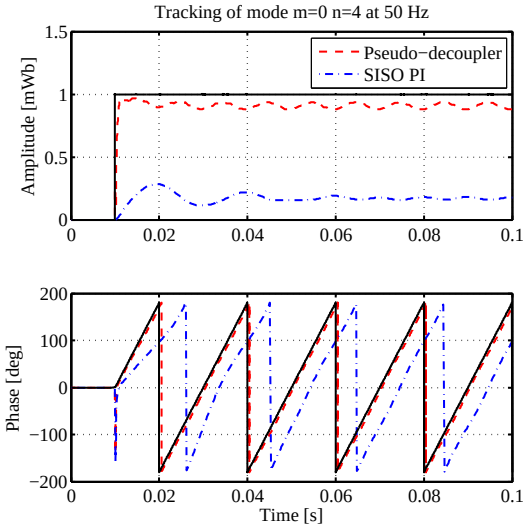

Figure 4.6: Comparison between the new and the SISO PID controller performance in tracking a m=0 n=4 rotating mode at 50 [Hz].

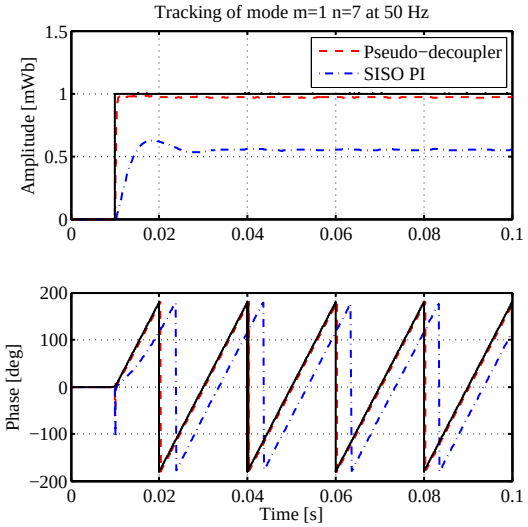

Figure 4.7: Comparison between the new and the SISO PID controller performance in tracking a m=1 n=7 rotating mode at 50 [Hz].

performances is allowed by the limits of the power amplifiers or whether the same performance can be achieved with a less current demanding controller designed following different paradigms. However, the controller, obtained following the pseudo-decoupler approach, is also an interesting benchmark for other control algorithms and an useful tool to gain insight into the intrinsic limits of the active control system.

Chapter 5

Conclusions and further developments

The research activity covered the analysis and modelling of an electromagnetic MIMO dynamic system with 192 inputs and 192 outputs. It also covered the field of control system engineering with the implementation of a pseudo-decoupling control scheme which is also an example of the applicability of the model.

The theoretical analysis of the active system for the control of MHD instabilities showed how the concepts of the Unified Signal Theory can be applied to the analysis of this system. The use of the Unified Framework allows to grasp the essential features of the system. Its strong mathematical foundations provide a model for the understanding of the MHD control algorithms and it can be used to establish a common background among physicists and engineers. The study allowed to highlight the structural difference between axialsymmetric cylindrical models and the signal-based model of the same MHD system, the most important regarding the system spatial non-invariance. However, it is not aimed at demoting the importance of analytical models, which are understood to be essential to the development of the plasma physics and are always valuable in the implementation of algorithms often able to improve the performance of the machine to an excellent level. Despite this mathematical analysis has not produced results of immediate practical relevance, it has been extremely useful in characterising the effect of sampling quantities on a bi-dimensional toroidal manifold, in particular the spectral analysis of the flux sensors has been performed quantitatively. The work performed provides methods which can be considered when the assumptions made by simpler models become unacceptable, for example it could be used in the need of improving the actual sideband correction algorithm. In fact it takes into account properties such as the spatial variance of the system, the frequency

dependence of the field distribution and the conservation law of the magnetic flux which are presently neglected in the sideband analytical calculations. In particular, the presence of shell local features such as gaps and ports is cause of a strong spatial variance. A natural development of this study consists in the the numerical calculation of the actual harmonic content of the field distribution generated by the saddle coil currents. This task can be carried out using a Finite Element Model of the machine active coils and passive structures and a electromagnetic solver such as CARIDDI, for example.

The activity of modelling the RFX-mod active control system for the control of the MHD instabilities has been concluded producing a full electromagnetic model of the system whose state space representation consists of more than 6000 states. The peculiarity of this model is the fact that it has been derived almost entirely from experimental data. Extensive series of validation tests proved the model capability to reproduce the system open and closed loop response in terms of evolution of the magnetic fluxes with satisfactory accuracy. The same tests showed that the inductive effect of the plasma on the currents in the active coils can be neglected. This can be used in the construction of models comprehensive of the plasma action because it allows to simplify the problem. The derived model is capable of quantitative analysis of the relevant measured quantities and has been used with success in the study of unstable phenomena which the MHD system had exhibited. In particular, the model is able to reproduce the stability range of the closed loop system, whose upper limit is not determined by an effect of the plasma but by the MHD system itself. Finally, since all the model parameters have been derived from experimental data, the effects of the toroidal geometry, passive structures, and the presence of non axialsymmetric features on the dynamics of the coil currents and the radial field are implicitly taken into account. Recently, a new campaign of measures has been concluded and the integration of the new measures into the current model is ongoing. Despite it has been successfully used up to now, the uge size of the model could be a limit to further developments. Advanced model reduction techniques, able to deal with models of size ten thousand, could be investigated, because preliminary reduction attempts suggest that the model can be reduced to about one tenth of its original size. Apart of this activity, from the point of view of the modelling, it would be also interesting exploring ways to couple the MHD equations to this electromagnetic model of the machine in order to obtain a global model comprehensive of the plasma interactions suitable for the design of improved control algorithms.

Finally, the last results of the research is the development of a new controller for the MHD system. Its design has been done on the basis of the data of the electromagnetic model which had just been developed. During the

research activity several design techniques have been considered. The high dimensionality of the available model and the real-time constraints of the controller implementation seriously limited the usable design techniques. Finally a MIMO approach was followed based on a decoupling component together with a controller designed with the classical loop shaping method. It should be pointed out that the design method required the explicit use of the flux conservation law in the controller derivation. This resulted in a pseudo-decoupler component instead of a full decoupling design whose properties have also been algebraically demonstrated. Simulation results confirm that such controller scheme can improve the dynamic performance of the MHD control system in terms of mode tracking, disturbance rejection and spectrum quality. Considering these properties, the new controller based on the pseudo-decoupler exhibits better performances than the diagonal PI controller. The real-time implementation of the pseudo-decoupling algorithm is currently ongoing. Preliminary tests have been carried out on the crate hosting the computer board used in the control system architecture of the RFX-mod MHD units and the EFDA-JET vertical stabilisation component. Early results suggest that it is possible to implement the pseudo-decoupler algorithm on one node of the architecture (which consists of a Motorola VME5500 board equipped with a single PowerPC processor), this however has required a full exploitation of the board features at the lowest possible level (kernel level and/or hardware level). At the moment an offline application of the pseudo-decoupler in the field of the error field correction is considered. In this application the MHD system is expected to counteract the effect of the error fields induced by the magnetising winding. The pseudo-decoupler provides also a benchmark for other controllers. Apart from the pseudo-decoupler no other implemented controllers are known to have the property of equalising the MHD system so as to achieve the same penetration time constant for each spatial harmonic. In the field of the control system engineering, an interesting application is the study of the technical feasibility of real-time eddy currents calculation. It is still an open question whether the required performances are allowed by the limits of the power amplifiers or whether the same performances can be achieved with a less current demanding controller designed following different paradigms.

Appendix A

Technicalities

In the following chapter are proved four propositions stated in the rest of the dissertation.

Proposition A.1. *For every cell $C = [U/P)$ there exist a one to one mapping $\mu : C \to U/P$ from C to the quotient group U/P.*

Proof. Consider the restriction to C of the natural mapping from U into U/P $\mu(c) : c \in C \to c + P$. Suppose $(c_1 + P) \cap (c_2 + P) \neq \varnothing$. So there exist an element u which belongs at the same time to $(c_1 + P)$ and to $(c_2 + P)$. That is there exist two elements, $p_1, p_2 \in P$, so that

$$u = c_1 + p_1 = c_2 + p_2. \tag{A.1}$$

This equation also states that u is both in $C + p_1$ and $C + p_2$ so, from the relation (2.5) is possible to conclude that $p_1 = p_2$ and also $c_1 = c_2$. This proves the map injectivity.

Every possible member of U/P can be expressed in the form $u + P$ with $u \in U$. Equation (2.4) gives $(C + P) \cap (u + P) = U \cap (u + P) = u + P$. That is, for every $u \in U$, there exist a $c \in C$ and $p_1, p_2 \in S$ so that $c + p_1 = u + p_2$, which means that $\mu(c) = u + P$. This proves the map surjectivity. □

Proposition A.2. *Given a time variant system $g(\boldsymbol{t}_1, \boldsymbol{t}_2)$ transforming the input signal $u(\boldsymbol{t}_1)$ defined over the domain I into the corresponding output signal $v(\boldsymbol{t}_2)$ defined over the same domain by the law*

$$v(\boldsymbol{t}_2) = \int_I u(\boldsymbol{t}_1) g(\boldsymbol{t}_1, \boldsymbol{t}_2) d\boldsymbol{t}_1 \tag{A.2}$$

the Fourier transform of $u(\boldsymbol{t}_1)$, $v(\boldsymbol{t}_2)$ and $g(\boldsymbol{t}_1, \boldsymbol{t}_2)$, respectively $U(\boldsymbol{f}_1)$, $V(\boldsymbol{f}_2)$ and $G(\boldsymbol{f}_1, \boldsymbol{f}_2)$, are related by the equation

$$V(\boldsymbol{f}_2) = \int_{\hat{I}} U(\boldsymbol{f}_1) G(-\boldsymbol{f}_1, \boldsymbol{f}_2) d\boldsymbol{f}_1 \tag{A.3}$$

Proof. Considering that

$$U(\boldsymbol{f}_1) = \int_I u(\boldsymbol{t}_1) e^{-j2\pi \boldsymbol{f}_1 \cdot \boldsymbol{t}_1} d\boldsymbol{t}_1$$

and

$$G(\boldsymbol{f}_1, \boldsymbol{f}_2) = \iint_{I\ I} g(\boldsymbol{t}_1, \boldsymbol{t}_2) e^{-j2\pi(\boldsymbol{f}_1 \cdot \boldsymbol{t}_1 + \boldsymbol{f}_2 \cdot \boldsymbol{t}_2)} d\boldsymbol{t}_1 d\boldsymbol{t}_2$$

equation (2.18) becomes

$$\begin{aligned}
V(\boldsymbol{f}_2) &= \int_{\hat{I}} \int_I u(\boldsymbol{t}_1) e^{-j2\pi \boldsymbol{f}_1 \cdot \boldsymbol{t}_1} d\boldsymbol{t}_1 \iint_{I\ I} g(\boldsymbol{t}_1, \boldsymbol{t}_2) e^{-j2\pi(-\boldsymbol{f}_1 \cdot \boldsymbol{t}_1 + \boldsymbol{f}_2 \cdot \boldsymbol{t}_2)} d\boldsymbol{t}_1 d\boldsymbol{t}_2 d\boldsymbol{f}_1 \\
&= \iiiint_{\hat{I} \times I \times I \times I} u(\boldsymbol{t}_3) e^{-j2\pi \boldsymbol{f}_1 \cdot \boldsymbol{t}_3} g(\boldsymbol{t}_1, \boldsymbol{t}_2) e^{-j2\pi(-\boldsymbol{f}_1 \cdot \boldsymbol{t}_1 + \boldsymbol{f}_2 \cdot \boldsymbol{t}_2)} d\boldsymbol{t}_3 d\boldsymbol{t}_1 d\boldsymbol{t}_2 d\boldsymbol{f}_1 \\
&= \iiint_{I \times I \times I} g(\boldsymbol{t}_1, \boldsymbol{t}_2) e^{-j2\pi \boldsymbol{f}_2 \cdot \boldsymbol{t}_2} u(\boldsymbol{t}_3) \int_{\hat{I}} e^{-j2\pi \boldsymbol{f}_1 \cdot (\boldsymbol{t}_3 - \boldsymbol{t}_1)} d\boldsymbol{f}_1 d\boldsymbol{t}_3 d\boldsymbol{t}_1 d\boldsymbol{t}_2 \\
&= \iint_{I \times I} g(\boldsymbol{t}_1, \boldsymbol{t}_2) e^{-j2\pi \boldsymbol{f}_2 \cdot \boldsymbol{t}_2} \int_I u(\boldsymbol{t}_3) \delta_I(\boldsymbol{t}_3 - \boldsymbol{t}_1) d\boldsymbol{t}_3 d\boldsymbol{t}_1 d\boldsymbol{t}_2 \\
&= \int_I e^{-j2\pi \boldsymbol{f}_2 \cdot \boldsymbol{t}_2} \int_I u(\boldsymbol{t}_1) g(\boldsymbol{t}_1, \boldsymbol{t}_2) d\boldsymbol{t}_1 d\boldsymbol{t}_2 \\
&= \int_I v(\boldsymbol{t}_2) e^{-j2\pi \boldsymbol{f}_2 \cdot \boldsymbol{t}_2} d\boldsymbol{t}_2
\end{aligned}$$

□

Proposition A.3. *Given a function g of two vectorial variables $\boldsymbol{t}_1, \boldsymbol{t}_2 \in I = G/P$ such that for every $\boldsymbol{d} \in I$ $g(\boldsymbol{t}_1 + \boldsymbol{d}, \boldsymbol{t}_2 + \boldsymbol{d}) = g(\boldsymbol{t}_1, \boldsymbol{t}_2)$, its Fourier transform is*

$$G(\boldsymbol{f}_1, \boldsymbol{f}_2) = \delta_{\hat{I}}(\boldsymbol{f}_1 + \boldsymbol{f}_2) G_r(\boldsymbol{f}_2) = \delta_{\hat{I}}(\boldsymbol{f}_1 + \boldsymbol{f}_2) G_r(-\boldsymbol{f}_1) \tag{A.4}$$

where

$$G_r(\boldsymbol{f}_2) = \int_I g(\boldsymbol{0}, \boldsymbol{\tau}) e^{j2\pi \boldsymbol{f}_2 \boldsymbol{\tau}} d\boldsymbol{\tau} \tag{A.5}$$

Proof.

$$\begin{aligned}
G(\boldsymbol{f}_1, \boldsymbol{f}_2) &= \iint\limits_{I\times I} g(\boldsymbol{t}_1, \boldsymbol{t}_2) e^{-j2\pi(\boldsymbol{f}_1\cdot\boldsymbol{t}_1 + \boldsymbol{f}_2\cdot\boldsymbol{t}_2)} d\boldsymbol{t}_1 d\boldsymbol{t}_2 \\
&= \iint\limits_{I\times I} g(\mathbf{0}, \boldsymbol{\tau}) e^{-j2\pi(\boldsymbol{f}_1\cdot\boldsymbol{t}_1 + \boldsymbol{f}_2\cdot\boldsymbol{t}_1 + \boldsymbol{f}_2\cdot\boldsymbol{\tau}))} d\boldsymbol{t}_1 d\boldsymbol{\tau} \\
&= \int\limits_{I} g(\mathbf{0}, \boldsymbol{\tau}) e^{-j2\pi\boldsymbol{f}_2\cdot\boldsymbol{\tau}} \int\limits_{I} e^{-j2\pi(\boldsymbol{f}_1+\boldsymbol{f}_2)\cdot\boldsymbol{t}_1} d\boldsymbol{t}_1 d\boldsymbol{\tau} \\
&= \int\limits_{I} g(\mathbf{0}, \boldsymbol{\tau}) e^{-j2\pi\boldsymbol{f}_2\cdot\boldsymbol{\tau}} \delta_{\hat{I}}(\boldsymbol{f}_1 + \boldsymbol{f}_2) d\boldsymbol{\tau} \\
&= \delta_{\hat{I}}(\boldsymbol{f}_1 + \boldsymbol{f}_2) \int\limits_{I} g(\mathbf{0}, \boldsymbol{\tau}) e^{-j2\pi\boldsymbol{f}_2\cdot\boldsymbol{\tau}} d\boldsymbol{\tau} \\
&= \delta_{\hat{I}}(\boldsymbol{f}_1 + \boldsymbol{f}_2) G_r(\boldsymbol{f}_2)
\end{aligned}$$

The above chain of equations follows from the position $\boldsymbol{\tau} = \boldsymbol{t}_2 - \boldsymbol{t}_1$ substituting $\boldsymbol{t}_2$ in favour of $\boldsymbol{\tau}$, whereas the second equation of the proposition follows substituting $\boldsymbol{t}_1$ with $\boldsymbol{\tau}$ in similar manner. □

Proposition A.4. *Considering the relations of section 4.3.2, that is*

$$\boldsymbol{q}^H = [1, \ldots, 1], \quad \boldsymbol{q}^H \mathbf{G}(j\omega) = \mathbf{0}^H, \tag{A.6}$$

$$\mathbf{Q} = \frac{\boldsymbol{q}\boldsymbol{q}^H}{\boldsymbol{q}^H\boldsymbol{q}}, \quad \mathbf{P} = \mathbf{I} - \mathbf{Q}, \tag{A.7}$$

$$\mathbf{G}(j\omega) = \mathbf{U}_1(j\omega)\boldsymbol{\Sigma}(j\omega)\mathbf{V}_1^H(j\omega) \tag{A.8}$$

and

$$\mathbf{W}(j\omega) = \mathbf{V}_1(j\omega)\boldsymbol{\Sigma}^{-1}(j\omega)\mathbf{U}_1^H(j\omega) \tag{A.9}$$

then

$$\mathbf{G}(j\omega)\mathbf{W}(j\omega) = \mathbf{P} \tag{A.10}$$

for every $\omega \in \mathbb{R}$.

Proof. $\boldsymbol{q}^H\mathbf{G}(j\omega) = \mathbf{0}^H$ implies that

$$\boldsymbol{q}^H\mathbf{G}(j\omega)\mathbf{W}(j\omega) = \boldsymbol{q}^H\mathbf{U}_1(j\omega)\mathbf{U}_1^H(j\omega) = \mathbf{0}^H \tag{A.11}$$

because $\mathbf{U}_1(j\omega)$ is full rank. So $\frac{\boldsymbol{q}}{\sqrt{\boldsymbol{q}^H\boldsymbol{q}}}$ can be used to complete the basis $\mathbf{U}_1(j\omega)$ to $[\mathbf{U}_1(j\omega)\ \frac{\boldsymbol{q}}{\sqrt{\boldsymbol{q}^H\boldsymbol{q}}}]$. Then

$$\mathbf{U}_1(j\omega)\mathbf{U}_1^H(j\omega) = [\mathbf{U}_1(j\omega)\ \tfrac{\boldsymbol{q}}{\sqrt{\boldsymbol{q}^H\boldsymbol{q}}}] \begin{bmatrix} \mathbf{I} & \mathbf{0} \\ \mathbf{0} & 0 \end{bmatrix} [\mathbf{U}_1(j\omega)\ \tfrac{\boldsymbol{q}}{\sqrt{\boldsymbol{q}^H\boldsymbol{q}}}]^H \tag{A.12}$$

$$= [\mathbf{U}_1(j\omega)\ \frac{\boldsymbol{q}}{\sqrt{\boldsymbol{q}^H\boldsymbol{q}}}] \left(\mathbf{I} - \begin{bmatrix}\mathbf{0} & \mathbf{0}\\ \mathbf{0} & 1\end{bmatrix}\right) [\mathbf{U}_1(j\omega)\ \frac{\boldsymbol{q}}{\sqrt{\boldsymbol{q}^H\boldsymbol{q}}}]^H = \mathbf{I} - \mathbf{Q} \tag{A.13}$$

□

Bibliography

[1] Allen H. Boozer. Physics of magnetically confined plasmas. *Reviews of modern physics*, 76(4):1071–1141, October 2004.

[2] Topical issue on the rfx-experiment. *Fusion Engineering and Design*, 25(4), January 1995.

[3] P. Zaccaria F. Gnesotto S. Ortolani A. Buffa M. Bagatin W. R. Baker S. Dal Bello P. Fiorentin L. Grando G. Marchiori D. Marcuzzi A. Masiello S. Peruzzo N. Pomaro P. Sonato, G. Chitarin and G. Serianni. Machine modifications for active mhd control in rfx. *Fusion Engineering and Design*, 66-68:161–168, September 2003.

[4] A. Luchetta P. Sonato, R. Piovan. Control of non-axisymmetric magnetic fields for plasma enhanced performances: The rfx contribution. *Fusion Engineering and Design*, 74:97–107, November 2005.

[5] P. E. Stott C. M. Braams. *Nuclear Fusion: half a century of magnetic confinement research*. Institute of Physics Publishing, Dirac House, Temple Back, Bristol, BS1 6BE, UK, first edition, 2002. ISBN 0750307056.

[6] Gianfranco Cariolaro. *La teoria unificata dei segnali*. UTET libreria, Torino (ITALY), 2nd edition, 1996.

[7] Leopoldo Nachbin. *The Haar Integral*. D. Van Nostrand Company, 120 Alexander St., Princeton, New Jersey, USA, 1965.

[8] A. Luchetta G. Marchiori C. Taliercio M. Cavinato, G. Manduchi. Distributed real time control in rfx-mod nuclear fusion experiment: Commissioning and first results. *IEEE Transactions on Nuclear Science*, 53:1015–1021, 2003.

[9] S. Ortolani and the RFX team. Active mhd control experiments in rfx-mod. *Plasma Phys. Control. Fusion*, 48:B371–B381, 2006.

[10] P. R. Brunsell D. Yadikin G. Marchiori, A. Masiello. Open loop characterization of an active control system of mhd modes. *Fusion Engineering and Design*, 74:555–560, 2005.

[11] A. Masiello R. Paccagnella G.Marchiori, M. Cavinato. Electromagnetic modeling for the active control of mhd modes in rfx. *Fusion Engineering and Design*, 66–68:691–696, 2003.

[12] C. Taccon. Private communication.

[13] P. Zollino G. Chitarin, G. Marchiori. Computation and experimental validation of the transfer functions of the local control coil system in rfx. *Proceedings of the 17th Symposium on Fusion Engineering*, vol.I:572–575, October 1997.

[14] S. Martini et al. Active mhd control at high currents in rfx-mod. *Nuclear Fusion*, 47(8):783–791, August 2007.

[15] I. Postlethwaite S. Skogestad. *Multivariable feedback control*. Jhon Wiley & Son, XX, xx edition, 1996. ISBN 0 471 94277 4.

[16] Anton Soppelsa Giuseppe Marchiori. Development and validation of an electromagnetic model of the active control system of mhd modes in rfx-mod. *Fusion Engineering and Design*, 82:1015–1022, 2007.

[17] C. F. Van Loan G.H. Golub. *Matrix computations*. The Jhon Hopkins University Press, 2715 North Charles Street, Baltimore, Maryland, 21218-4319, USA, third edition, 1996. ISBN 0 8018 5413 X.